University of Southampton

National Oceanography Centre

Mechanisms of eddy dissipation in the Southern Ocean

Thesis for the degree of Doctor of Philosophy

Author:
Jesse Cusack

Supervisors:
Alberto Naveira Garabato
David Smeed
James Girton

18th December 2017

Abstract

UNIVERSITY OF SOUTHAMPTON

FACULTY OF NATURAL AND ENVIRONMENTAL SCIENCES

National Oceanography Centre

Doctor of Philosophy

Mechanisms of eddy dissipation in the Southern Ocean

by Jesse Cusack

The Southern Ocean is a region of fast currents, energetic eddies, large amplitude internal waves and strong turbulence. It is also a place where substantial quantities of heat and carbon are exchanged between the ocean and atmosphere. Our ability to predict global climatic changes relies, in part, on understanding the physical processes occurring there.

This thesis adds to the growing body of knowledge about Southern Ocean dynamics by using in-situ observations from profiling floats to study a lee wave generated in the Drake Passage by the flow of the Antarctic Circumpolar Current over topography. It is the first unambiguous example of such a wave in the Southern Ocean and is found to be associated with large fluxes of energy and momentum, as well as elevated turbulent dissipation. A key finding is that the energy flux is two orders of magnitude larger than the depth integrated dissipation, indicating that the majority of the energy may not be dissipated locally.

The wave observation was made possible by developing a method for measuring vertical velocity from profiling floats. The essence of the method is to model the expected steady motion of the float and subtract this from the observed motion to retrieve the vertical velocity. It is easily applicable to many similar floats and has the potential to provide a global picture of vertical flows in the ocean.

The interaction of eddies and internal waves away from boundaries is investigated for the first time in the Southern Ocean using data from a mooring array in the Scotia Sea. Theoretical arguments are made to treat the interaction as a viscous coupling between internal wave stress and eddy strain. The results imply that eddy dissipation by interaction with the internal wave field is an important energy sink and comparable in magnitude to lee wave generation and bottom boundary layer viscous processes.

Acknowledgements

First and foremost, I would like to thank my supervisors Alberto, David and James for their guidance and encouragement; it has been a pleasure working with you. I want to send big thanks out to all the friends I've met both in Southampton and around the world over the course of this PhD who have provided scientific advice, taken part in numerous shenanigans and generally made living in Southampton good fun. A special thanks goes to Helen for being so kind and supportive, even when I was stressed and grumpy.

Declaration Of Authorship

I, Jesse Cusack, declare that this thesis and the work presented in it are my own and has been generated by me as the result of my own original research.

I confirm that:

1. This work was done wholly or mainly while in candidature for a research degree at this University;
2. Where any part of this thesis has previously been submitted for a degree or any other . qualification at this University or any other institution, this has been clearly stated;
3. Where I have consulted the published work of others, this is always clearly attributed;
4. Where I have quoted from the work of others, the source is always given. With the exception of such quotations, this thesis is entirely my own work;
5. I have acknowledged all main sources of help;
6. Where the thesis is based on work done by myself jointly with others, I have made clear exactly what was done by others and what I have contributed myself;
7. Parts of this work have been published as: Cusack et al. (2017).

Signed:_____

Date:_____

Contents

List of Tables

List of Figures

Chapter 1

Introduction

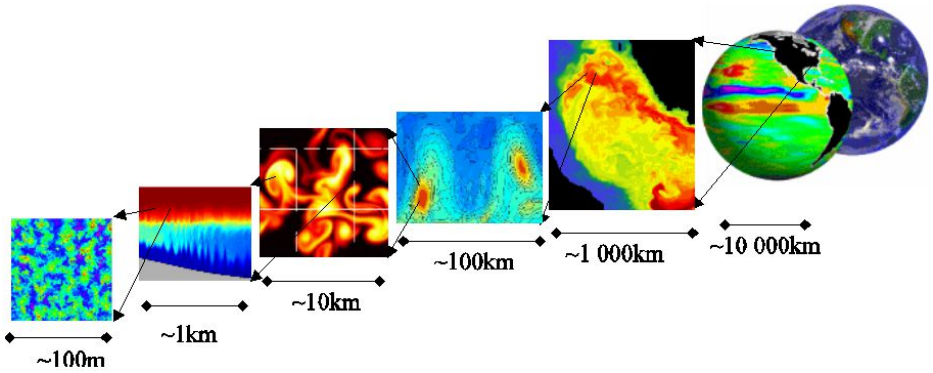

Figure 1.1: Illustration of the scales of geophysical fluid motion, taken from the MITgcm website.

Physical processes in the ocean occur over time and length scales ranging from hundreds of years and thousands of kilometres, down to minutes and millimetres (Figure 1.1). The subtle but profoundly important interaction of large and slow processes, such as the global overturning circulation, with small and rapid processes such as turbulence, is partly what makes oceanographic research both challenging and interesting. The work in this thesis is an observational assessment of interactions between the oceanic mesoscale, having lengths of about 100 km and time scales of weeks to months, with smaller scale processes. Specifically, it considers the propagation and dissipation of an internal wave generated by flow over a sea mount, and the interaction of mesoscale eddies with internal waves in the Scotia Sea. The observations used come from the Diapycnal and Isopycnal Mixing Experiment in the Southern Ocean (DIMES), conducted from 2009 to 2014 in and around the South East Pacific, Drake Passage and Scotia Sea.

This introduction attempts to provide a general context for the following chapters. The first section discusses the Southern Ocean and the important place it holds in the earth system, with a focus on observations from, and modelling of, Drake Passage processes and their connection to the global overturning circulation. The second summarises the relationship between eddies, internal waves and turbulent mixing. The third provides a very brief summary of the Diapycnal and Isopycnal mixing experiment. The final section outlines the thesis structure.

1.1 Southern Ocean dynamics and overturning

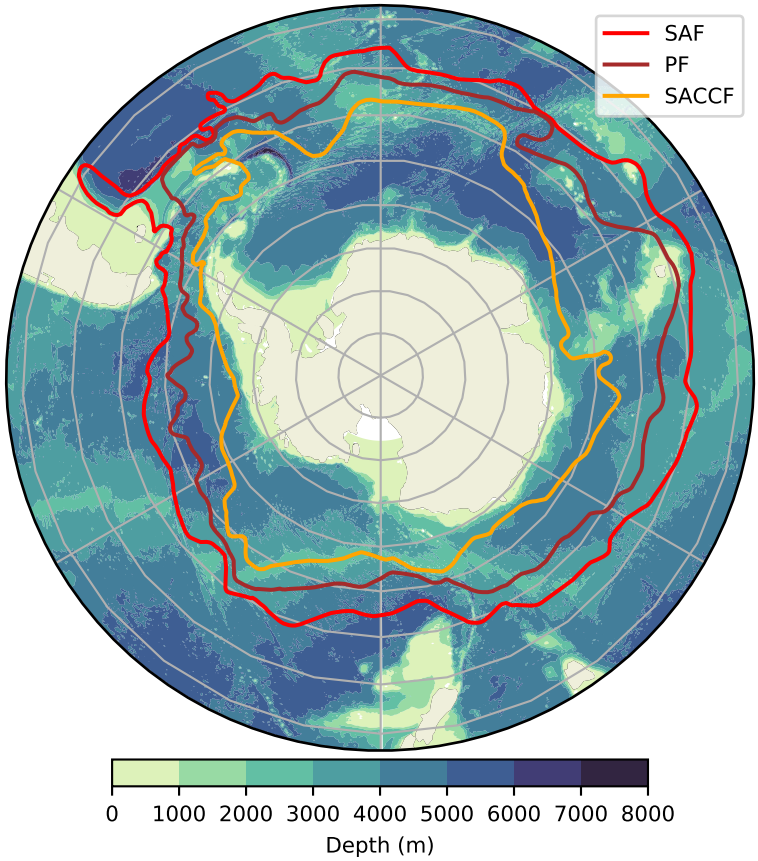

Figure 1.2: Topography of the Southern Ocean (Smith and Sandwell, 1997) with the climatological position of the three main ACC fronts (Orsi et al., 1995).

The de facto official designation of the Southern Ocean, according to the International Hydrographic Organisation's draft 2002 report, is the waters south of 60° S. This thesis takes a more dynamic definition and considers it to include anything close to and south of the Antarctic Circumpolar Current (ACC), a large eastward flowing current connecting the Pacific, Atlantic and Indian ocean basins (Figure 1.2). Such a current can exist because of the lack of any land barrier at the latitude band of the Drake Passage, which opened between 50 and 20 million years ago as the continents of Antarctica and South America separated. It is believed that the appearance of the ACC was associated with significant local and global climate change (Livermore et al., 2007).

In the synoptic picture of the ACC, it is composed of three major fronts, the Subantarctic Front (SAF), the Polar Front (PF) and the Southern Antarctic Circumpolar Front (SACCF) (Orsi et al., 1995), depicted in Figure 1.2. These are both thermodynamic fronts, delineating water masses of contrasting temperature and salinity, as well as regions of steep density gradients and maxima in surface velocity. Estimates of the baroclinic volume transport of the ACC through the Drake Passage generally find values of order 120 - 140 Sv (Cunningham, 2003; Chidichimo et al., 2014), being concentrated mainly in the SAF and PF. More recent analysis suggests the total transport is as high as 170 Sv (Donohue et al., 2016). An interesting finding from these

relatively long term measurements is that transport exhibits significant variability on weekly time scales, but very little on inter-annual scales. The explanation for this thought to lie in the way the ACC responds to long term changes in wind stress and is elaborated on slightly further on in this introduction.

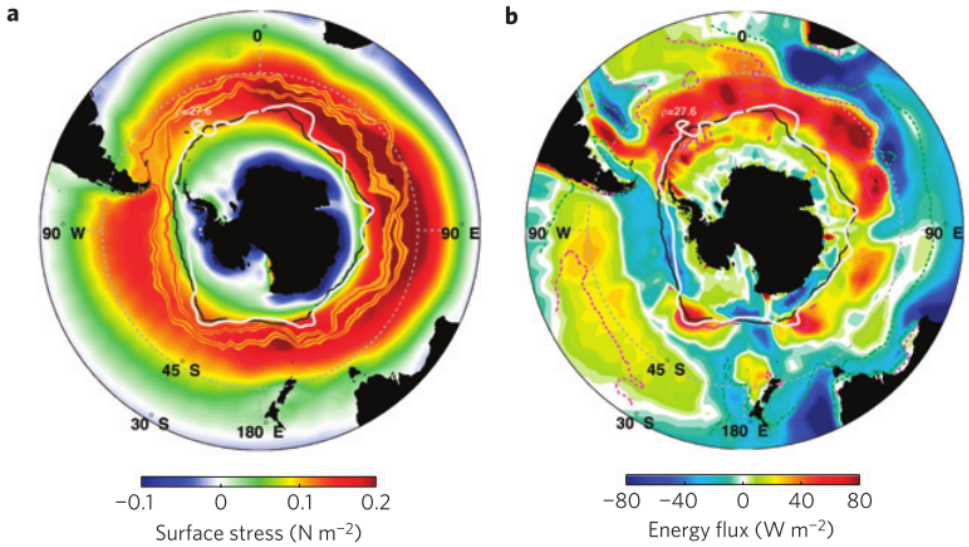

Figure 1.3: a) The mean zonal wind stress, for the period 1980 to 2000 from the National Centers for Environmental Prediction reanalysis. The winter ice edge is marked by the black line and the 27.6 kg m^{-3} outcrop by the white line. The positions of the PF and SAF are marked by orange lines. b) The National Centers for Environmental Predication mean net air-sea heat flux for the same period, including contributions from evaporation and precipitation expressed as a pseudo-heat flux. Negative values indicate a flux out of the ocean. This figure is modified from Marshall and Speer (2012).

The ACC is primarily driven by the combined effects of wind stress and buoyancy forcing at the ocean surface; time mean estimates for both of which are plotted in Figure 1.3. Such is the strength of the winds that blow eastward around Antarctica that sailors gave the latitude bands the names roaring forties and the furious fifties. As well as directly imparting momentum to the ocean, meridional gradients in the wind stress generate divergent and convergent surface Ekman transports, leading to upwelling near the pole, and downwelling at lower latitudes. This tends to tilt density surfaces so that they shoal towards the pole, intensifying the ACC through thermal wind shear. This shoaling can be seen in neutral density sections shown in Figure 1.4b. Observations and models suggest that the strength of the wind stress over the Southern Ocean has increased in recent decades and will continue to do so (Swart and Fyfe, 2012). Idealised models (Hogg, 2010) suggest that the ACC may also be sensitive to changes in buoyancy forcing that have a significant effect on the meridional gradient of density.

In contrast to the time mean picture of the ACC, snapshots of ocean velocity such as those provided by satellite altimetry (Sokolov and Rintoul, 2007) or state estimates that integrate observations into physically consistent numerical model (Mazloff et al., 2010), reveal an enormous amount of mesoscale variability (Figure 1.5). The variability takes the form mobile jets and eddies with horizontal scales of 100 km that extract their energy, via baroclinic instability, from the

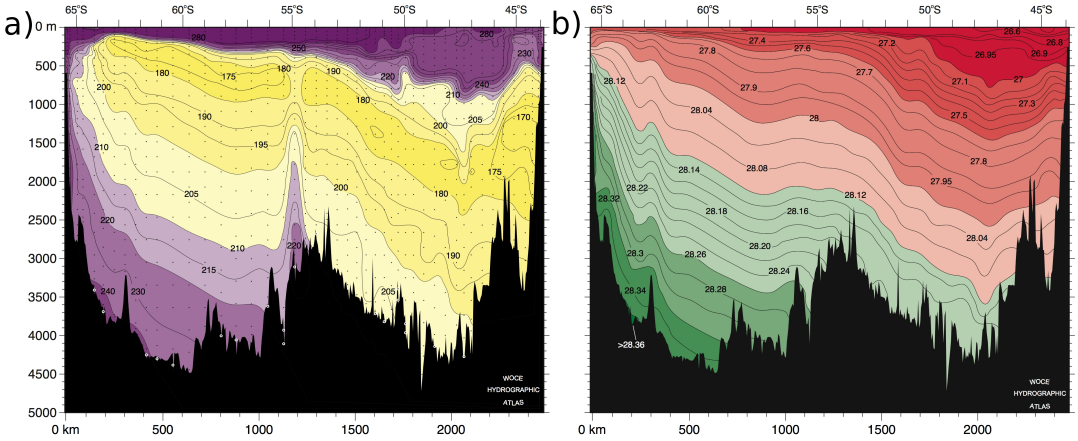

Figure 1.4: Hydrographic sections of a) oxygen concentration and b) neutral density from World Ocean Circulation Experiment line S3 between Australia and Antarctica. Topography is shaded in black.

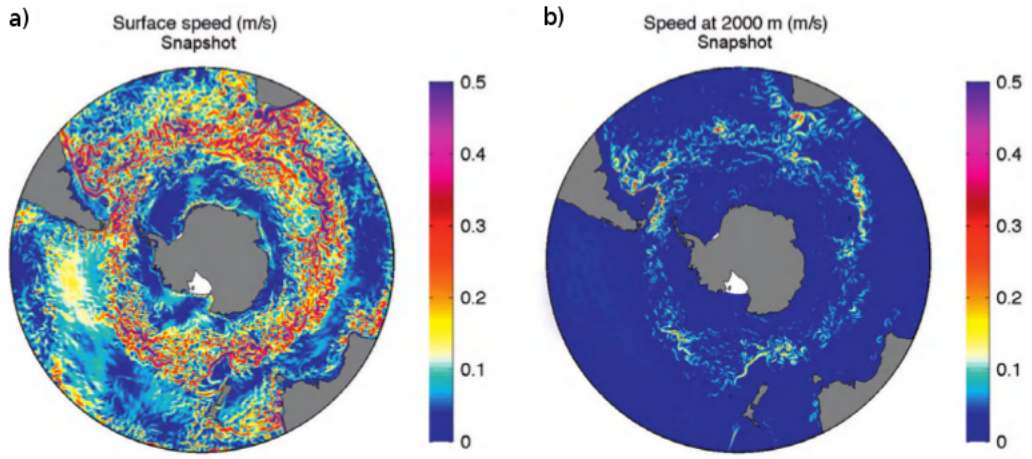

Figure 1.5: Snapshots of flow speed from a) the surface and b) 2000 m depth, from a Southern Ocean state estimate (Mazloff et al., 2010). This figure has been modified from (Rintoul and Naveira Garabato, 2013).

potential energy stored in the tilted isopycnals. Eddies provide the mechanism through which wind stress at the surface is transferred to lower levels of the water column, via a mechanism known as interfacial form stress (Vallis, 2006). Ultimately, wind stress at the surface is balanced by form stress across large bathymetric features. It has been suggested that the explanation for the relative invariance of ACC transport over long time scales lies in the related concept of eddy saturation (e.g. Munday et al., 2013). In summary, changes in wind stress act to increase the baroclinicity of the ACC, which in turn leads to more eddying motions that effectively transfer the stress to the bottom. Recent assessments of the altimetry record suggest that the eddy kinetic energy of the ACC is increasing (Hogg et al., 2015), consistent with the expected responses to changes in the Southern Ocean wind stress.

It is clear from hydrographic sections that a two cell overturning circulation exists in the Southern Ocean. Observations of dissolved oxygen, which is a proxy of water mass age, are shown in Figure 1.4a and provide a good example. Figure 1.6 is a cartoon view of the overturning

based on the observational evidence. Oxygen depleted North Atlantic Deep Water (NADW) flows poleward into the Southern Ocean where it is mixed with waters from the other ocean basins forming Circumpolar Deep Water (CDW). Upper Circumpolar Deep Water (UCDW) reaches the surface along tilted isopycnals and gains buoyancy from the atmosphere, where it is converted into Antarctic Intermediate Water (AAIW) and Subantarctic Mode Water (SAMW), forming the upper cell. Lower Circumpolar Deep Water (LCDW) is also transported to the surface closer to the pole where it loses buoyancy due to sea ice processes and atmospheric heat fluxes and is converted to Antarctic Bottom Water (AABW), creating the bottom cell. Due to its recent contact with the atmosphere, AABW is relatively enriched in oxygen. It experiences significant mixing as it is exported from the Antarctic shelf, as indicated by the small arrows.

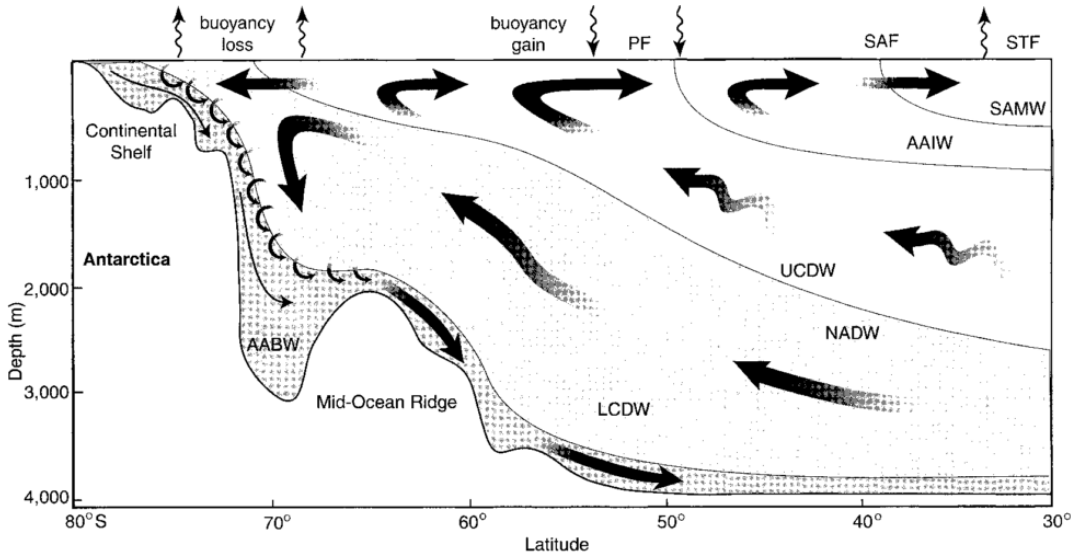

Figure 1.6: A schematic of the Southern Ocean overturning circulation. This figure has been modified from (Speer et al., 2000).

Conceptual understanding of the link between the overturning circulation and eddies has been advanced by residual mean theory (Marshall and Radko, 2003), which is derived from the quasi-geostrophic (QG) zonal mean momentum equations. In this framework, the overturning is found to be the residual of opposing wind and eddy driven components. Importantly, it is also adiabatic away from the surface, occurring along isopycnals which partially does away with the need for large diapycnal mixing coefficients implied by older closure schemes (Munk, 1966). The theory is supported by idealised numerical models (Abernathey et al., 2011), however, its applicability to the real ocean remains questionable since the ACC is not perfectly zonal (Figure 1.2). Recent research suggests that the non zonal, strongly topogrpahically steered, nature of the ACC may be key to understanding transports across it (e.g. Naveira Garabato et al., 2011).

It is difficult to overstate the importance of the global overturning circulation for the Earth's climate. The top of atmosphere energy imbalance has resulted in $\sim 3 \times 10^{23}$ J being accumulated in the climate system over the past few decades, the vast majority of which has ended up in the ocean (Rhein et al., 2013). About 27% of anthropogenic carbon dioxide emitted between 2001 and

2011 was absorbed into the ocean (Le Quéré et al., 2012) and both observations (Sabine, 2004) and models (Frölicher et al., 2015) suggest that the Southern Ocean plays a disproportionately large role in facilitating this sink. Moreover, coupled climate models (Frölicher et al., 2015) indicate that the Southern Ocean is responsible for taking up 75% of the additional heat input into the climate system from 1861 to 2005. A significant amount of uncertainty in projections of future surface warming comes from uncertainty in the efficiency with which the Southern Ocean will continue to uptake heat (Boé et al., 2009).

1.2 Eddies, internal waves and mixing

The previous section highlighted the connection between the overturning circulation and eddies. While eddies can transport properties adiabatically to the surface, above the level of blocking topography, there does not appear to be a similar return pathway for bottom waters. Some amount of interior diabatic transport is still required to explain the observed stratification of the deep ocean, and this necessarily occurs at the scales of molecular diffusion, which are of order 10^{-3} m. Much recent work has been done to understand the mechanisms leading to, and location of, the turbulent motions that facilitate diapycnal diffusion in the ocean (MacKinnon et al., 2013). This section summarises a small portion of the work which is relevant to this thesis, with a focus on the role of internal waves, eddies, and the interaction between the two in the Southern Ocean.

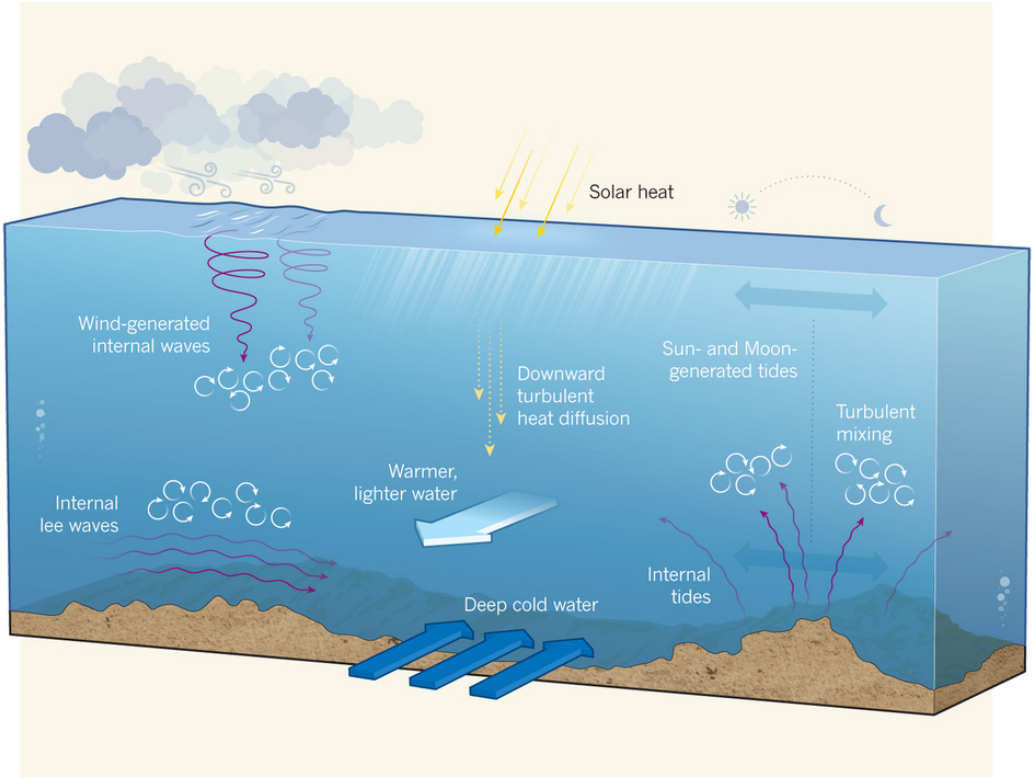

Figure 1.7: A schematic of internal wave generating processes in the Southern Ocean from MacKinnon (2013). The white circular arrows denote mixing caused by wave breaking.

Internal waves are oscillatory motions where buoyancy provides the restoring force that occur in the interior of stratified fluids when density surfaces are perturbed. The most important mechanisms of internal wave generation are atmospheric forcing (Alford et al., 2016), the interaction of tidal currents with topography (Garrett and Kunze, 2007) and the impingement of subinertial motions onto topography (Nikurashin and Ferrari, 2010b). The first two of these processes tend excite waves at near inertial and tidal frequencies respectively, and are readily observed as peaks in the energy-frequency spectrum. The frequency of waves generated by subinertial flow over topography, often called lee waves, depends on the scale of the topography and the speed of the forcing flow. Together these generating mechanisms are thought to provide the majority of the energy supply into the internal wave field. The schematic in Figure 1.7 provides a conceptual summary.

Deep reaching eddy flows that hit topographic obstacles will generate lee waves if the ratio of the flow speed, U, to the horizontal topographic length scale, L, falls between the inertial frequency and the buoyancy frequency. In the Southern Ocean, eddy form stresses effectively transfer horizontal momentum to the deep ocean. Moreover, there exist many regions of rough topography, such as in the Drake Passage. It is expected, therefore, to be a location where lee waves are readily generated. Global estimates of the energy flux into lee waves using modelled velocities (Scott et al., 2011; Nikurashin and Ferrari, 2011) or observed velocities (Wright et al., 2014), combined with climatological stratification and observed bathymetry indicate that many such hot-spots of lee wave generation exist in the Southern Ocean. Very high resolution numerical modelling studies of channel flow over realistic topography (Nikurashin et al., 2012) provide supporting evidence. Globally the energy flux from geostrophic flows into lee waves is estimated to be in the range 0.2 - 0.7 TW (Scott et al., 2011; Nikurashin and Ferrari, 2011; Wright et al., 2014).

Internal wave breaking is thought to be one of the most important mechanisms for generating turbulence in the deep ocean (MacKinnon et al., 2013). Wave breaking occurs when the wave velocity amplitude exceeds its phase speed, leading to a density inversion, and a cascade of instabilities eventually resulting in turbulence (Staquet and Sommeria, 2002). A wave may induce shear instability and turbulence if the gradient Richardson number exceeds a critical value (Miles, 1961; Howard, 1961), however, the oceanographic literature usually refers to this as wave breaking. Waves may also break if they reflect off a solid boundary at a critical angle (Lamb, 2014). When initially formed, waves may not be susceptible to instability, however, weak nonlinear interaction with other waves tends to result in a net transfer of energy to smaller scales (Müller et al., 1986). As the wavenumber (inverse wavelength) increases, waves become more susceptible to shear instability. Constructive superposition of waves may also lead to conditions suitable for breaking.

Direct observations of the rate of turbulent energy dissipation are difficult to make, due to the

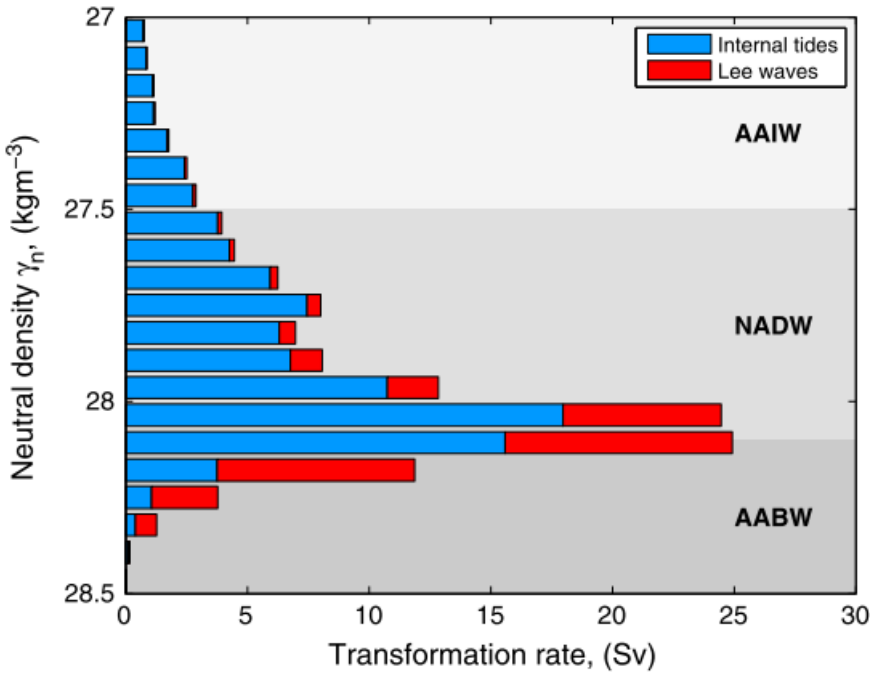

Figure 1.8: Global transformation rate of water as a function of neutral density due to mixing resulting from internal tides and lee waves. From Nikurashin and Ferrari (2013)

small scale at which dissipation occurs and its intermittency. Nevertheless, targeted campaigns in recent years have revealed that dissipation rates in the Southern Ocean increase dramatically over rough topography in the Drake Passage (Watson et al., 2013). One source of this increased turbulence is thought to be the breaking of lee waves forced by the ACC's passage over the many sea mounts and ridges located there. This conclusion is supported by the increase in dissipation with depth (e.g. St. Laurent et al., 2012) coincident with an excess of upward propagating wave energy (e.g. Sheen et al., 2013). Estimates of global transformation rate of waters from denser water classes to lighter ones, shown in Figure 1.8, imply that lee wave driven mixing may play an important role in closing the lower limb of the overturning circulation. Furthermore, Sheen et al. (2014) demonstrated that there may be a connection between eddy kinetic energy and deep mixing on decadal timescales, mediated by lee waves. Chapter 3 adds to this story by presenting the first unambiguous observation of a lee wave in the Southern Ocean.

The second dynamical focus of this thesis is on the transfer of energy from eddies to internal waves away from boundaries. The interaction of a mesoscale strain field with an internal wave field has been shown theoretically to result in a transfer of energy from eddies to waves (Muller, 1976). Internal waves propagating through such a field are distorted, leading to stresses that act to damp the eddy motions. Bühler and McIntyre (2005) show that, if the strain rate is sufficiently high, a situation can occur dubbed the 'shrinking catastrophe'. In this case the strain acts to align wave phase with the direction of maximum strain, and the horizontal and vertical wavenumbers grow exponentially. Eventually this process would be expected to lead to shear instability and turbulence. Observations of wave - eddy interactions are limited, however, Polzin (2010) provides evidence that process is of first order importance in the Northwest Atlantic. Chapter 4 considers

the problem using data from a mooring array in the Scotia Sea.

In summary, there exist several potentially important pathways from energy input at the large scale into small scale turbulence important for water mass transformations. While much progress has been made in recent years, the relative importance of the proposed mechanisms remains difficult to quantify. This is often because in-situ measurements remain scarce, especially in the Southern Ocean, where the weather conditions and distances conspire to make life difficult for oceanographers. Recent advances in autonomous platforms, such as profiling floats (http://www.argo.ucsd.edu/) have increased the volume of available observations tremendously in recent years. Nevertheless, it is still desirable to extract as much possible information from the available observations. Chapter 2 presents the derivation and validation of model of profiling float motion. Vertical velocities derived from this model essential for the analysis of internal waves and turbulence in the subsequent chapters.

1.3 The Diapycnal and Isopycnal Mixing Experiment (DIMES)

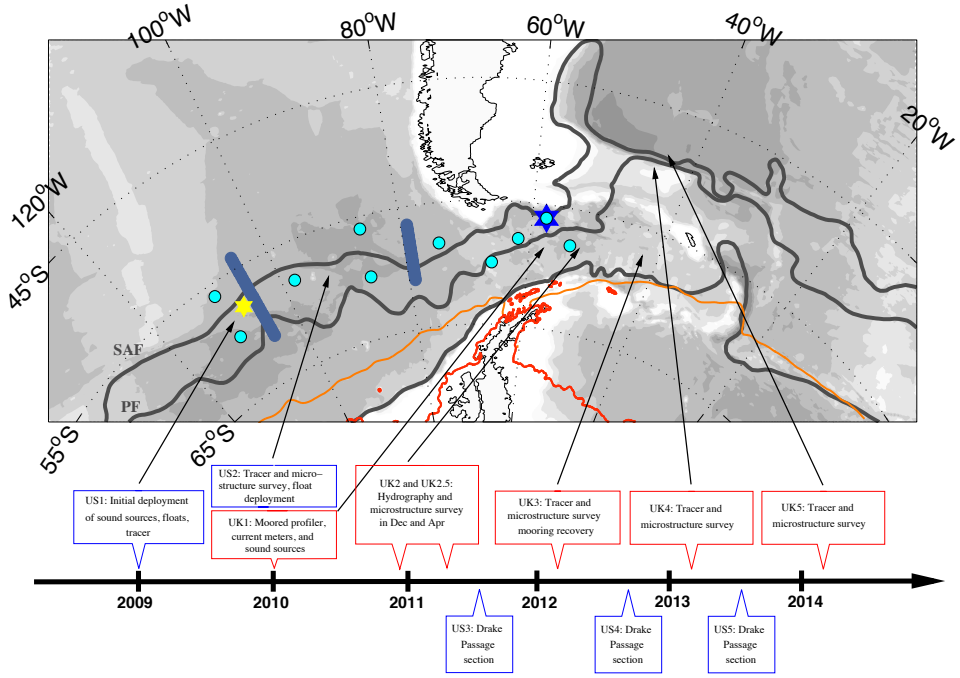

Figure 1.9: The time line of DIMES operations. The yellow star marks the tracer deployment location and the blue star marks the mooring array location.

DIMES was a joint U.S. - U.K. venture to study mixing processes in the Southern Ocean (Gille et al., 2007). It consisted of 11 cruises conducted over 5 years in and around the south east Pacific, Drake Passage, Scotia Sea and Argentine basin, shown in Figure 1.9. The experiment was initiated with the release of 73 kg of trifluoromethyl - sulphur - pentafluoride, an inert and non-toxic tracer, on the 1027.9 kg m^{-3} neutral density surface. The subsequent vertical diffusion and horizontal dispersion of this tracer was studied in great detail. The tracer study

was complemented by the release of over 200 acoustically tracked isopycnal RAFOS floats as well as numerous hydrographic and microstructure surveys. Throughout the course of the experiment, 20 Electromagnetic Autonomous Profiling Explorer (EM-APEX) floats were deployed with the intention of studying upper ocean internal wave and mixing processes. Additionally, a mooring array was operated for 2 years in the Scotia Sea. The EM-APEX floats and mooring array provide the majority of data analysed in this thesis. A full list of publications resulting from the DIMES project can be found at http://dimes.ucsd.edu/en/publications/.

1.4 Thesis structure

Chapter 2 derives and assesses a method for estimating vertical water velocity from profiling floats. The model is then applied to the EM-APEX floats deployed during DIMES, revealing large velocity anomalies. Chapter 3 uses vertical velocities from two of these floats, along with other observations to characterise a large lee wave generated by the flow of the ACC over a sea mount. It is the first direct observation of a lee wave in the Southern Ocean, and is particularly energetic when compared with other such waves globally. Chapter 4 considers the interaction between internal waves and eddies using data from a mooring array. While parts of the analysis are hindered by noise, results suggest that horizontal coupling of eddies and waves is an first order sink (source) of eddy (wave) energy in the Southern Ocean. Chapter 5 summarises the findings of the thesis and provides suggestions for future work.

Chapter 2

Vertical velocity from profiling floats

2.1 Introduction

A large variety of physical processes can lead to vertical flows in the ocean and they are usually distinguished from one another by their speed, location, spatial scale and temporal scale. On scales larger than the Rossby radius of deformation, which varies from 10 km at high latitudes to 100 km near the equator, the ocean is in geostrophic balance to a good approximation. Scaling the geostrophic equations of motions (Olbers et al., 2012) implies that vertical motions are smaller than horizontal motions by a factor of $\beta H/f$ where $\beta = \frac{\partial f}{\partial y} \sim 10^{-11}$ m^{-1} s^{-1}, $H \sim 10^3$ m and $f \sim 10^{-4}$ s^{-1}. An example of a physical process leading to basin scale vertical motion is Ekman pumping or suction induced by large scale curl in mean wind stress. Velocities associated with this process are of order 10^{-6} m s^{-1} (e.g. Hellerman and Rosenstein, 1983). Surface wind stress also generates surface waves and swell, with associated vertical velocities of order 1 m s^{-1}, however, the amplitude of such motion decays exponentially away from the surface. The majority of the oceanic horizontal kinetic energy is concentrated in mesoscale eddies (Wunsch, 1998), and such eddies are known to induce vertical motions of order 10^{-3} m s^{-1} (Klein and Lapeyre, 2009). Similarly, submesoscale eddies and frontal structures also induce a near surface vertical velocity of order 10^{-4} - 10^{-3} m s^{-1}. Internal waves in the deep ocean induce typical vertical velocities of 10^{-3} - 10^{-2} m s^{-1}. This by no means exhaustive list of processes highlights the large range in order of magnitude of vertical speeds that exist. Many of the above physical processes play a role in transporting chemical tracers vertically, with significant consequences for ocean biology and biogeochemistry (e.g. Mann and Lazier, 2006; McGillicuddy, 2016).

The instrumentation required to measure vertical motion depends on the physical process of interest. Only a few techniques make direct measurements with others relying on theoretical approximations of balance or conservation of volume. One example of an instrument capable of making in-situ estimates of absolute vertical velocity is the Lowered Acoustic Doppler Current Profiler (LADCP) (Thurnherr, 2011), which measures the frequency shift of sound pulses reflected off particles suspended in the water. The spatial resolution of the measurements is limited by

the frequency of the pulse, and observations are usually taken at fixed locations along cruise transects. Another example is acoustically tracked neutrally buoyant floats (D'Asaro and Lien, 2000a) which follow the mean flow very accurately. They are Lagrangian when considering flow scales much larger than the instrument itself. Vertical velocity can be estimated from profiling instruments such as gliders (Merckelbach et al., 2010; Frajka-Williams et al., 2011) and floats (Cusack et al., 2017) by measuring deviations from their expected vertical profiling speed. This requires an accurate flight model for the instrument. The methods described above are typically not more accurate than 10^{-2} - 10^{-3} m s^{-1} and are only suitable for measuring physical processes such as internal waves, convective plumes and large turbulent overturns which produce sufficiently large velocities.

Other indirect methods, using approximations of the fluid dynamical equations and measurements of temperature and salinity can be applied to a variety of instruments such as moorings (e.g. Bryden, 1980; Sévellec et al., 2015) and floats (Phillips and Bindoff, 2014) to estimate quasi-geostrophic velocities. The velocities inferred are smaller, but their accuracy relies on the validity of the underlying theory. Despite the gradual increase in methods available over the past decades, a thorough review of the subject does not, to my knowledge, exist yet and accurate observations of oceanic vertical velocities remain relatively scarce.

This chapter covers the derivation and evaluation of a method for estimating vertical velocity from profiling floats, specifically EM-APEX floats, but in principle any similar profiling float. It is largely the same as reported in (Cusack et al., 2017), with an expanded derivation of the float model and additional results for all 20 floats deployed during DIMES. Following this introduction is a description of the floats to which the method is applied, derivation of the theory, validation and quantification of uncertainties. Vertical velocities estimated using this method underpin many of the results presented in Chapter 3.

2.2 Method

2.2.1 EM-APEX floats

EM-APEX floats, depicted in Figure 2.1 are a type of neutrally buoyant profiling float designed to make oceanographic measurements over periods of days to years. They were developed at the Applied Physics Laboratory, University of Washington, in collaboration with Teledyne Webb Research Corporation. The EM modification consists of electrodes on the outer casing that measure the potential difference across the instrument induced by the motion of the instrument and ocean through the vertical component of the Earth's magnetic field (Sanford, 1971). This information, along with measurements of instrument tilt and magnetic compass heading, is used to calculate relative horizontal water velocity with a characteristic precision of 1 cm s^{-1} (Sanford et al., 2005). Relative velocity is converted to absolute velocity by using surface GPS positions

to estimate a depth-independent constant offset (explained in Section 3.2.2). As well as velocity, the floats also measure conductivity, temperature and pressure using a Seabird Electronics SBE-41 pumped CTD. All recorded measurements and GPS positions are communicated via Iridium satellites while at the surface.

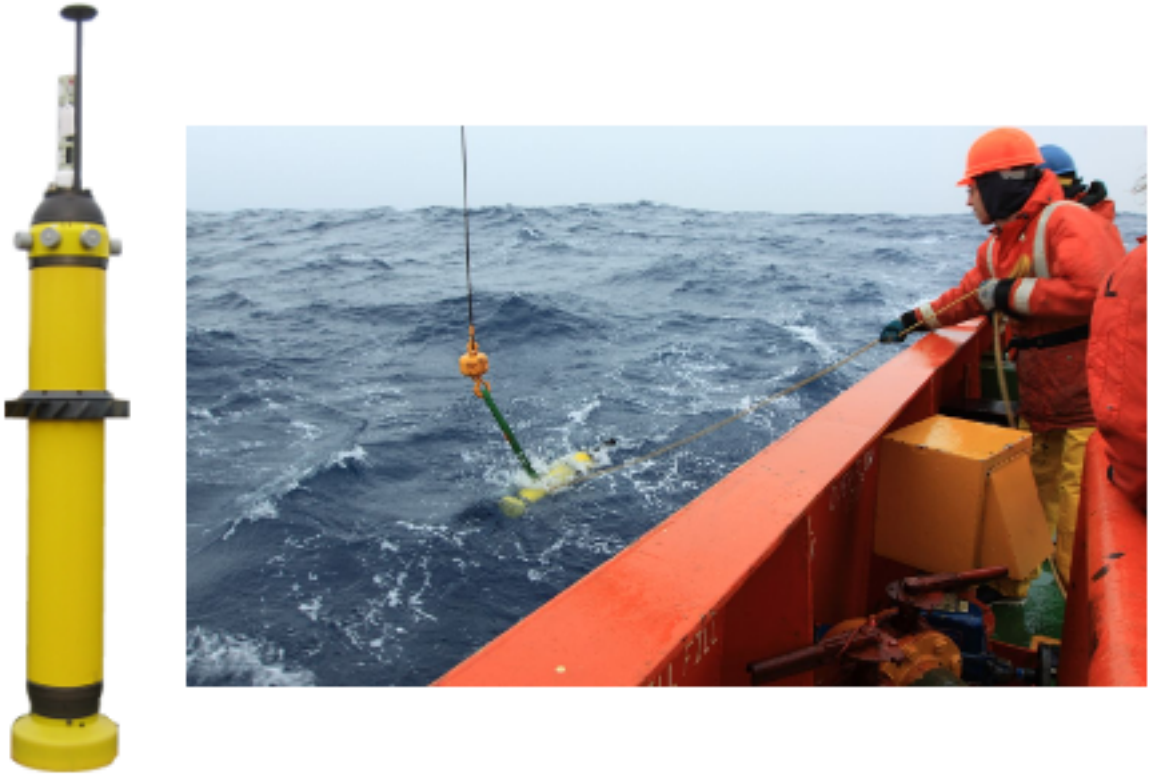

Figure 2.1: An EM-APEX float and one being deployed in the Drake Passage.

The floats change their buoyancy by pumping oil into and out of an external bladder using a piston. The position of the piston is proportional to the volume of oil in the bladder and is recorded throughout a profile. The floats deployed during DIMES were programmed to change their buoyancy in such a way as to maintain an approximately constant vertical speed of 12 cm s^{-1}. This aspect of float engineering is important when it comes to estimating vertical velocity. The floats were also programmed to perform profiles at half inertial periods so that near inertial motions could be easily filtered from horizontal velocity profiles (Kilbourne and Girton, 2015).

During DIMES 20 EM-APEX floats were deployed and all except one started their mission successfully. Prior to deployment floats were ballasted so that they can profile over an appropriate range of pressures and remain neutrally buoyant at some depth. The typical maximum profiling depth used was 1500 to 2000 m. The following sections as well as Chapter 3 concern themselves mostly with two particular floats, labelled 4976 and 4977. These were special because, unlike other floats, they profiled continuously without parking. Other floats are covered at the end of this chapter.

2.2.2 Derivation of a model for float vertical motion

The theoretical underpinnings of the motion of a float of finite size in a stratified fluid are described in detail by D'Asaro et al. (1996) and summarised here. The Boussinesq approximation is made, meaning that the float is taken to be incompressible except when considering terms involving gravity. The equation of motion for a float with mass M, volume, V, and velocity, $\mathbf{u}_f$, is

$$\rho_f \frac{\mathrm{d}\mathbf{u}_f}{\mathrm{d}t} = \mathbf{g}(\rho_f - \rho) - \overline{\boldsymbol{\nabla} p} + \oiint_{S(V)} (-(p^* - \overline{p})\hat{\mathbf{n}} + \mu \boldsymbol{\nabla} \mathbf{u}^*) \cdot \hat{\mathbf{n}} \, \mathrm{d}S \tag{2.1}$$

where ρ_f is the float density, $\frac{\mathrm{d}}{\mathrm{d}t}$ is the material derivative, $\mathbf{g}$ is the gravitational acceleration, ρ the water density, p is the pressure, p^* the pressure field generated due to the presence of the float, μ the molecular viscosity, $\mathbf{u}^*$ is the additional velocity field generated by the float, $\hat{\mathbf{n}}$ the unit vector normal to the float surface element $\mathrm{d}S$. An over bar denotes an average over the float volume. The first term on the right hand side quantifies the acceleration due to buoyancy, proportional to the difference in density between the float and the surrounding water. The second term is the effect of large-scale non-hydrostatic pressure gradients on the float. The final integral term encompasses the combined effects of form drag and skin friction over the surface of the float. The form drag is the result of pressure gradients across the float, due to the motion of the float in the water. Skin friction results from viscous stresses in the thin boundary layer around the float.

We assume that the Reynolds number is large enough that skin friction can be neglected, which justifies a simple functional form of the form drag as proportional to $(u_f - u)^2$. The float also experiences an additional drag force when accelerating, known as the added mass force, which is a function of the difference in acceleration between the float and the surrounding fluid. We neglect completely the force arising from changes in the turbulent wake and viscous boundary layer due to acceleration, often called the Basset force.

Consider the vertical component of Equation (2.1) after dividing by the float density and substituting the appropriate drag formula (Batchelor, 2000),

$$\frac{\mathrm{d}w_f}{\mathrm{d}t} = \mathbf{g}(1 - \frac{\rho}{\rho_f}) - C_D \frac{A}{V} |w_f - w|(w_f - w) + F_{am} \tag{2.2}$$

where C_D is a dimensionless drag coefficient and A the cross sectional area of the float and F_{am} is the added mass force. The first term on the left scales as W_f/T, the second as $g\Delta\rho/\rho_f$, the third as W_f^2/H_f and the final as W_f/T. Typical values are, $W_f = 0.1$ m s^{-1} for the float speed, $T = 10^3$ s for the large scale flow time scale (although this would have to be reduced for times when the piston position changes), $g = 10$ m s^{-2}, $\Delta\rho = 1$ kg m^{-3}, $\rho_f = 1000$ kg m^{-3}, $w = 10^{-2}$ m s^{-2} and $H_f = 1$ m. That leads to the following order of magnitude estimates, $W_f/T = 10^{-4}$, $g\Delta\rho/\rho_f = 10^{-2}$, $W_f^2/H_f = 10^{-2}$ and $W_f/H = 10^{-4}$. This implies that the leading order balance

is between drag and buoyancy. Occasionally, acceleration and added mass may be important on small time scales, for example when the piston position changes, but most of the time they will be small.

The aim of the derivation is to find the water velocity, w. After neglecting the effect of acceleration and added mass and multiplying by the float volume, the equation becomes,

$$-g(M-\rho V)+C_D\rho A|w_f-w|(w_f-w)=0 \tag{2.3}$$

which is essentially a quadratic equation for w that can be solved numerically using standard minimisation routines. Many of the variables in this equation are known or measured directly by the float. The density of water is measured leaving one unknown variable, and several unknown constants. The unknown variable is the float volume, and it is therefore necessary to formulate another equation that describes changes in volume as a function of pressure, temperature and piston position, effectively an equation of state. The unknown, or poorly known constants are the drag coefficient and coefficients that go into the equation of state.

Float volume is assumed to change linearly with pressure, p and piston position k,

$$V=V_0(1+\alpha_p(p-p_0))+\alpha_k(k-k_0), \tag{2.4}$$

where V_0, p_0 and k_0 denote the volume, pressure and piston position at the ballast point. Variables α_p and α_k are the coefficient of compressibility and the change in volume with piston position, respectively. We have neglected the effects of thermal expansion because they are difficult to separate from those of pressure, since in the Scotia Sea both sets of effects cause a decrease in volume with depth. Variations in temperature during profiles do not typically exceed 5 °C, and if a thermal expansion coefficient of 3.6×10^{-5} °C^{-1} (as quoted in the technical specifications for EM-APEX floats) is assumed, then thermal changes in volume over a profile are typically one order of magnitude smaller than compressive changes, and thus can justifiably be neglected.

Equations (2.3) and (2.4) need to be solved to diagnose the water velocity. First, we simplify the equations further.

2.2.3 Steady ocean approximation

Following previous work on the estimation of oceanic vertical flow from gliders (Merckelbach et al., 2010; Frajka-Williams et al., 2011), we can simplify the equations of motion by considering the motion of a float in a steady ocean. The steady approximation is valid if the the rate of change of vertical water velocity is small, $\frac{\mathrm{d}w}{\mathrm{d}t}\sim 0$. After optimisation of the model parameters,

absolute vertical water velocity, w, is estimated as the difference between the measured float vertical velocity, w_f, and the steady vertical velocity that it is predicted to have in steady water, w_s,

$$w = w_f - w_s, \tag{2.5}$$

where $w_f = \frac{dz_f}{dt}$. Float height, z_f, is determined from pressure and latitude using the TEOS-10 package. Both w_s and w_f have an order of magnitude of 10 cm s^{-1} and the vertical velocity is the difference between two similar values. In order to determine w_s, it is necessary to solve the steady equation of motion of the float,

$$M\frac{dw_s}{dt} = g(M - \rho V) - \rho C_D A|w_s|w_s, \tag{2.6}$$

with

$$\frac{dz_s}{dt} = w_s, \tag{2.7}$$

where z_s is the float height in steady water. Here we have neglected the complication of the added mass effect, although it may be important. It is necessary to solve the system of differential equations described by Equations (2.6) and (2.7) to fully diagnose w_s. However, accelerations of the float are assumed to be very small, setting $\frac{dw_s}{dt} = 0$, the equations can be simplified.

Given a steady-state assumption, Equation (2.6) can be rearranged for w_s as

$$w_s = \mathrm{sgn}(\rho V - M)\sqrt{\frac{|g(M - \rho V)|}{\rho C_D A}}. \tag{2.8}$$

One further adjustment to the model is to use a different drag coefficient for ascents and descents. Where this is done, the coefficients are denoted $C_D^{(\mathrm{u})}$ and $C_D^{(\mathrm{d})}$. The justification for doing this is that the base of the float is flat whereas the top consists of antenna and sensors (see Figure 2.1) and the drag coefficient is likely to depend on direction of motion. Such a modification is not made for most of the results discussed in this thesis, however, it is made in Section 2.3.3 at the end of this chapter.

2.2.4 Optimisation routine

The steady model contains 7 parameters (or 8 if two drag coefficients are used), of which mass, ballast piston position and ballast pressure are known, having been measured or set prior to deployment. The float diameter is 16.5 cm, giving a cross-sectional area of 0.02 m^2 that is

assumed to remain constant with depth. In subsequent calculations the area is combined with the drag coefficient into a single parameter, C_D^*, the value of which is not initially known. The remaining parameters are optimised by minimising the following cost function for vertical water velocity variance over many profiles,

$$\sum_t w(t)^2 \tag{2.9}$$

where $w(t)$ denotes any absolute water velocity measurement at time t regardless of depth. This cost function follows from conservation of volume in an incompressible fluid, which is a very good approximation for the entire ocean, but is also assumed to hold over the smaller spatial and time scales covered by a float. We defer to Frajka-Williams et al. (2011) for a more thorough discussion of cost functions. In summary, they assessed four and found that one was as effective as (2.9), while two were worse and did not produce physically consistent results. The upper 60 dbar of each profile is excluded when performing the optimisation since both the float and water experience strong accelerations near the surface, invalidating the assumptions of the model. It is possible that parameter values may change over the lifetime of a float, for example the drag coefficient can change as a result of biofouling (Merckelbach et al., 2010).

2.3 Results

2.3.1 Floats 4976 and 4977

Standard least squares methods were used to perform the optimisation separately for floats 4976 and 4977, using 150 profiles shortly after the observation of a large lee wave. Parameter estimates from technical specifications were used as initial values. Profiles to optimise to were chosen so that the model would be reliable at the time of the wave observation, while also keeping the observations independent from the model parameters. Uncertainties were estimated by repeating the optimisation many times on random sub-samples of the chosen profiles, to build a distribution of possible parameters from which the standard deviation was calculated. The resulting parameters and their uncertainties are summarised in Table 2.1, along with values expected from technical specifications. Over a small range of parameter values close to the optimum, C_D^* and α_k co-vary with compensating effect on vertical velocity. This may result in a somewhat unrealistic, albeit small, difference between floats.

A time series of the terms in Equation (2.5) are displayed in Figure 2.2 for five profiles from float 4976. It can be seen that the steady velocity has much less high frequency variability than the measured float velocity. Large changes in steady velocity only occur when the float piston position is adjusted leading to a change in buoyancy.

Table 2.1: Vertical velocity model parameter estimates after optimisation for the two floats are displayed in the latter two columns, including the one standard deviation uncertainty. Expected values come from technical specifications for EM-APEX.

Parameter	Units	Expected	Float 4976	Float 4977
V_0	10^{-2} m^3	2.62	2.62 ± 0.0	2.62 ± 0.0
C_D^*	10^{-2} m^2	2.9	3.5 ± 0.6	2.2 ± 0.4
α_p	10^{-6} dbar^{-1}	3.67	3.6 ± 0.3	3.8 ± 0.2
α_k	10^{-6} m^3	1.156	1.5 ± 0.3	1.0 ± 0.2

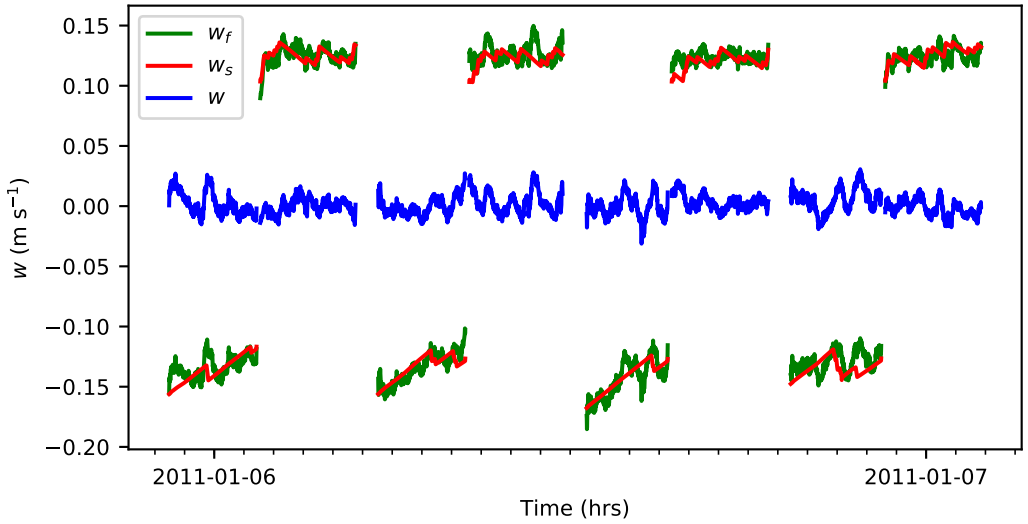

Figure 2.2: Time series of measured velocity w_f, steady velocity w_s and the vertical velocity estimated as the difference of the two for float 4976, profiles 51 to 58. Data from the upper 60 dbar have been removed.

2.3.2 Validation and uncertainties for floats 4976 and 4977

Without independent measurements of vertical velocity with which to compare, only a limited validation of the model is possible. The first check is the distribution of vertical velocities, which should be centred on zero, as constrained by the optimisation procedure. Figure 2.3 shows the distribution of measurements. This closely approximates a Gaussian distribution with a mean of 0.0 mm s^{-1} and a standard deviation of 9 mm s^{-1}. In total, 51% of velocities are less than 1 cm s^{-1}.

The Garrett - Munk (GM) spectrum (e.g. Gregg and Kunze, 1991) provides an estimate of the expected internal wave induced variance of several physical quantities, including vertical velocity or vertical kinetic energy (VKE) (Thurnherr et al., 2015) as a function of vertical wavenumber.

$$\mathrm{VKE}(m) = \pi E_0 b N f j_* \frac{1}{(m + m_*)^2}, \tag{2.10}$$

where the nondimensional spectral energy level $E_0 = 6.3 \times 10^{-5}$; b is the stratification e-folding scale taken as 1000 m in the Drake Passage (Thurnherr et al., 2015); j_* is the peak wave number, which quantifies the bandwidth of the internal wave field; $m_* = j_* \frac{\pi N}{b N_0}$; and $N_0 = 5.3 \times 10^3$ rad s^{-1}.

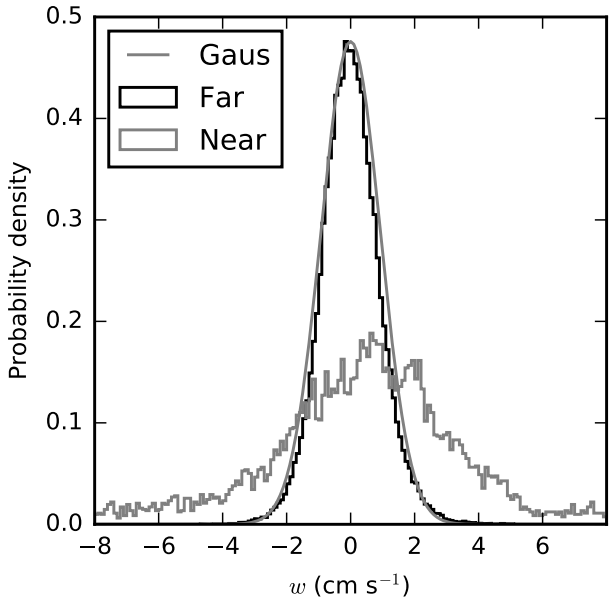

Figure 2.3: Histogram of vertical velocity measurements from depths greater than 50 m. The results from both floats have been combined. The black histogram contains observations from the far field that were used to optimise the velocity model. The grey histogram contains observations from the area of the wave observation, the same profiles displayed in Figure 3.6. A Gaussian with zero mean and 0.9 cm s^{-1} standard deviation is shown for reference.

Analysis of vertical velocity from LADCP measurements (Thurnherr et al., 2015) find that such a spectrum holds in many regions of the ocean, spanning a range of latitudes, up to a limiting wavenumber. The average VKE spectrum from the two floats, computed from 100 profiles distant from the observed wave, is compared to the GM spectrum in Figure 2.4. In general the GM spectrum with default parameter values is about a factor of 2 more energetic than the measured average spectrum but is still encompassed by the spread of individual profile spectra, denoted in the figure by faint grey lines. Measured energy levels decline from large to small vertical scales at a rate that is consistent with the power law proportional to m^{-2} over the wavenumber range 0.03 to 0.2 rad m^{-1}. A notable deviation from this power law includes a broad peak at 0.02 rad m^{-1}. This is likely caused by processes with a time scale of $2\pi/N$ aliasing the spatial signal, since for a float travelling at $w_f \approx 0.12$ m s^{-1}, and $N \approx 2 \times 10^{-3}$ rad s^{-1}, $N/w_f \approx 0.02$ rad m^{-1}.

The standard deviation in vertical velocity from different choices in model parameter, estimated from the distributions generated when optimising the model, is 1 mm s^{-1}. This is an uncertainty that manifests as a constant bias in the profile velocity. An additional uncertainty of 1 mm s^{-1} at high frequencies is caused by random noise the pressure sensor. The final source of uncertainty is introduced by a systematic bias in the model as a result of necessary simplification of float dynamics. A test on the accuracy of the steady model was performed by solving the fully time-dependent equations of motion and comparing to the time-independent solution (not shown). The difference between solutions was found to be greatest where the float was undergoing acceleration, such as at the beginning and end of profiles, and when the piston was moved to alter buoyancy. Synthetic profiles of density and pressure were generated, and the time response of the

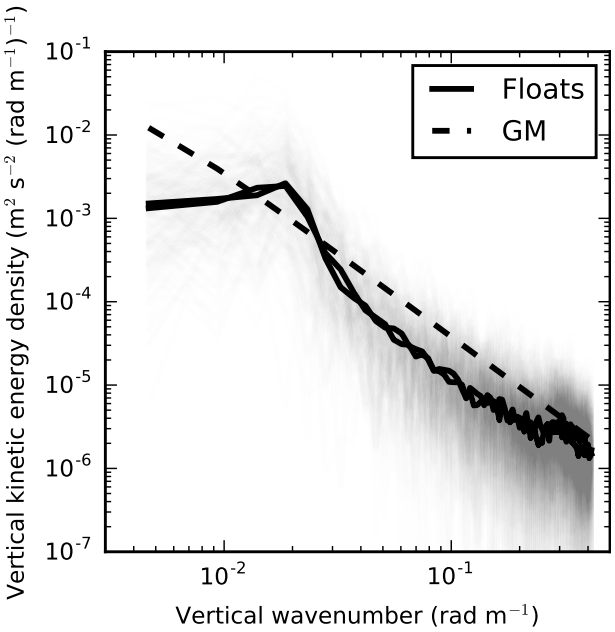

Figure 2.4: Vertical kinetic energy spectrum from 100 profiles each from both floats (faint grey shading), as well as the mean (solid black) plotted against vertical wavenumber. The peak at 0.02 rad m^{-1} is likely caused by aliasing. The reference GM spectrum is also shown (dashed black).

equations to a step change in piston position was assessed. It was found that the float reached 99% of the new terminal velocity after 15 s, corresponding to a vertical distance of less than 1.5 m, which is smaller than the characteristic sampling distance. Thus, for measurements of processes changing on time scales longer than this adjustment time or over larger vertical distances, the no acceleration assumption is justifiable.

2.3.3 Results for all floats

When fitting the vertical velocity model to all floats, the drag coefficient was separated into upward and downward components. This model was also fitted to the two floats previously discussed, 4976 and 4977. The outcome of the fitting procedure as well as the estimated parameter values are displayed in Table 2.2. The model was successfully fitted to 12 out of the 20 floats. A successful fit is one in which the the cost function is minimised resulting in a Gaussian distribution of velocities about zero, similar to Figure 2.3. This metric is not sufficient to determine whether the fit is 'good' in a more subjective sense. Inspection of vertical velocity plots from individual floats reveals that those meeting the successful criteria show non-physical characteristics, including a dipole-like distribution of vertical velocity. Figure 2.6 shows the velocity section for float 4814 where it can be seen that velocities are excessively positive at the beginning of the section and negative at the end. The appearance of this phenomena implies that parameter values may be changing significantly over the lifetime of the float. The reason for this is not known but possibilities include biofouling and wear and tear.

Out of the 12 floats for which the optimisation was successful, 6 do not display a bipolar

Table 2.2: Outcome and parameter estimates after fitting vertical velocity model to all DIMES floats. Outcomes are U, unsuccessful, S, successful, D, dipole velocity structure, L, evidence of vertical velocity in excess of 10 cm/s. The parameters are volume V_0 (m^3), ascending drag coefficient $C_D^{(u)}$ (m^2), descending drag coefficient $C_D^{(d)}$ (m^2), compressibility α_p ($dbar^{-1}$) and piston coefficient α_k (m^3). A row highlighted in bold indicates the model fit was successful and no dipole was observed.

Float	Outcome	V_0	$C_D^{(u)}$	$C_D^{(d)}$	α_p	α_k
3767	U	0.0261	0.02	0.02	3.67e-06	1.16e-06
4086	U/D	0.0262	0.0262	0.0235	3.9e-06	1.11e-06
4087	S/D	0.0262	0.0254	0.0253	3.9e-06	1.11e-06
4089	U	0.0261	0.00754	0.0224	4.35e-06	6.28e-07
4090	S/D	0.0262	0.0231	0.0253	3.74e-06	1.13e-06
4594	S/D	0.0262	0.0253	0.0198	4.1e-06	8.96e-07
4595	U	0.0262	0.0329	0.0232	3.72e-06	1.26e-06
4596	U	0.0262	0.0566	0.00396	4.94e-06	1.59e-06
4597	U/D	0.459	429	327	-0.000838	0.0183
4812	S/D	0.0261	0.0341	0.0422	2.92e-06	1.7e-06
4813	U/D	0.0209	2.41	2.16	-0.000137	9.85e-05
4814	S/D	0.0262	0.0217	0.0228	3.71e-06	9.85e-07
4815	U/D	0.0262	0.0249	0.0211	3.78e-06	9.86e-07
4976	**S/L**	**0.0262**	**0.0836**	**0.0794**	**1.58e-06**	**3.53e-06**
4977	**S/L**	**0.0261**	**0.0666**	**0.0669**	**1.46e-06**	**2.92e-06**
6478	**S**	**0.0263**	**0.019**	**0.021**	**3.69e-06**	**8.41e-07**
6480	**S/L**	**0.0262**	**0.0455**	**0.0489**	**2.51e-06**	**1.99e-06**
6481	S/D	0.0262	0.0358	0.037	3.08e-06	1.52e-06
6625	**S**	**0.0262**	**0.0567**	**0.0571**	**2.27e-06**	**2.41e-06**
6626	**S/L**	**0.0262**	**0.0193**	**0.0205**	**3.91e-06**	**8.49e-07**

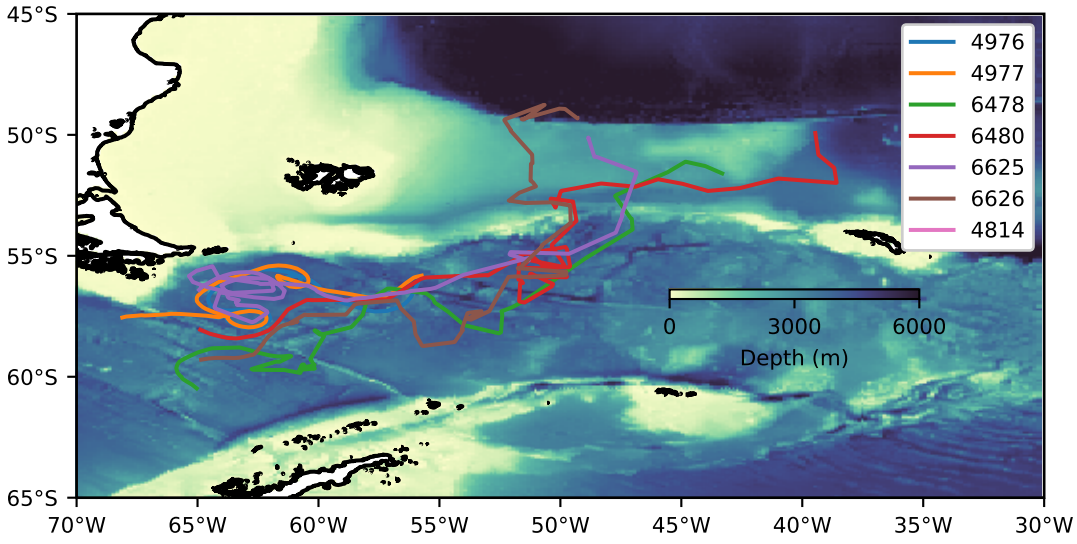

Figure 2.5: Map of float trajectories.

distribution of velocities. The trajectories of these floats are plotted in Figure 2.5 and velocity sections are displayed in Figures 2.7 to 2.12. Even for these floats the spread of parameter values is considerable for all parameters except the volume, with the largest parameter estimate being a factor of 4 to 5 times the smallest. Such significant variance between floats is surprising and it cannot be explained by differences in float manufacturing alone. For individual floats, the difference between upward and downward drag coefficients is smaller than the uncertainty on the

values, which increases confidence in the single drag parameter model used previously.

Insight into the spread of parameter values for a particular float can be gained from Figure 2.13. It has been produced by plotting the distribution of parameter values gained from a bootstrapping method against each other. There exists a strong degree of correlation between certain parameter pairs, in particular, the compressibility with the piston coefficient and the drag coefficients with the volume. Insight into the spread of parameter values between different floats can be gained from Figure 2.14. The parameters for this float display a bimodal distribution. The red vertical line in each histogram denotes the optimised parameter using all data (the same value as given in Table 2.2) and the green line denotes the expectation from technical specifications. This is evidence that there exist two local minima in the cost function which the optimisation routine cannot easily distinguish between. All floats highlighed in bold in Table 2.2 for which the compressibility is less than 3×10^{-6} dbar^{-1} display the same bimodal distribution (not shown). The spread of these results also implies that the model is under constrained by the data.

2.4 Discussion and conclusions

A theoretical model of float vertical motion has been derived and applied to EM-APEX floats deployed during DIMES. The goal of this process was to produce estimates of absolute vertical water velocity. This goal was achieved for 6 of the 19 successfully deployed floats, 4 of which detected large vertical velocity anomalies. The model was derived from the equations of motion for a float immersed in a fluid and simplified by assuming that accelerations of both the water and the float were negligible, and that the Reynolds number of the flow around the float was sufficiently large to justify a simple analytical form of the drag equation. The model relies on an assumed form of the equation of state for the float, which contains several poorly known parameters. It was necessary to optimise these parameters by minimising a cost function based on the expected large scale statistics of vertical velocity. After optimisation, the model uses the observed variables, pressure, time, piston position and density to estimate the expected steady float velocity which is then subtracted from the measured float velocity to produce the vertical velocity estimate.

Analysis of the model uncertainties focused on two floats in particular, 4976 and 4977, which were unique because of their continuous profiling strategy and provide the much of the data used in the next chapter. The total error in the final vertical velocity estimate is a combination of measurement errors, model parameter uncertainty and error resulting from simplifying assumptions in the underlying theory. The total error is estimated to be 1 - 2 mm s^{-1} under normal conditions, increasing at certain points during a profile where the float undergoes accelerations, such as when the piston is moved to alter the buoyancy. Additional confidence in the use of a single drag parameter, rather than two, is found in the fact that when optimising the two drag parameter model, the two coefficients are within 1 standard deviation. Confidence in the final

velocity results is boosted by the generally good agreement of the spectrum of vertical kinetic energy with Garrett-Munk expectations, although evidence of temporal aliasing is present. The final error in the measurements is very similar to that of the gliders assessed by Merckelbach et al. (2010) and Frajka-Williams et al. (2011).

Application of the model to all the DIMES floats produced mixed results. For 8 of the floats, the optimisation procedure did not succeed. The reasons for this remain unknown and would require a thorough examination of the data being supplied to the model for each float individually. The heterogeneous nature of the sampling strategy of individual floats made developing an automated algorithm for fitting them all difficult. The development of the more complex algorithm or methods tailored to individual floats would be an easy avenue for future work.

A more challenging issue is the unphysical change in depth mean vertical velocity with time observed in 9 floats. The reason why this occurs remains unknown. Possible reasons include 1) biofouling, whereby the growth of organisms on the outer casing change the drag coefficient 2) wear and tear leading to changes in float dynamics, 3) the cost function being too simple a constraint. If the problem is due to boifouling or wear and tear, it could be solved by fitting the model to smaller sections of float data or by modifying the model to allow for temporal changes in the parameter values. The latter option does not seem like a good one, since there is evidence that the model is already under constrained, since for several floats it displays multiple local minima in the cost function and strong correlation of variables. Some of this correlation has arisen by construction, since the model has not been reduced to its minimum number of parameters by rearranging the equation and combining terms. This was a deliberate choice, since we prefer to keep parameters that have a physical meaning. A more thorough exploration of alternative cost functions would be a worthwhile, and could rule out the cost function as the cause.

Of the 6 floats to which the model was successfully fitted and showed no unphysical velocity structure, 4 detected large oscillations in vertical velocity exceeding 5 cm s^{-1} while 3 exceeded 10 cm s^{-1}. Observations of such large vertical velocities are relatively rare in the deep ocean and the following chapter focuses in depth on phenomena leading to their generation.

The ARGO program (http://www.argo.ucsd.edu), as of 15th June 2017, consists of 3868 autonomous profiling floats many of which are very similar in design to the EM-APEX floats described in this chapter. Data from parked ARGO floats has already shown to be useful for investigation internal waves by estimating vertical isotherm displacement (Hennon et al., 2014). A major requirement is that the floats provide the internal engineering variables required to calculate float volume, in particular the piston position (or equivalent for different floats) and that they return an accurate time stamp of each measurement. If the requirements are met, ARGO presents a large new potential dataset for examining vertical motion in the ocean.

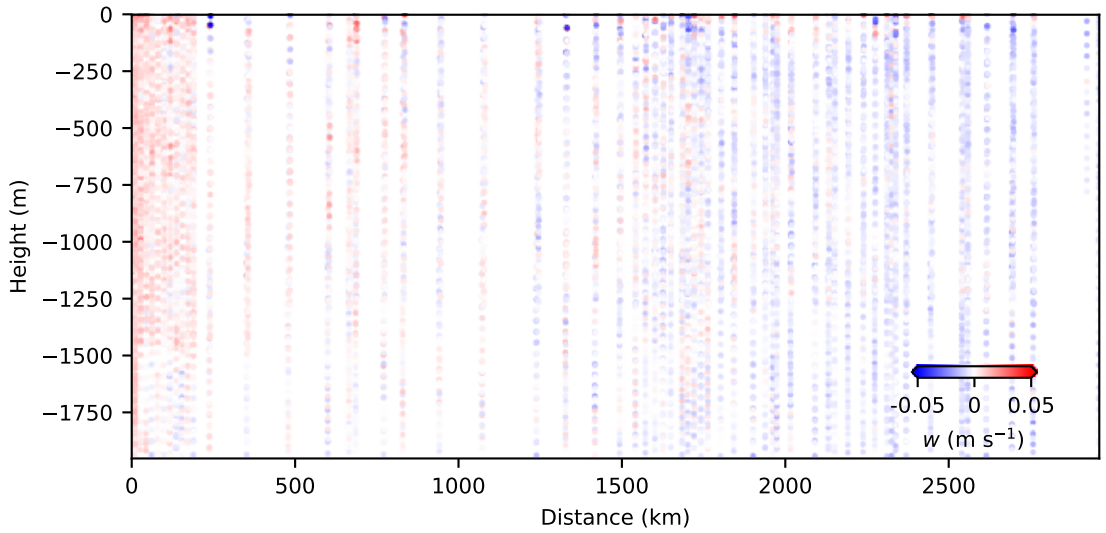

Figure 2.6: Vertical velocity section for float 4814 which displays a dipole-like distribution of velocities.

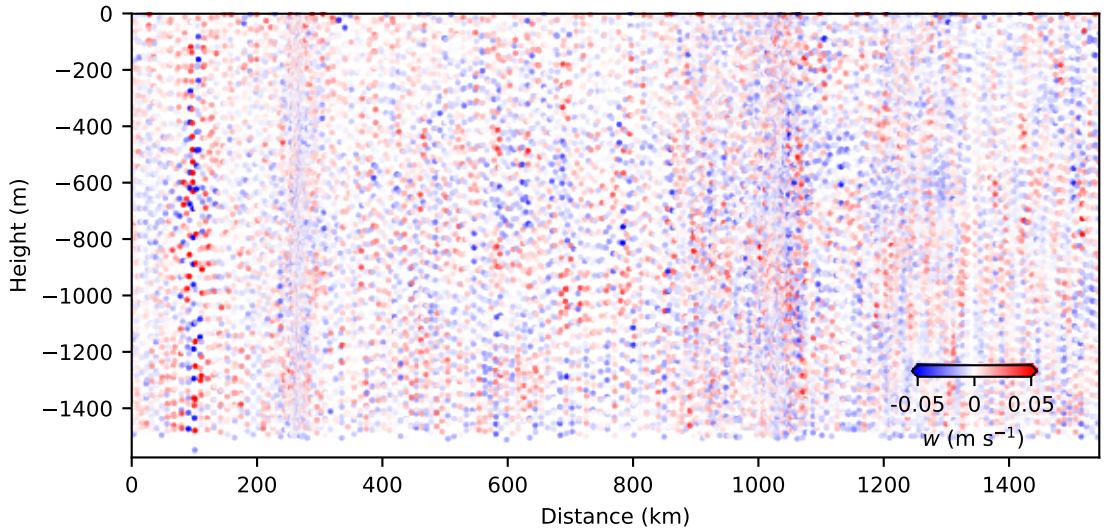

Figure 2.7: Vertical velocity section for float 4976.

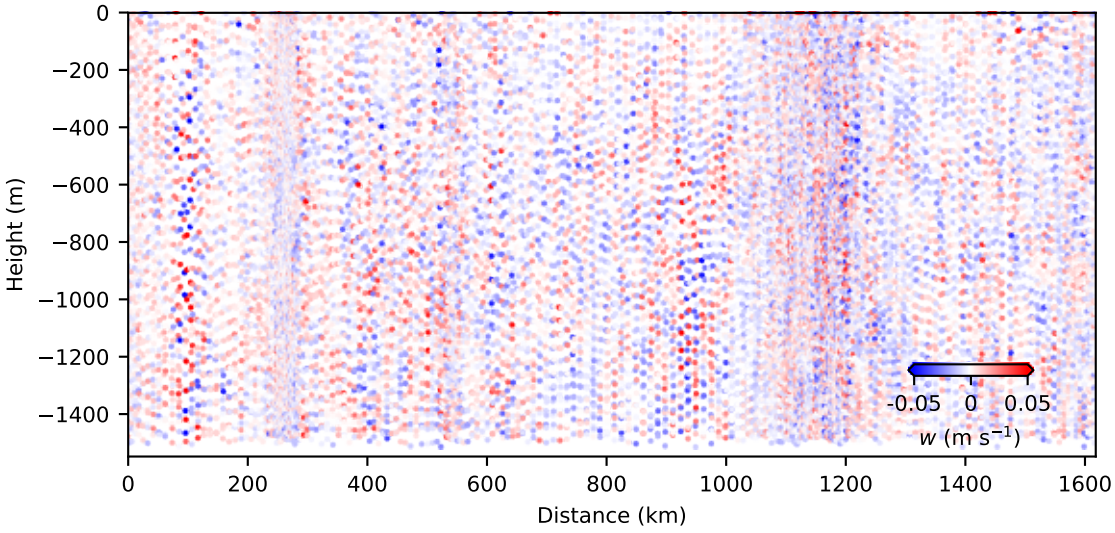

Figure 2.8: Vertical velocity section for float 4977.

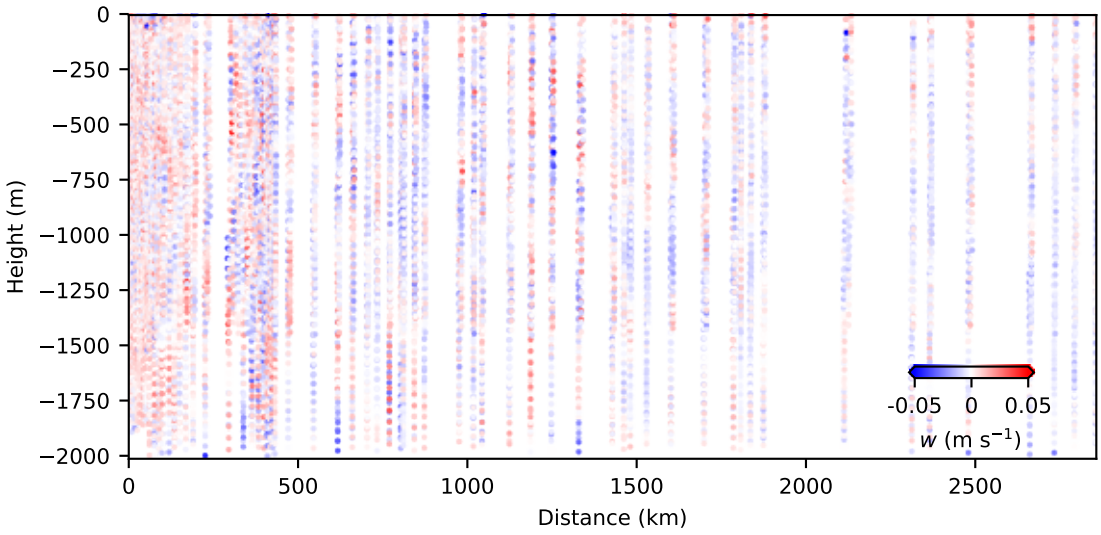

Figure 2.9: Vertical velocity section for float 6478.

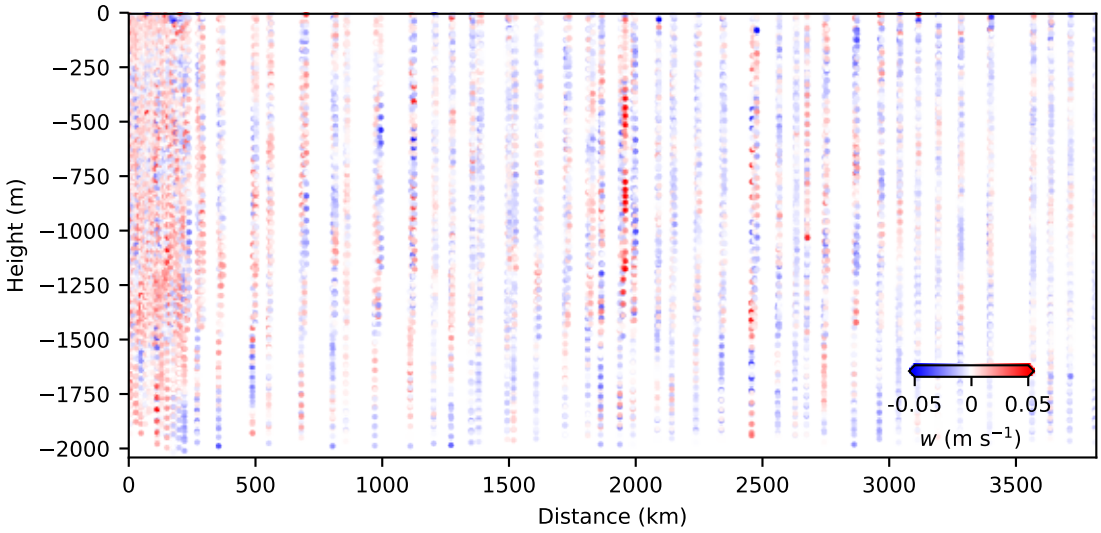

Figure 2.10: Vertical velocity section for float 6480.

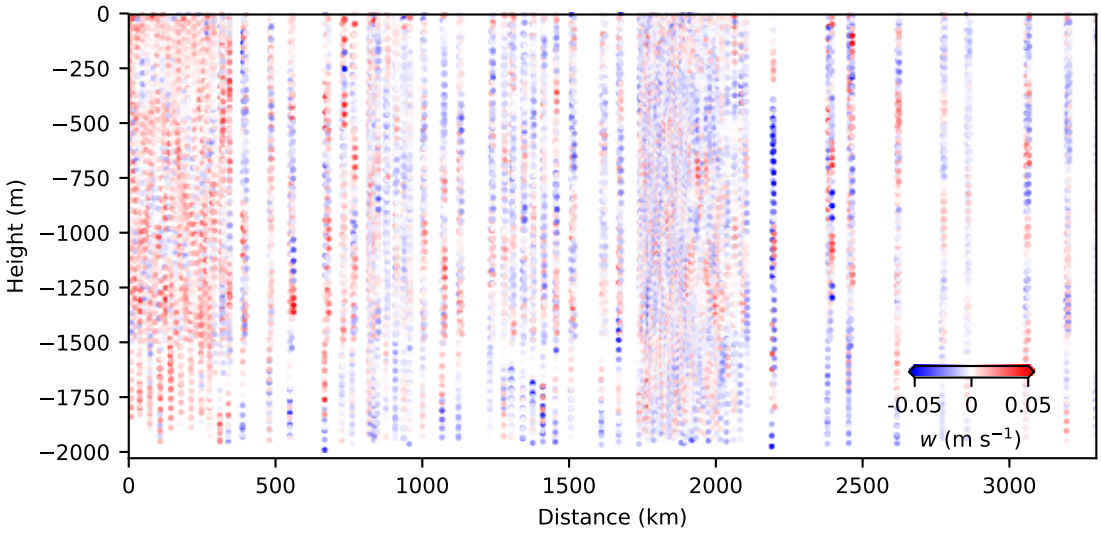

Figure 2.11: Vertical velocity section for float 6625.

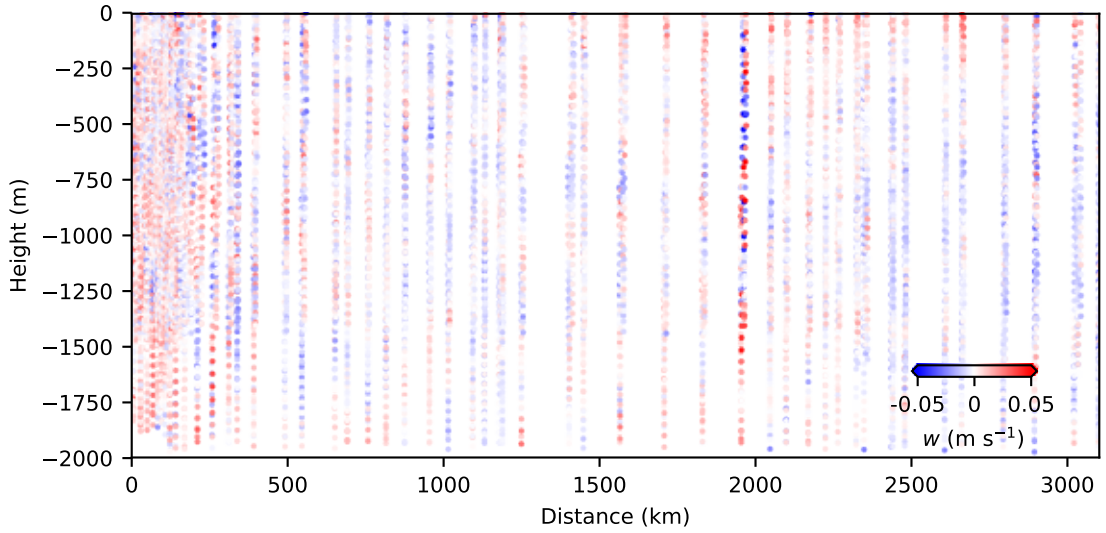

Figure 2.12: Vertical velocity section for float 6626.

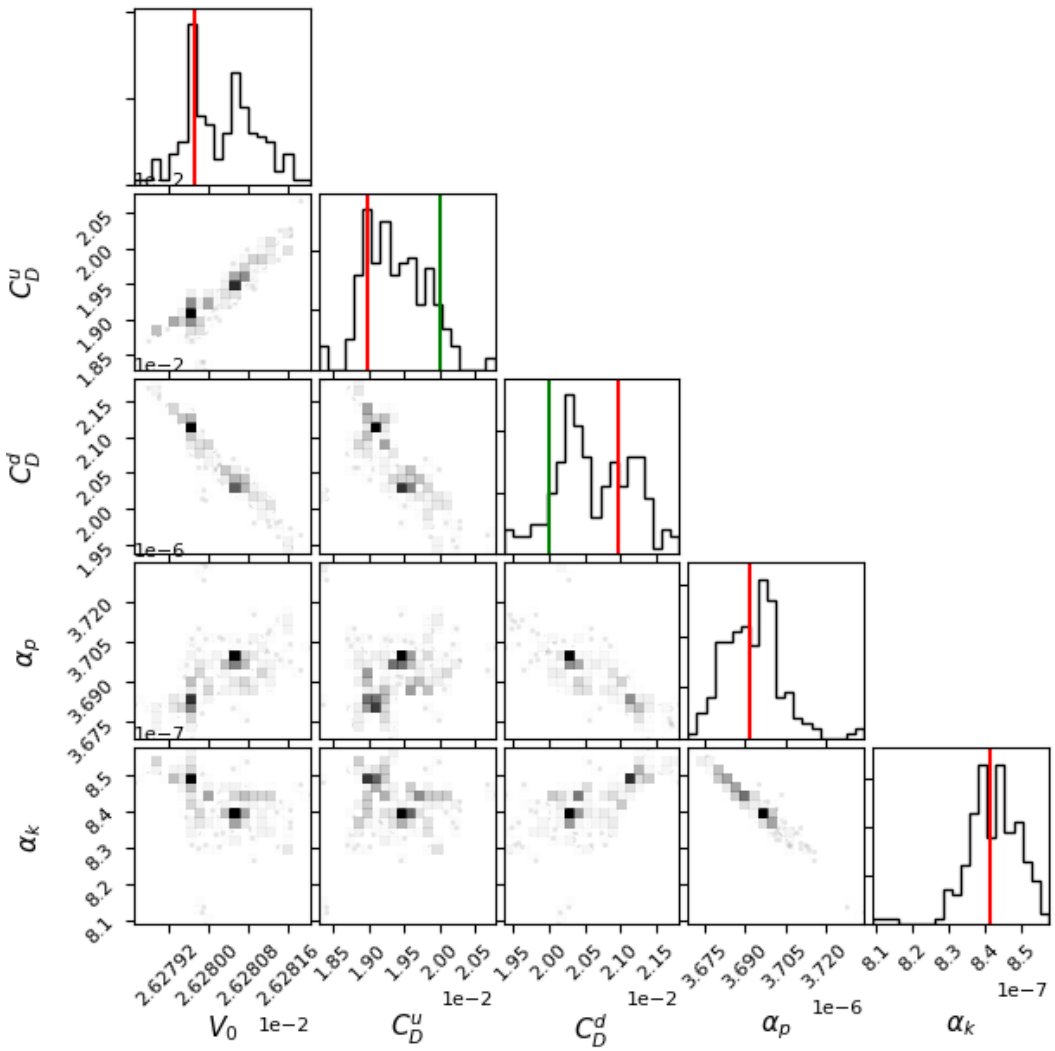

Figure 2.13: Float 6478. The upper most plot in each column is a histogram, displaying the distribution of parameter estimates from a bootstrapping method, with the final parameter estimate denoted by a vertical red line and the expected value by a green line. All other plots are two dimensional histograms for every possible pair of parameters, where the shading is proportional to the density of results. The 2D histograms of highly correlated parameters take on a linear appearance. The variables V_0, C_D^u, C_D^d, α_p and α_k denote volume, upward drag, downward drag, compressibility and piston coefficient respectively.

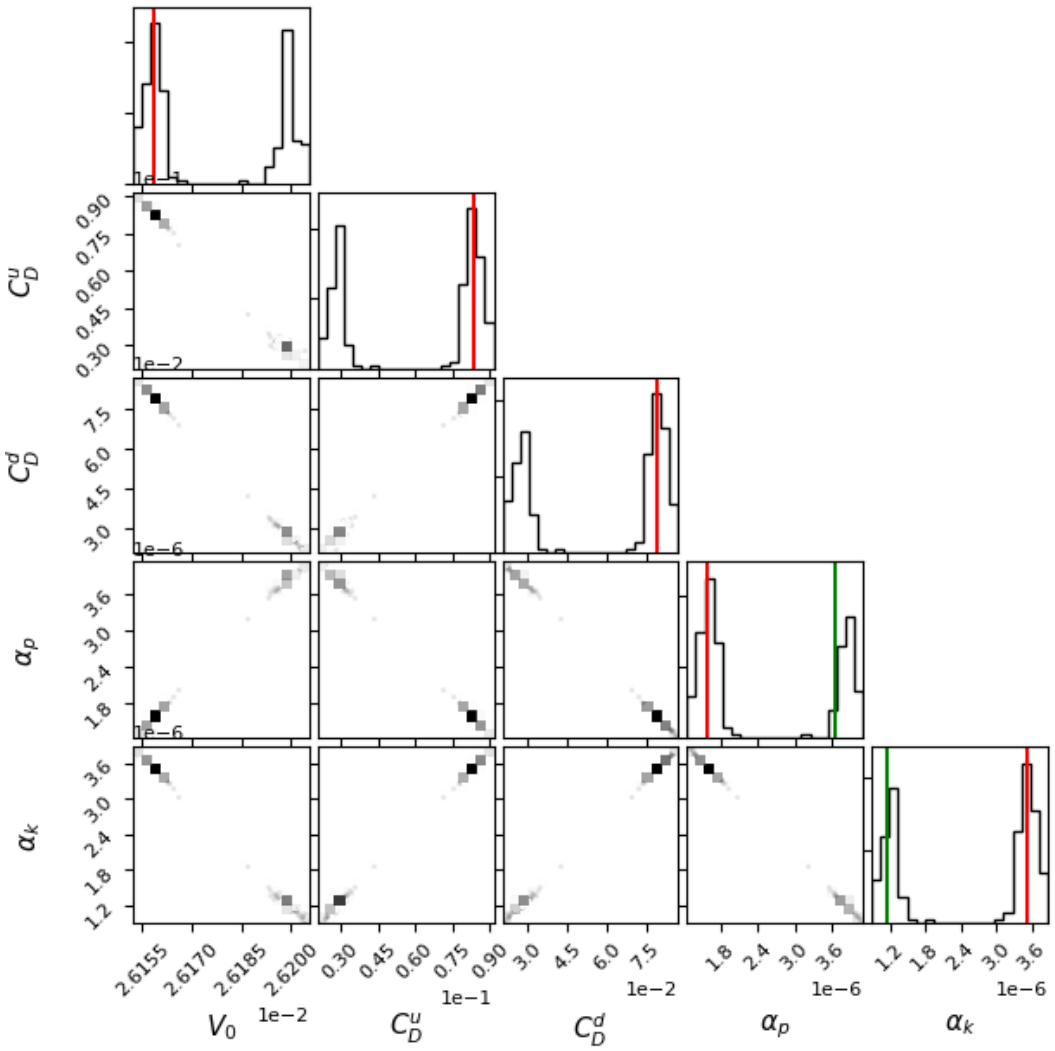

Figure 2.14: Float 4976. See caption of Figure 2.13. Histograms show a bimodal distribution, suggestive of two local minima in the cost function used to optimise the model parameters.

Chapter 3

Observation of a large lee wave

3.1 Introduction

Lee waves can be generally defined as internal gravity waves generated by the interaction of a quasi-steady stratified flow with topography. Observations of such phenomena in the ocean are rare, with notable examples including high frequency, tidally forced waves in the lee of ridges (e.g. Pinkel et al., 2012; Alford et al., 2014). Propagating waves must have a frequency between the local inertial frequency, f, and buoyancy frequency, N, which precludes their generation in many regions of the ocean where bottom flows are not sufficiently strong and topography is not of the correct scale to excite such a frequency. Global maps of energy input to lee waves from geostrophic flows (Scott et al., 2011; Nikurashin and Ferrari, 2011) highlight the importance of the Southern Ocean because it contains many regions that meet the dynamical requirements, usually centred on ridges and fracture zones such as Phoenix Ridge and the Shackleton Fracture Zone in Drake Passage. Lee waves extract energy and horizontal momentum from the forcing flow, and can transport them both vertically and horizontally, redistributing them throughout the water column via nonlinear interactions with other waves, the large-scale flow or instabilities that result in wave breaking (e.g. Munk, 1980). Lee waves have garnered growing interest in recent years, as efforts have been made to understand the origins of small-scale turbulence and its role in returning dense waters to the upper layers of the ocean as part of the global overturning circulation (Talley, 2013; Waterhouse et al., 2014).

Turbulent kinetic energy dissipation and mixing are consistently found to be enhanced over regions of rough bathymetry, using a variety of measurement techniques including tracer releases and microstructure profiles (Ledwell et al., 2000; Watson et al., 2013). The presence of lee waves in these regions is usually inferred from finescale (order 100 m) measurements of variance in velocity shear and isopycnal strain, which show a predominance of upward-travelling wave energy (Naveira Garabato et al., 2004; Kunze et al., 2006; Waterman et al., 2013; Sheen et al., 2013) indicative of bottom generation. In addition, a more limited number of microstructure profiles indicates that turbulent kinetic energy dissipation is enhanced within $\sim$ 1 km of the ocean floor over topography

(St. Laurent et al., 2012; Sheen et al., 2013). Shear and strain based parameterisation methods (e.g. Polzin et al., 2014) are also used to estimate dissipation rates, and while there is currently an unresolved quantitative discrepancy between these results and those from microstructure (Hibiya et al., 2012; Waterman et al., 2014), the qualitative picture of bottom-enhanced dissipation is robust. The inference from this range of observations is that lee waves are generated over rough bathymetry and eventually break, causing turbulence in the vicinity of the topography. However, this picture remains open to alternative interpretations, as the unambiguous observation of lee waves in the Southern Ocean has remained elusive.

It has been appreciated in the atmospheric literature that lee waves, or mountain waves, play an important role in the momentum budget and influence aspects of the general circulation (e.g. Fritts, 2003) and that the results of general circulation models are improved when their effects are accounted for (McFarlane, 1987). The dominant momentum balance in the Antarctic Circumpolar Current (ACC) is between wind stress at the surface and form stress across large bathymetric features, such as ridges, on scales of 1000 km (Vallis, 2006). Further, recent work estimating the lee wave drag on the geostrophic flow from an application of wave radiation theory suggests that regions of the ACC with rough bathymetry of the required lateral scale to excite waves ($1 - 10$ km) may add a non-negligible wave drag to the momentum balance (Naveira Garabato et al., 2013). Direct measurements of lee wave momentum fluxes and convergence in the Southern Ocean are required to test this hypothesis. The results would have implications for numerical models that do not resolve small-scale topography and internal waves, since their effect on the momentum balance would need to be parameterised.

In this chapter, we document the first observations of a lee wave in the Southern Ocean and determine its properties, fluxes of energy and horizontal momentum, and turbulent kinetic energy dissipation levels. The observations were obtained with two Electromagnetic Autonomous Profiling Explorer (EM-APEX) floats deployed in Drake Passage under the auspices of the Diapycnal and Isopycnal Mixing Experiment in the Southern Ocean (DIMES), a U.S. - U.K. program to investigate mixing processes in the ACC (Gille et al., 2007). Previous investigations of internal waves using EM-APEX floats have focussed on diagnosing near-inertial waves, which oscillate with a time period of approximately 14 hours at 57° S, significantly longer than the time it takes to profile (Kilbourne and Girton, 2015; Meyer et al., 2016). Here, we focus on the measurement of a near-buoyancy frequency wave with a period close to 1 hour in a frame of reference moving with the mean flow. This has presented new challenges in analysis because time-dependence cannot be neglected. Several methods for estimating vertical water velocity and turbulent kinetic energy dissipation are adapted and applied to the measurements, allowing almost complete characterisation of the wave in terms of frequency, wavelength, momentum flux, energy flux and dissipation rate.

A description of the floats and data sampling strategy is provided in Section 3.2.1, which

also includes an assessment of a theoretical model of profiling float motion used to calculate absolute vertical water velocity. In Section 3.3, the float measurements are used to characterise the observed lee wave, and estimate its associated fluxes of energy and momentum and turbulent dissipation rates. A discussion of the significance of our findings for the emerging picture of the role of lee waves in the Southern Ocean circulation is offered in Section 3.4, followed by concluding remarks.

3.1.1 Internal wave theory

We summarise here the results of linear internal wave theory that are used in the analysis of observations, following Gill (1982). The linearised, Boussinesq, momentum equations for an incompressible fluid assuming a constant stratification, N, constant Coriolis parameter, f, and constant mean flow $\mathbf{U} = (U, V, 0)$, can be combined into the following equation for vertical velocity perturbations, w',

$$\left[\left(\frac{\partial}{\partial t} + \mathbf{U}\cdot\nabla\right)^2 \nabla^2 + f^2\frac{\partial^2}{\partial z^2} + N^2\left(\frac{\partial^2}{\partial x^2} + \frac{\partial^2}{\partial y^2}\right)\right] w' = 0. \tag{3.1}$$

Plane wave solutions are assumed such that,

$$w' = w_0 e^{i(\mathbf{k}\cdot\mathbf{x} - \omega t)}, \tag{3.2}$$

where w_0 is the velocity amplitude, $\mathbf{k} = (k, l, m)$ is the wavevector, $\mathbf{x} = (x, y, z)$ is the position vector, and ω the Eulerian frequency as would be measured in a frame of reference stationary with respect to the Earth. Substituting this solution into Equation (3.1) gives the familiar internal wave dispersion relation,

$$(\omega - \mathbf{k}\cdot\mathbf{U})^2 = \omega_0^2 = \frac{f^2 m^2 + (k^2 + l^2)N^2}{k^2 + l^2 + m^2}, \tag{3.3}$$

where ω_0 is the intrinsic wave frequency. It can be seen that the intrinsic frequency of a propagating wave measured by an observer travelling with the flow must lie between f and N, else the frequency would be imaginary and the solution evanescent. In the presence of a mean flow, $\mathbf{U}$, a Doppler shifted (Eulerian) frequency, ω, would be measured by a stationary observer and the relationship between the two frequencies is $\omega = \mathbf{k}\cdot\mathbf{U} + \omega_0$.

An internal wave generates fluctuations in all components of velocity, $\mathbf{u}' = (u', v', w')$ as well as pressure, p', and buoyancy, b'. Here we have divided pressure by mean density, $p' = P'/\rho_0$, and define buoyancy as, $b' = -g\rho'/\rho_0$. The relative amplitude of these fluctuations are related to the wave length scales by the polarisation relations,

$$u_0 = \frac{k\omega_0 + ilf}{\omega_0^2 - f^2} p_0 \tag{3.4}$$

$$v_0 = \frac{l\omega_0 - ikf}{\omega_0^2 - f^2} p_0 \tag{3.5}$$

$$w_0 = \frac{-m\omega_0}{N^2 - \omega_0^2} p_0 \tag{3.6}$$

$$b_0 = \frac{imN^2}{N^2 - \omega_0^2} p_0. \tag{3.7}$$

The final plane wave solutions for velocity, buoyancy and pressure are then given by,

$$(u', v', w', b', p') = (u_0, v_0, w_0, b_0, p_0) e^{i(\mathbf{k}\cdot\mathbf{x} - \omega t)}. \tag{3.8}$$

Thus, for a given mean flow speed, stratification and Coriolis parameter, linear waves are completely described by a few key parameters: the components of wavenumber (inverse wavelength) in all three directions, and the amplitude of the pressure perturbation. Frequency is fixed by the ratio of horizontal to vertical wavenumber, or aspect ratio, $\alpha^2 = (k^2 + l^2)/m^2$. The amplitude of velocity fluctuations is set by the pressure perturbation amplitude and wavenumber. Much information can therefore be deduced from limited observations of a few key variables.

By dividing the Equations (3.6) and (3.7), one gets a succinct measure of the wave frequency from the amplitude of buoyancy and vertical velocity perturbations,

$$\left| \frac{w_0}{b_0} \right| N^2 = \omega_0. \tag{3.9}$$

The dispersion relation can be re-cast in terms of the aspect ratio,

$$\omega_0^2 = \frac{f^2 + \alpha^2 N^2}{1 + \alpha^2}, \tag{3.10}$$

which can be rearranged for the aspect ratio,

$$\alpha^2 = \frac{\omega_0^2 - f^2}{N^2 - \omega_0^2}. \tag{3.11}$$

Equations (3.9) and (3.10) provide two methods for deducing internal wave frequency from measurements of velocity and buoyancy amplitude made by EM-APEX floats, both of which are

used in subsequent analysis. For a monochromatic plane wave it can be shown using Equations (3.4), (3.5), (3.6) and (3.11), that the aspect ratio is related to the velocity amplitudes as follows,

$$\frac{w_0^2}{u_0^2 + v_0^2} = \frac{\omega_0^2}{\omega_0^2 - f^2}\alpha^2. \tag{3.12}$$

In the non-hydrostatic limit where $N \geq \omega_0 \gg f$,

$$\frac{w_0^2}{u_0^2 + v_0^2} \approx \alpha^2. \tag{3.13}$$

This result can be substituted into Equation (3.10) to deduce the intrinsic frequency from velocity amplitude alone,

$$\omega_0^2 \approx \frac{(u_0^2 + v_0^2)f^2 + w_0^2 N^2}{w_0^2 + u_0^2 + v_0^2} \approx \frac{w_0^2 N^2}{w_0^2 + u_0^2 + v_0^2}. \tag{3.14}$$

Energy flux

Internal waves have an energy density, E, consisting of a kinetic part relating to the motion of water parcels, and a potential part relating to the displacement of density surfaces from equilibrium,

$$E = \tfrac{1}{2}\rho_0(\overline{u'^2 + v'^2 + w'^2}) + \tfrac{1}{2}\rho_0 N^{-2}\overline{b'^2}. \tag{3.15}$$

Here an over-bar denotes an average over one wave period. Linear internal waves flux energy in the direction of the group velocity, $\mathbf{c_g}$, so that the energy flux vector is given by

$$\mathbf{F_E} = E\mathbf{c_g}, \tag{3.16}$$

which is also defined more generally as the average covariance of pressure and velocity perturbations,

$$\mathbf{F_E} = \rho_0\overline{p'\mathbf{u}'}. \tag{3.17}$$

Often one is interested in the vertical energy flux, $F_E^{(z)}$, which is simply the energy density multiplied by the vertical component of the group velocity,

$$F_E^{(z)} = E c_g^{(z)}, \tag{3.18}$$

or alternatively

$$F_E^{(z)} = \rho_0 \overline{p'w'}. \tag{3.19}$$

The equation for the vertical component of the group velocity can be derived by taking the derivative of the dispersion relation (Equation (3.10)) with respect to vertical wavenumber, $\frac{\partial \omega_0}{\partial m}$, giving the result

$$c_g^{(z)} = \frac{-(N^2 - f^2)\alpha^2}{m(1+\alpha^2)^{\frac{3}{2}}(f^2 + \alpha N^2)^{\frac{1}{2}}}. \tag{3.20}$$

It can be seen that, for fixed α, the vertical group velocity increases with wavelength (inverse wavenumber) and has opposite sign to the wavenumber, such that negative vertical wavenumber indicates upward group velocity and upward energy flux. To estimate vertical energy fluxes from observations requires knowledge of energy density, aspect ratio and wavelength before applying these in Equations (3.18) and (3.20) (e.g. Kunze and Sanford, 1984). Alternatively, it can be estimated from measurements of pressure perturbation and vertical velocity, applying Equation (3.19) (e.g. Nash et al., 2005).

Momentum flux

The absolute vertical flux of horizontal momentum is defined as

$$F_M^{(z)} = \rho_0 \left[(\overline{u'w'})^2 + (\overline{v'w'})^2 \right]^{\frac{1}{2}}, \tag{3.21}$$

where the covariance of velocities are summed in quadrature to account for transport of both zonal and meridional momentum. In the case of linear lee wave generation by infinitesimal topography (e.g. Gill, 1982), the vertical flux of horizontal momentum is equal in magnitude to the drag force exerted on the mean flow. If finite-amplitude effects are taken into account, including flow blocking and splitting, the drag becomes a nonlinear function of the steepness parameter (Welch et al., 2001).

3.2 Method

3.2.1 Instrumentation and sampling strategy

The primary observations of this work were obtained by two EM-APEX floats, numbered 4976 and 4977, deployed at the same time and position in the Drake Passage from the *RSS James Cook* (68° 11′ 1.4″ W. 57° 34′ 14.9″ S) on 31 December 2010 at 12:18 UTC. Float trajectories are displayed in Figure 3.1.

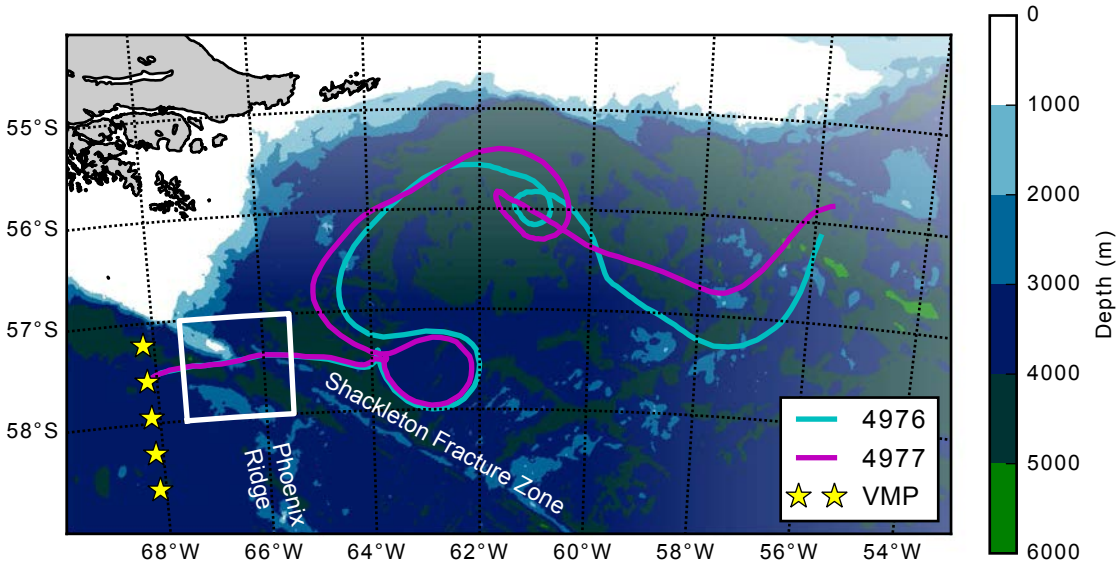

Figure 3.1: Map of the northern Scotia Sea with float trajectories and vertical microstructure profiler stations used in calibrating the float-derived dissipation rates. Lee wave measurements were obtained within the boxed region, which is expanded in Figure 3.5.

The sampling frequency varied but on average CTD measurements were made every 20 s or 2.5 m, while EM measurements were made every 25 s or 3 m. Both floats analysed here were programmed to profile continuously to 1500 dbar, taking about 3.5 hours to complete an ascent or descent, pausing only while at the surface for an average of 30 minutes to transmit data.

3.2.2 Derived variables

Analysis was performed on several variables not directly observed by the floats, and their derivation is described here briefly. Relative horizontal velocity measurements were converted to absolute horizontal velocity using the method described by Phillips and Bindoff (2014). In summary, the relative horizontal velocity measured from a descent / ascent profile pair is integrated with respect to time, providing a displacement estimate. The difference between this displacement and the measured GPS displacement at the surface is then divided by the time taken to profile and constitutes a constant depth-independent velocity that is added back to the relative velocity. This method also provides an estimate for subsurface float position (x, y), in metres, in the zonal and meridional direction from the point of descent.

In situ and potential density as well as buoyancy frequency were calculated from CTD temperature, salinity and pressure measurements using the 2010 equation of state for seawater (IOC et al., 2010). Smooth reference potential density profiles referenced to 1000 dbar, ρ_{ref}, were computed by averaging 5 profiles before and after the target profile. Density perturbations, ρ', were calculated by subtracting reference density from measured density, $\rho' = \rho - \rho_{\text{ref}}$. Smooth 'reference' buoyancy frequency profiles were generated using the adiabatic levelling method (Bray and Fofonoff, 1981; Millard et al., 1990) with a vertical window size of 400 dbar. Pressure perturbation was estimated by integrating buoyancy perturbation, $b' = -g\rho'/\rho_0$, with depth assuming hydrostatic balance before subtracting the depth average, using a method described by Kunze et al. (2002) and further analysed by Nash et al. (2005).

3.2.3 Estimation of internal wave properties

Internal wave properties are estimated by application of linear internal wave theory to the measurements. Properties that can be deduced without knowledge of the wavenumber components are aspect ratio, α, intrinsic frequency, ω_0, energy density, E, and the vertical fluxes and of energy and horizontal momentum, denoted $\overline{w'p'}$ and $(\overline{w'u'},\overline{w'v'})$ respectively. The mean flow is well described by a uniform flow plus a linear shear, evidence of which is provided in Section 3.3.1 and so to estimate the wave perturbation of horizontal velocity, (u', v'), a linear background shear is removed from absolute horizontal velocity measurements.

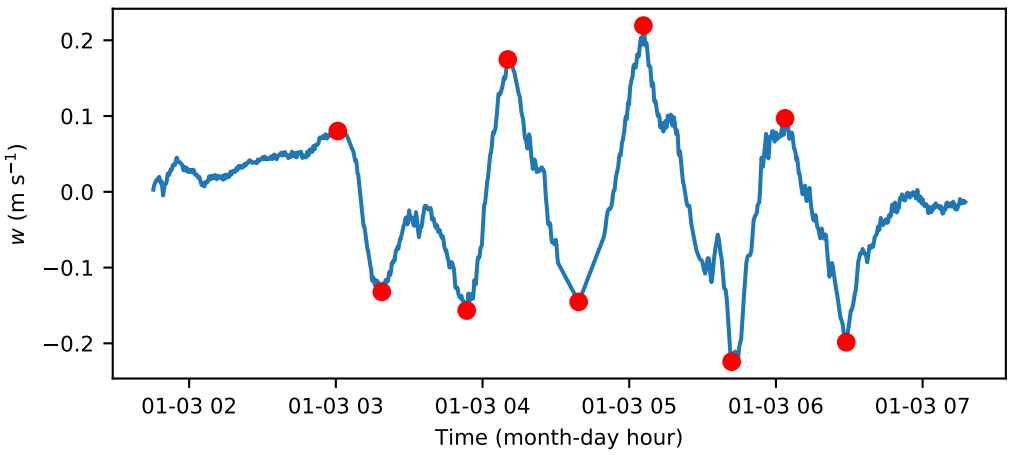

Figure 3.2: A time series of vertical velocity from float 4976. Maxima and minima found using a peak detecting algorithm are shown with red circles.

To estimate the aspect ratio and intrinsic frequency, fourteen sets of coherent velocity and buoyancy maxima/minima were identified from profiles using a peak detection algorithm, and confirmed by eye. Figure 3.2 shows an example of the algorithm applied to vertical velocity from float 4976 using a threshold peak height of 0.05 m s^{-1} and minimum distance between peaks of 100 data points equivalent to 37 minutes in time. The amplitudes at the maxima/minima were then applied in Equations (3.10) and (3.13). By isolating maxima in this way we assume that the variability is dominated by a single monochromatic wave. Energy density was calculated by

isolating segments of velocity and buoyancy profiles that contained an integer number of wave oscillations, identified from subsequent maxima by eye, before computing the time average over those isolated sections following Equation (3.15). The sections used are those depicted in Figure 3.6. The vertical fluxes of energy and horizontal momentum were also estimated for the isolated segments following the same approach. The above quantities, deduced without attempting to estimate any wavenumber components, are referred to as the 'observed' quantities.

The impact of background oceanographic variability (which is significantly larger in magnitude than instrumental noise) on the energy and momentum flux diagnostics was investigated by repeating the calculation with the addition of red noise with spectral properties, such as slope and energy level, given by a background spectrum. The background spectrum was computed by averaging the absolute velocity spectra from 100 profiles 100 km downstream and 2 days after the large wave event. The standard deviation of results after many repetition is the error, quoted in subsequent analysis. Ultimately, the results are found to be insensitive to choices of the type and energy level of background variability used.

To deduce the wavenumber, we fit monochromatic plane waves to observations of velocity, buoyancy and pressure perturbation. Once deduced, the wavenumber implies, following linear theory, values for all the quantities discussed above. The quantities deduced from this fitting are referred to as 'plane wave' estimates. Two illustrative profiles are presented in Section 3.3.2. The fits take into account the combination of spatial and temporal variability present in the observations by using the depth measurement from the float's pressure sensor, the horizontal position estimated from time-integrated horizontal velocity, and time from the internal clock. In this way, it was possible to account for advection of the float by the local flow field.

The fitting procedure optimises five parameters: the three wavenumber components, the pressure perturbation amplitude induced by the wave, and an arbitrary phase shift. Doppler shifting was accounted for by using the mean horizontal velocity of each profile, and a background shear was subtracted from the horizontal velocity. Markov Chain Monte Carlo methods were used to conduct the fitting and produce likelihood distributions for the parameter values. Likelihood distributions are proportional to the posterior probability distribution, which describes the probability that the model fits the data with given parameter values. The most likely parameter set is the best estimate of the parameter value and the width of the distribution is a measure of the confidence interval of that parameter set.

3.2.4 Estimation of the turbulent kinetic energy dissipation rate

To estimate the rate of turbulent kinetic energy dissipation rate, ϵ, we employ the large eddy method of Beaird et al. (2012), which has previously been applied to vertical velocity measurements from gliders. We also use the more established Thorpe scale method (Thorpe, 1977; Dillon,

1982) for comparison. The results derived from these methods are a 'best effort' at estimating turbulent parameters from measurements that do not resolve the inertial subrange.

Large eddy method

The large eddy method can be derived from simple scaling of turbulent motions, specifically, the turbulent kinetic energy relation (Taylor, 1935),

$$\epsilon \sim \frac{q'^3}{l} \tag{3.22}$$

where q' is the turbulent velocity scale and l a length scale associated with the largest overturning eddies. The choice of an appropriate length scale is subject to certain arbitrariness (Kantha and Clayson, 2000). However, if one chooses the buoyancy length, defined as the vertical displacement over which a water parcel will convert its kinetic energy to potential energy in a stratified fluid and given non-rigorously as $q'N^{-1}$, then one arrives at the following equation,

$$\epsilon = c\langle q'^2 \rangle N \tag{3.23}$$

where c is a constant of proportionality. A complementary interpretation is that turbulent eddies are dissipated over a time proportional to N^{-1}, known as the eddy turnover time. An assumption of the method is that the largest turbulent scales are isotropic, and that it is sufficient to measure the kinetic energy of one (in this case, the vertical) velocity component, equal to the mean square velocity $\langle q'^2 \rangle$, to estimate the energy of an overturn. Tests of the scaling (Beaird et al., 2012, and references therein) indicate that it is valid for a range of oceanic conditions, including weak dissipation regimes, down to $q' \sim 0.2$ mm s^{-1} (Peters et al., 1995).

The constant of proportionality also corrects implicitly for limitations of the float vertical velocity model, and for measurements that may not fully isolate turbulent motions and include small-scale internal waves. The vertical microstructure profile measurements made shortly before deployment of the floats (Sheen et al., 2013), marked as stars in Figure 3.1, provide the best available calibration data. The statistics of ϵ from the large eddy method and microstructure match for $c = 0.146$ (float 4976) and $c = 0.123$ (float 4977).

To isolate the vertical eddy velocity signal, first a temporal low-pass filter was applied to vertical velocity profiles with a cut-off period of 100 s. This was necessary to remove signals associated with internal electronic noise with an approximate length scale of 9 m resulting from a suspected time-stamp recording error, exhibited by both floats. The narrow bandwidth of the noise allowed for its complete removal. A spatial high-pass filter was then applied with a cut-off wavelength of 40 m. Steady height, $z_s = \int w_s dt$, rather than measured height, z, was used

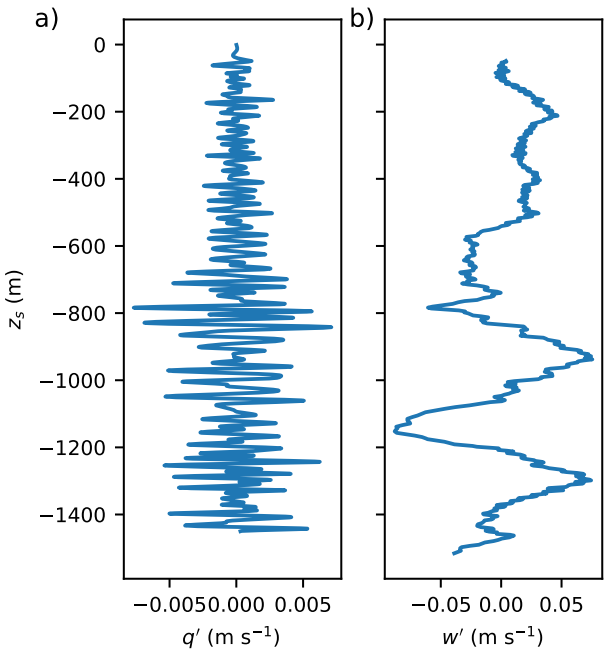

Figure 3.3: Examples of a) band-pass filtered vertical velocity, q', and b) absolute vertical velocity, w', from Float 4976 profile 34.

as the spatial variable so as to reduced aliasing caused by changes in float profiling speed and advection by vertical flows. An example of the band-pass filtering applied to a vertical velocity profile is shown in Figure 3.3. Root-mean-square vertical velocity and mean buoyancy frequency were calculated in a sliding 20 m window. Comparison of vertical kinetic energy spectra between profiles with high and low average ϵ values (not shown) indicate that energy is most enhanced at scales less than 100 m. The filter cut-off length scale is chosen pragmatically to capture this variance.

D'Asaro and Lien (2000b) note that in a stratified environment it is difficult to differentiate between turbulence and internal waves. They consider the applicability of Equation (3.23) as a function of large scale Richardson number and distinguish between two regimes; the stratified turbulence regime, where the Richardson number is small and the internal wave regime when the number is large. Equation (3.23) applies in the stratified turbulence regime, when the internal wave field bandwidth, defined as m_1/m_c approaches 1, where m_1 is the largest vertical wavenumber in the deep ocean and m_c the critical wavenumber, usually taken as 0.1 cpm in the Garret-Munk model. The observations presented here are not in the stratified turbulent regime and this might be expected to cause an overestimation of the dissipation rate, however, since the method is calibrated against microstructure measurements, the coefficient c, is proportionally smaller to account for wave energy. The fact that the method theoretically relies on measuring the eddy energy, rather than the wave energy remains a cause of concern. Some reassurance can be taken from the documented, albeit poorly understood relationship between wave vertical kinetic energy and dissipation found by Thurnherr et al. (2015) in a variety of regions, including the Drake Passage. Thurnherr et al. (2015) use their findings as the basis for a new parametrisation of

dissipation in terms of VKE alone, which appears to provide more accurate results than shear-strain based parametrisations. This is relevant because it implies that internal wave VKE is strongly connected to dissipation. We accept that some readers may not be convinced by the large eddy method and so we also estimate dissipation using the more established Thorpe scale method.

Thorpe scale method

The theoretical basis of the Thorpe scale method is that, in a stratified fluid with buoyancy frequency N, the dissipation rate is related to the largest isotropic turbulent scales, defined by the Ozmidov scale L_O,

$$\epsilon = L_O^2 N^3. \tag{3.24}$$

At scales larger than the Ozmidov scale, stratification suppresses vertical motion and turbulent eddies become anisotropic. At smaller scales, there exists an inertial subrange where energy cascades to the dissipation scale. By comparing a profile of density with the same data monotonically sorted, such that it forms a stable profile, it is possible to estimate the vertical displacement of density parcels in overturning regions. The Thorpe scale, L_T, is defined as the root mean square displacement of data in an overturn and empirically related to the Ozmidov scale by the relation $L_0 = (0.8 \pm 0.4)L_T$ (Dillon, 1982). The standard error on a density measurement from a float is 0.0016 kg m^{-3}, caused by random error in the temperature and salinity measurements of 0.002 °C and 0.002 respectively. The smallest resolvable Thorpe scale is 1.6 m, corresponding to a dissipation rate of 1.6×10^{-8} W kg^{-1}.

The method is sensitive to spurious density measurements, especially in weakly stratified regions of the water column, which may occur due to salinity spiking. To counter this problem we use the intermediate profile method of Ferron et al. (1998) and reject overturns using an overturn ratio criteria (Gargett and Garner, 2008). The intermediate profile method creates a smooth density profile that removes fluctuations smaller than the accuracy of the sensor. The overturn ratio compares the relative vertical length scale of the positive and negative density perturbations in each individual overturn. If the ratio is small then the overturn is suspect and could have been caused by salinity spiking. We set the threshold ratio to 0.3.

3.3 Results

3.3.1 Observed wave properties

Large-scale observations

Between the 2nd and 4th of January 2011, two EM-APEX floats were advected eastwards over the northern segment of the Shackleton Fracture Zone (SFZ), a chain of sea mounts and large bathymetric features that extends between the Antarctic Peninsula and the South American continental shelf. They maintained a horizontal separation of approximately 4 km during this period. The boxed area in Figure 3.1 marks this region, and all subsequent analysis is concentrated within it. The upper-ocean buoyancy frequency and velocity upstream of the SFZ are shown in Figure 3.4 as an average of 20 profiles. The mean zonal flow speed between 100 m and 1500 m was 33 cm s^{-1}, with a vertical shear of 1.35×10^{-4} s^{-1}. The mean meridional flow over the same depth range was 2 cm s^{-1}, with some variability between profiles and no significant shear. There also exists a minimum in buoyancy frequency at 350 m depth, which may reflect upward propagating internal waves with a frequency greater than 1.4×10^{-3} rad s^{-1}.

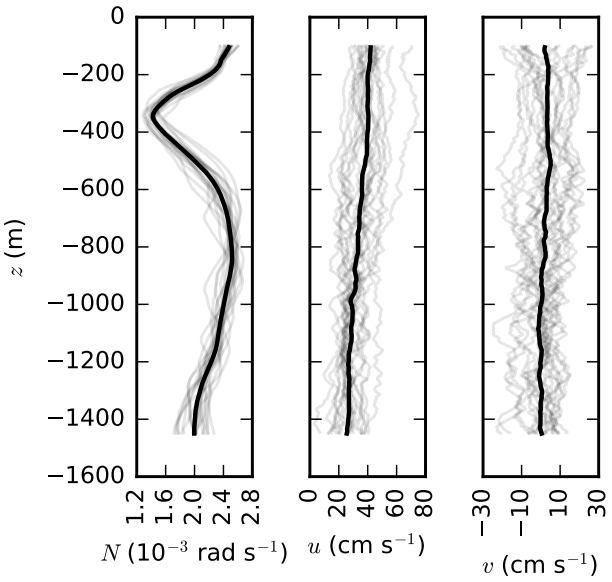

Figure 3.4: Profiles (light grey) of buoyancy frequency, zonal velocity and meridional velocity taken prior to the large vertical velocity perturbations. Mean profiles are shown in black.

Figure 3.5a displays the measured depth-averaged horizontal flow vectors around the SFZ, as well as the standard deviation of vertical water velocity measured below 100 m depth, shown by the vector shading. In the lee of a large topographic ridge, oscillatory vertical velocity perturbations with an amplitude exceeding 20 cm s^{-1} were measured by both floats, resulting in large values of vertical velocity standard deviation. Away from this region, vertical velocity measurements were typically less than 2 cm s^{-1}. Figure 3.5b displays a section of vertical velocity as a function of height and distance from the ridge crest. The largest vertical velocities were measured within 20 km of the crest. The sawtooth-like trajectory is typical of a profiling float being advected

by a strong mean flow. All the topographic data used originate from version 17.1 of the Smith and Sandwell (1997) global bathymetric database, since high-resolution multibeam bathymetric measurements were not available.

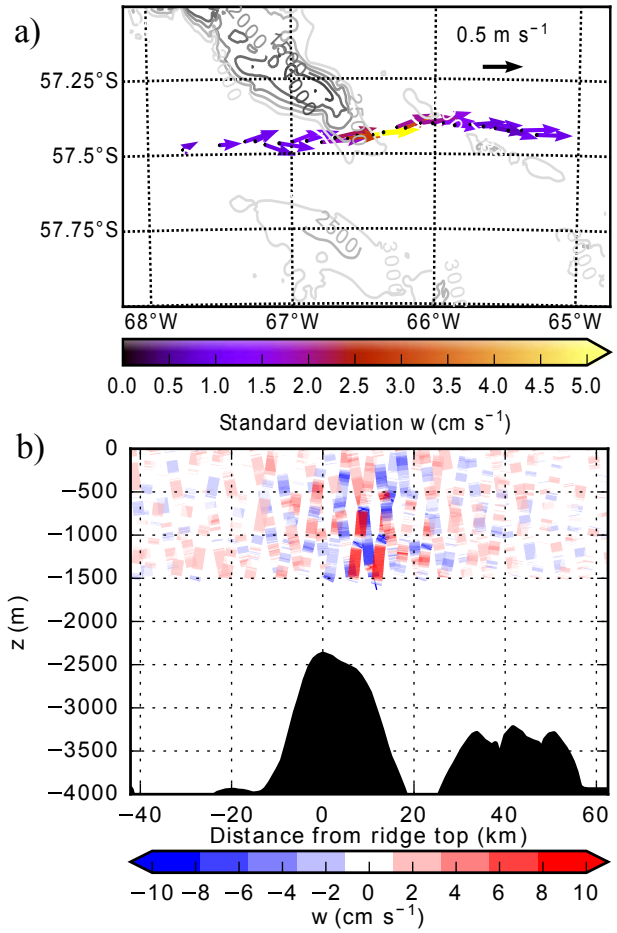

Figure 3.5: a) Mean horizontal velocity vector below 100 m within the boxed region in Figure 3.1. Arrow colour denotes the standard deviation of vertical velocity measured below 100 m depth. Depth is contoured in 500 m increments. b) A vertical section of vertical velocity from the same region. The observations from both floats are superposed, and topography from Smith and Sandwell (1997) database is shaded.

Figure 3.6 shows velocity and buoyancy perturbations from a sequence of profiles centred on the largest vertical velocity signal. Vertical velocity from these profiles were binned and displayed as a histogram in Figure 2.3, from which it can be seen that the distribution of velocity differs greatly from the far field mean. The greatest vertical displacement of density surfaces, estimated as b_0/N^2, was observed to be (120 ± 20) m (profile 32 float 4976). The shaded segments indicate measurements where vertical velocity amplitude exceeds 10 cm s^{-1} and also varies coherently with at least one other component of velocity. Profiles 31 and 32 from float 4976, and profiles 26 and 27 from float 4977, contain such segments. These four profiles are used in the following analysis to quantify the wave properties. While Figure 3.6 shows several other profiles that contain less conspicuous wave-like signals, noise in the horizontal velocity and buoyancy components makes it difficult to confidently assess wave properties from those profiles.

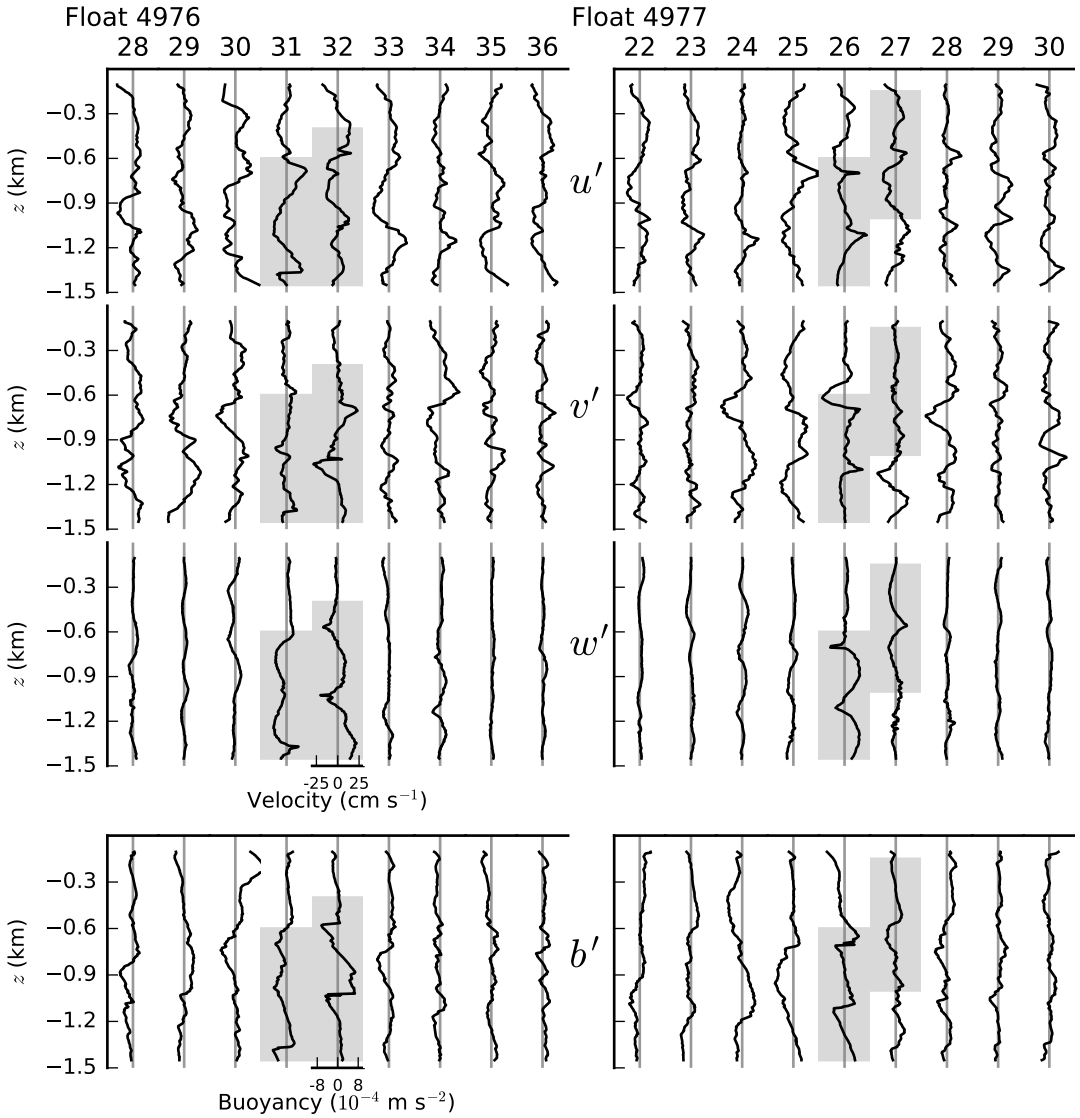

Figure 3.6: An observed series of profiles for the two floats, split into rows of zonal (u'), meridional (v') and vertical velocity (w'), and buoyancy (b'). The observations are centred around the ridge crest, and approximately correspond to the section of Figure 3.5b between 0 km and 20 km downstream of the ridge. Each minor column represents the results from a single profile, and is numbered by its profile ID. The two major columns separate results for the two floats. The shaded regions mark segments of profiles that contain a coherent wave signal in multiple velocity components, as well as a vertical velocity amplitude in excess of 10 cm s^{-1}.

Frequency and aspect ratio

The fourteen sets of maxima and minima from four profiles (those shaded in Figure 3.6) are listed in Table 3.1 and used to estimate wave aspect ratio and frequency. Figure 3.7a amalgamates the data in the table into box and whisker diagrams, showing median, 25th and 75th percentiles and range. The mean aspect ratio is 1.0 ± 0.6. Using Equation (3.9), the mean frequency is $(1.8 \pm 1) \times 10^{-3}$ rad s^{-1}, and using Equation (3.10) it is $(1.4 \pm 0.4) \times 10^{-3}$ rad s^{-1}. Both values are close to the local mean buoyancy frequency $N \approx 2.2 \times 10^{-3}$ rad s^{-1} and one order of magnitude larger than the local inertial frequency $f \approx 1.2 \times 10^{-4}$ rad s^{-1}. The period associated with the estimated frequency is approximately 1 hour. The spread of results is a consequence of the

Table 3.1: Values of velocity and buoyancy and 14 identified maxima and minima along with the corresponding aspect ratio and frequencies. The frequency denoted ω_0 is calculated from Equation (3.14) while ω_0^* is calculated from Equation (3.9). The velocity values have units of (m s^{-1}), the buoyancy has units of (10^{-4} m s^{-2}), the aspect ratio has no units and the frequencies have units of (10^{-3} rad s^{-1}).

Float	Profile	u_0	v_0	w_0	b_0	α	ω_0	ω_0^*
4976	31	0.17	0.11	0.17	4.0	0.84	1.41	2.06
		-0.12	-0.08	-0.025	-4.0	0.17	0.38	0.30
		0.20	0.045	0.07	-3.6	0.34	0.71	0.94
	32	0.10	0.18	0.19	2.0	0.92	1.49	4.60
		-0.06	-0.20	-0.20	-5.0	0.96	1.52	1.94
		-0.05	0.22	0.10	5.0	0.44	0.89	0.97
		-0.17	0.00	-0.20	-6.0	1.18	1.68	1.61
4977	26	-0.095	-0.075	0.16	4.5	1.32	1.76	1.72
		0.20	0.16	-0.10	-4.0	0.39	0.80	1.21
		-0.10	-0.04	0.17	3.0	1.58	1.86	2.74
		0.11	0.17	-0.21	-6.0	1.04	1.58	1.69
	27	-0.13	0.00	-0.080	-3.0	0.62	1.15	1.29
		0.10	0.00	0.12	2.7	1.20	1.69	2.15
		-0.030	0.00	-0.070	2.3	2.33	2.02	1.47

limited profiling speed, which is likely capturing the gradually changing characteristics of a wave propagating through a vertical shear and non-uniform stratification.

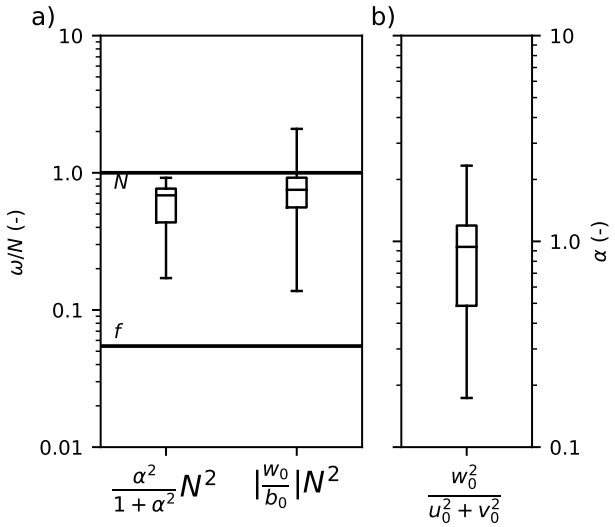

Figure 3.7: a) Two estimates of frequency normalised by the local buoyancy frequency, displayed as box and whisker plots. The estimates were obtained using Equations (3.9) and (3.10), which label the x–axis. The inner line of each box denotes the median frequency. The two horizontal lines indicate the buoyancy frequency, N, and inertial frequency, f. b) A box and whisker plot of the aspect ratio $\alpha = \frac{k_h}{m}$, estimated from the velocity amplitudes.

Energy and momentum fluxes

The shaded regions in Figure 3.6 indicate the isolated sections for which energy density and vertical fluxes of energy and horizontal momentum were calculated. The peak energy density was found to be 26 ± 4 J m^{-3} in profile 32 float 4976. Results from the four main profiles are displayed

in Figure 3.8a as box and whisker plots, and range in magnitude from 10 to 26 J m^{-3}.

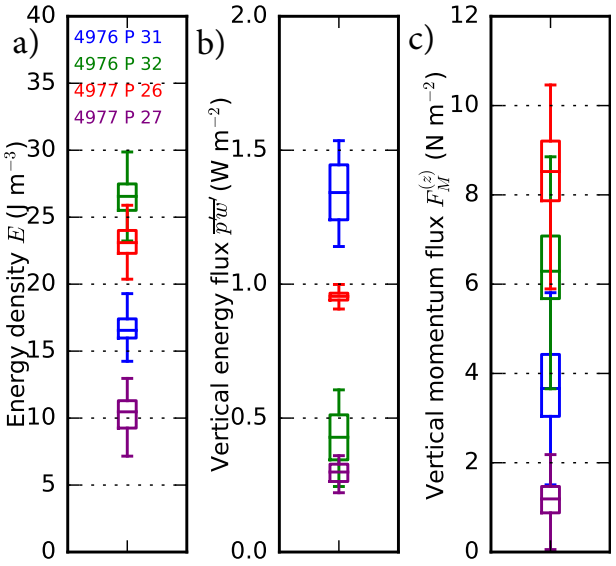

Figure 3.8: Estimates of a) energy density, E; b) vertical energy flux, $\overline{w'p'}$; and c) vertical flux of horizontal momentum, $F_M^{(z)}$. The error bars are displayed as box and whisker plots derived from a bootstrapping technique, the inner box contains 50% of estimates, the central line denotes the median and outer whiskers encompass the full range of estimates.

Observational estimates for the time-mean quantities $\overline{w'p'}$ and $F_M^{(z)}$, respectively representing the vertical fluxes of energy and horizontal momentum are displayed in Figures 3.8b and c. The peak energy flux was 1.3±0.2 W m^{-2}. All fluxes are positive, indicating upward wave propagation. The smallest value was found for profile 27 from float 4977, where the wave signal occurs higher in the water column, consistent with the group velocity diminishing as the depth of minimum N is approached. The average vertical group velocity corresponding to the observed flux and energy density is, following Equation (3.18), found to be 4 ± 1 cm s^{-1}. These energy flux diagnostics are likely to be underestimates, due to limitations in the method for estimating p'. For a wave with $\alpha \sim 1$, the hydrostatic approximation on which estimation of p' relies (Nash et al., 2005) holds only weakly. However, tests performed on a series of synthetic waves with α in the range 0.5 to 1.5 indicate that the method is typically in error by less than a factor of two. So while the uncertainty on the measured energy flux is substantial, the order of magnitude is correct and the real peak value is likely to be closer to 2 W m^{-2}.

Estimates of the vertical flux of horizontal momentum range from 1 to 8 N m^{-2} in magnitude. The uncertainty on individual measurements is larger than in the energy flux case because the quantity is more sensitive to oceanographic variability in the horizontal velocity. Momentum flux vectors are displayed in Figure 3.9, and are oriented predominantly in the northwest - southwest quadrant. The scatter in vector direction is likely indicative of the three-dimensional nature of the wave generation process, occurring off a complex topographic feature that does not lie perpendicular to the mean flow, but could also be spatial variability. In the classic textbook lee wave problem, the momentum flux vector would be orientated in direct opposition to the

mean flow. The mean zonal momentum flux was -3.1 ± 0.4 N m^{-2}, and the mean meridional momentum flux was 0.5 ± 0.4 N m^{-2}. In comparison, mean flow velocity vectors are orientated eastward (Figure 3.5a) in the opposite direction to the mean momentum flux. The limitations of the floats' spatio-temporal sampling of the wave mean that we cannot definitively establish whether the wave is imparting a drag on the mean flow, or radiating horizontal momentum elsewhere.

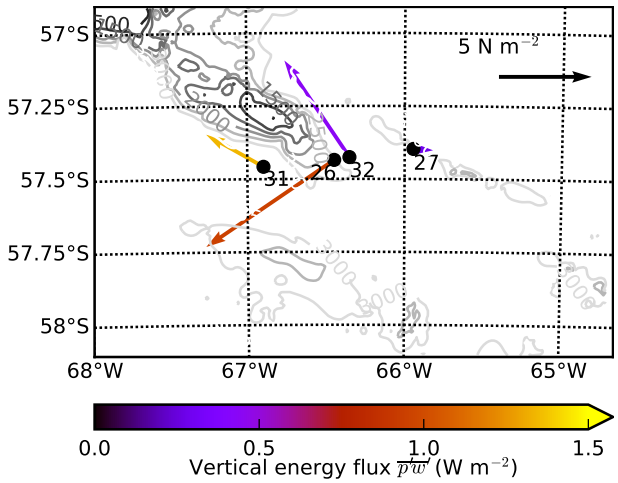

Figure 3.9: Vertical flux of horizontal momentum vectors, $\rho_0(\overline{w'u'}, \overline{w'v'})$, labelled by profile number. Arrow colour denotes the vertical energy flux. Depth is contoured in 500 m increments.

3.3.2 Wave characterisation with plane wave fits

EM-APEX floats profile slowly compared to the observed wave period of 1 hour, and this will have caused temporal aliasing of the measurements. The apparent vertical wavelength observed from subsequent maxima in vertical velocity from Figure 3.6 is approximately 400 m. If the wave is stationary, its horizontal wavelength can be deduced from the Doppler relation (Equation (3.3)), as $\omega_0 = -kU$. For the observed frequency and mean flow speed, this results in an approximate zonal wavelength of 1200 m, which will be the same as the vertical wavelength for $\alpha = 1$. The conclusion from this estimate is that the intrinsic wavelength could be significantly larger than the apparent wavelength.

Fits of Equation (3.8) to measurements from two profiles chosen for having the cleanest wave signal (profile 32 from float 4976 and profile 26 from float 4977) were conducted to compare the observations to the simplest possible theoretical explanation, a monochromatic plane wave. Doing so also provides a separate determination of the vertical fluxes of energy and momentum. The resulting parameter estimates (wavenumbers and pressure perturbation) from this fitting procedure were inserted into the linear internal wave equations (Equation (3.8)) to produce the red curves in Figure 3.10. The fit to profile 26 shows good agreement with observations for all variables, with the exception of u, which is not of the correct amplitude. Profile 32 contains small scale fluctuations in velocity which are not explained by a monochromatic plane wave, however,

the large scale variation is captured. The quantities are plotted as a function of time, rather than height, to remove the temporal-aliasing that causes cusping, visible in Figure 3.6. Cusping occurs as alternating phases of wave motion force the floats against their direction of motion, in some cases causing a complete reversal of direction, and then propel them in the same direction of motion, greatly increasing the profiling speed. Such forcing aliases the observations away from an expected sinusoidal shape.

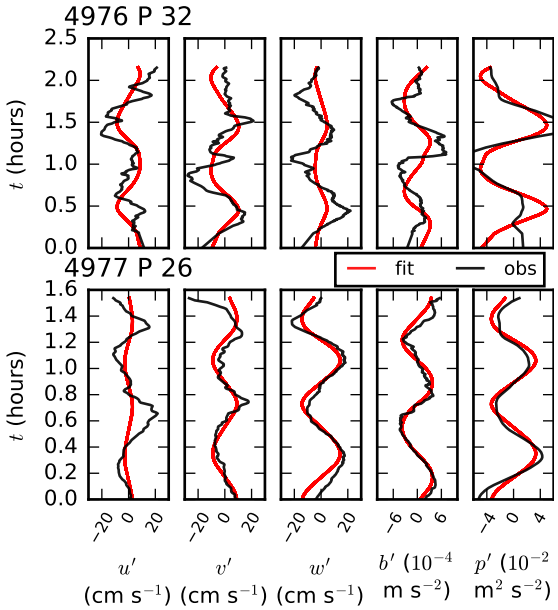

Figure 3.10: Comparison of linear internal wave fits and observations for two float profiles, both of which were ascents. The quantities u', v', w', b' and p' are plotted as a function of time since start of profile.

Figure 3.11a shows the likelihood distributions of the plane wave derived wavenumber components as box and whisker plots. It should be noted that the range of the distributions is typically less than 1% of the parameter value and so uncertainties are not quoted. For both profiles the fitting method finds the optimal zonal wavenumber, k, to be -0.002 rad m^{-1}, which corresponds to a zonal wavelength of 4000 m. This is likely to be an underestimate of the real wavenumber, because the fits do not reproduce the observed zonal velocity amplitude which is related to the wavenumber by the polarisation relation in Equation (3.4), and we would therefore expect a smaller zonal wavelength. There is a difference in sign between profiles as to the direction of the meridional wavenumber, likely due to the different time and position at which the profiles were taken; however it is of similar magnitude to the zonal wavenumber. The negative sign on the zonal wavenumber is significant, because it indicates that the wave phase velocity opposes the mean flow. The non-negligible magnitude of the meridional wavenumber means that the total horizontal wave vector is not directed exactly westward against the predominantly eastward mean flow, as was also found in observational estimates of the momentum flux vectors. The vertical wavenumber is negative, indicating upward propagation, and the vertical wavelength is 1800 m for profile 32 and 1000 m for profile 26.

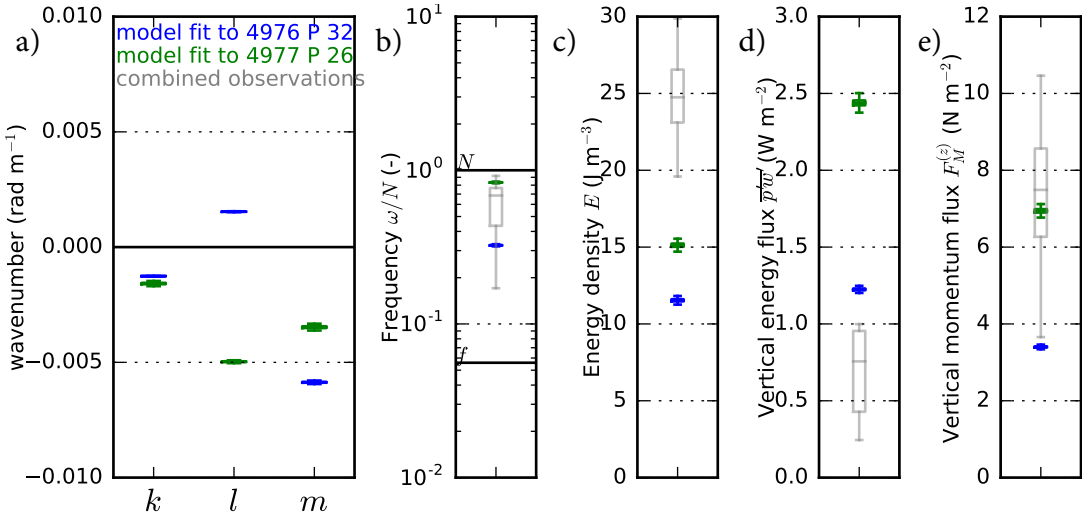

Figure 3.11: Comparison of linear internal wave fit-based diagnostics and direct estimates from observations for a) wavenumber components (for which there is no observational estimate); b) frequency normalised by buoyancy frequency; c) energy density; d) vertical energy flux; and e) vertical flux of horizontal momentum. The fits were conducted on profile 32 from float 4976 and profile 26 from float 4977.

The frequency determined from the fits is displayed in Figure 3.11b. It overlaps with the observational estimate (grey box and whisker), and is $0.3N$ for profile 32 and $0.8N$ for profile 26. Eulerian frequencies are 3×10^{-4} rad s^{-1} and 7×10^{-4} rad s^{-1}, corresponding to periods of 3 to 6 hours. If the horizontal wavevector has been underestimated, then so have these periods following from Equations (3.10) and (3.13). Thus, the wave is not perfectly stationary, but a fixed observer would notice a significant Doppler shift.

Energy density and the vertical fluxes of energy and horizontal momentum estimates are displayed in Figures 3.11c, d and e. The energy density of the best fits are 12 J m^{-3} and 15 J m^{-3}, smaller than the direct estimates from observations because the model has some difficulty in reproducing the full measured velocity amplitude. Energy fluxes are slightly larger than the direct estimates, at 1.2 W m^{-2} and 2.5 W m^{-2}, but within a factor of 2. Momentum fluxes are within the bounds of the direct estimates, with values of 3.5 N m^{-2} and 7 N m^{-2}.

In summary, while not providing a precise description, monochromatic plane waves do give a reasonable characterisation of the observed lee wave. This is estimated to have horizontal and vertical wavelengths in the range of 1 to 4 km; to propagate upward and against the eastward mean flow; to be quasi-stationary; and to transport energy and horizontal momentum vertically at large rates that are within a factor of 2 to 3 of the direct estimates.

3.3.3 Turbulent kinetic energy dissipation

A section of the rate of turbulent kinetic energy dissipation is displayed on a logarithmic colour scale in Figure 3.12. Results from Thorpe scale analysis are shown as large circles in Figure

3.12b and results from the large eddy method are displayed as small circles in Figure 3.12c. Background levels of dissipation in Drake Passage are typically of order 10^{-10} W kg^{-1}, less than the detection level of either method, and are blanked out over the majority of the section. Both methods indicate a patch of high dissipation above and in the lee of the ridge crest, coincident with profiles of large vertical velocity. Notably large overturns of order 10 m in scale are detectable using the Thorpe scale method, with dissipation rates in such patches approaching 10^{-6} W kg^{-1}, while the majority of overturns are smaller than this. The depth-integrated dissipation rate, $P = \int_{-Z}^{0} \rho \epsilon dz$, peaks at 20 mW m^{-2}.

Using the large eddy method, dissipation rates are found to be largest in the profiles containing the strongest wave signal, and peak at 10^{-7} W kg^{-1} at roughly 1000 m depth. The depth-integrated dissipation rate peaks at 6 mW m^{-2}, significantly less than the estimated vertical flux of energy associated with the wave. The sensitivity of these results to method parameter choices was assessed by systematically varying parameters, such as filter cut-off scale and window length, by various amounts up to a factor of 2. The spatial distribution of dissipation did not change, but the magnitude of the integrated dissipation rate varied by up to 20%.

3.4 Discussion and conclusions

In this chapter, observations of a wave-like feature in the vicinity of a sharp ridge made by two EM-APEX floats have been analysed to document the feature's physical characteristics. The limited number of profiles and the necessity of considering their time-dependent nature made analysis and interpretation of some properties challenging. Nonetheless, linear internal wave theory provides a good description of the dominant mode of variability, which has a positive vertical energy flux and negative vertical wavenumber, indicating upward propagation. The zonal phase velocity is directed westward, in opposition to the mean flow, resulting in a quasi-stationary pattern, while the meridional structure of the wave appears variable. This result, deduced from coherent oscillations of velocity and buoyancy over several wave periods, leads to the conclusion that the floats observed a lee wave, likely generated at the ridge and forced by the flow of the ACC. However, naive application of infinitesimal linear wave generation theory (Bell, 1975) for a near bottom flow speed of order 20 cm s^{-1}, near bottom stratification of 1×10^{-3} rad s^{-1} and topographic wavelength of 40 km imply that the resulting wave would be evanescent. This is in contradiction to the observations, which indicate a wave of frequency near N and wavelength closer to 4 km in the upper most 1500 m of the water column.

This contradiction may be resolved by considering the steepness parameter s. The steepness parameter is defined as the ratio of topographic height, h, to characteristic wave height, U/N, giving Nh/U, for a given near-bottom flow speed and stratification (Nikurashin and Ferrari, 2010a). Large values of s imply that the flow does not have sufficient kinetic energy to fully mount the topography, such that a deeper portion of the water column may be blocked or diverted

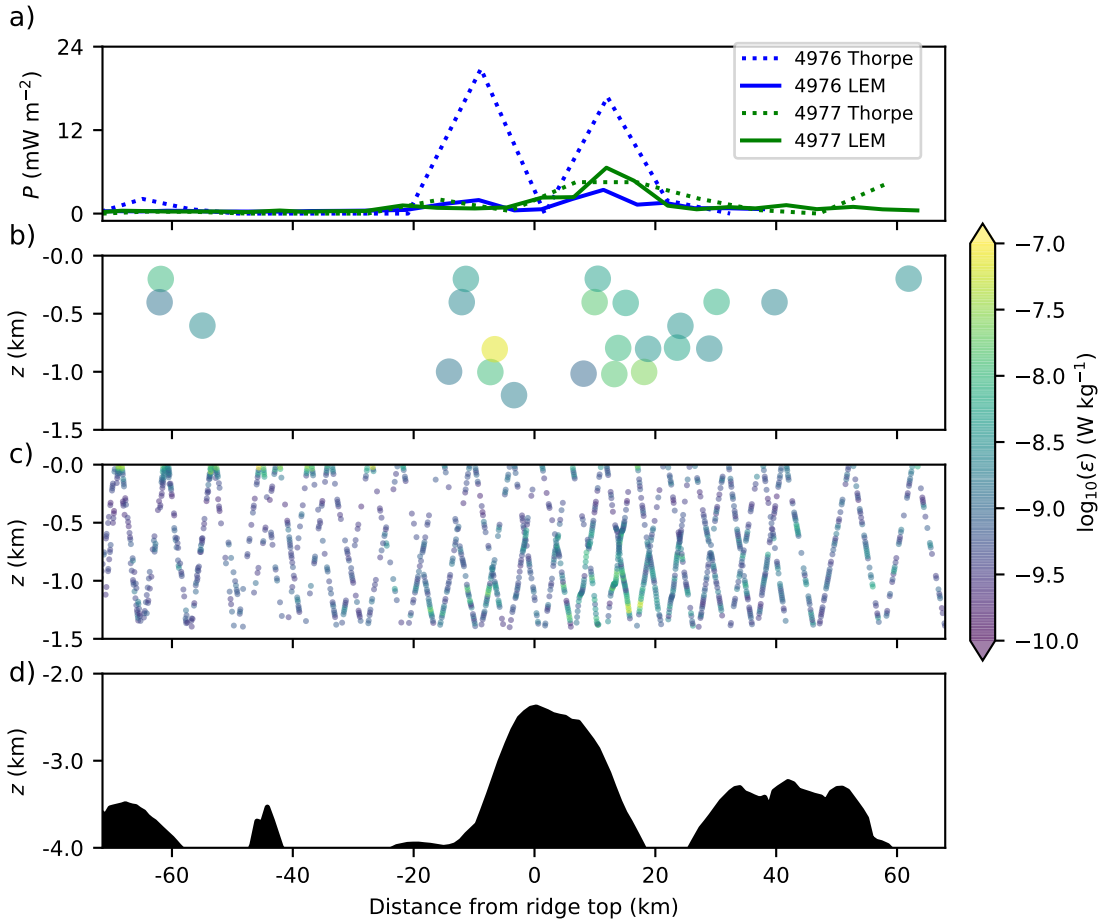

Figure 3.12: a) Depth-integrated TKED rate. b) Thorpe scale derived estimate of the TKED rate on a logarithmic scale, the large circles denote 200 m bin averages. c) Large eddy method (LEM) derived TKED rate calculated on a 20 m sliding window. d) Bathymetry. Measurements smaller than the noise threshold of the LEM, $c(w_{\mathrm{noise}})^2 N$, where the noise velocity, w_{noise} = 1 mm s^{-1}, have not been plotted. Similarly, portions of the water column where overturns are not detected have no associated Thorpe estimate.

making the wave generation process highly nonlinear. The value at which this transition occurs is in the range of 0.4 to 0.7, depending on topographic configuration (Aguilar and Sutherland, 2006; Nikurashin et al., 2014). Infinitesimal linear theory requires that the steepness parameter be much less than this value range. Given that the ridge height is roughly 1500 m, and that near-bottom stratification, as measured from ship-based CTD casts, is 0.8×10^{-3} rad s^{-1}, flow speeds in excess of 3 m s^{-1} would be required for a sufficiently small steepness parameter. This is not a physically reasonable speed for a near-bottom oceanic flow, and we conclude that the flow is highly likely to be blocked below some depth.

High-resolution modelling efforts in two and three dimensions using a domain analogous to the Drake Passage (Nikurashin et al., 2014) show that, for large values of the steepness parameter, the time-mean energy flux into lee waves saturates at 10 mW m^{-2}. For very long ridges in which the flow configuration is largely two-dimensional, the energy flux at generation saturates at 100 mW m^{-2}. These values are smaller than the energy fluxes estimated from our observations, of order 1 W m^{-2}, which are in good agreement with those for a propagating monochromatic plane

wave constrained by linear theory. It is possible to estimate the expected energy flux from linear theory (Bell, 1975) for the portion of the water column above the depth where blocking occurs. Doing so reduces the height of the topography to an effective height h_e. Taking h_e = 200 m, for which the topographic wavelength is roughly equal to the observed zonal wavelength of 4000 m, extrapolating the observed mean flow speed to be 0.2 m s^{-1} near ridge top, and using the ship based CTD estimate of stratification, we get a linear energy flux value of 0.5 W m^{-2}. This value is within a factor 3 of the observed value. We conclude that our observations are consistent with linear generation above a blocking level. However, we also acknowledge that important small scale bathymetric features may exist that are not resolved by the database used (Smith and Sandwell, 1997).

Observed integrated dissipation rates in the Southern Ocean (St. Laurent et al., 2012; Sheen et al., 2013) are typically less than 5 mW m^{-2}. Our estimated values are similar to this, however, there is some uncertainty in this result due to quantitative limitations of the Thorpe scale and large eddy methods. A significant finding of our work is that the diagnosed vertical energy flux is almost two orders of magnitude larger than the depth-integrated dissipation rate. This result lends support to the idea that not all lee wave energy is dissipated locally (Waterman et al., 2014), however, we are not able to deduce the fate of the wave energy from the limited observations available.

It is possible to make a basic assessment of the wave's propensity to shear instability, using the Richardson number, Ri = $N^2/(\frac{\partial u}{\partial z})^2$. A necessary condition for shear instability is that Ri < $\frac{1}{4}$ (Miles, 1961; Howard, 1961). For a single wave, the induced vertical shear $\frac{\partial u}{\partial z} = u_0 m$, where u_0 is the horizontal velocity amplitude and m the vertical wavenumber. For the criterion to be satisfied, we find that $m > 0.01$ rad m^{-1}. The observations indicate that m is less than this value by a factor of 2 to 4. In a process distinct from shear instability, a wave will become statically unstable when the ratio of the horizontal velocity amplitude to the horizontal phase speed, $u_0\omega/k > 1$ (Orlanski and Bryan, 1969), and evidence from numerical models suggests that this can occur at slightly less than 1 (Liu et al., 2010). Our estimate for the static stability is in the range 0.1 to 0.25, within a factor of 4 to 10 of the condition. These estimates indicate that the wave, at its point of observation, is on the verge of undergoing shear and / or static instability. Interaction with the mean flow, changing stratification or other waves may play a role in inducing or amplifying such instabilities.

A significant fraction of the diagnosed vertical flux of horizontal momentum associated with the wave was oriented in opposition to the mean flow, which is approximately zonal. Significant non-zonal components of the momentum flux are likely a consequence of the nonlinear, three-dimensional nature of the generation process but could also be a result of spatio-temporal variability or advection. It was not possible to deduce the divergence of the momentum flux, and therefore, the implied drag force. However, the magnitude of the flux is more than two orders of

magnitude greater than the time-mean wind stress on the ACC (Wunsch, 1998), suggesting that lee waves have the potential to be a significant term in the local momentum budget of ACC jets as suggested by Naveira Garabato et al. (2013). Further work will be needed to understand the temporal and spatial occurrence of such wave events and a targeted observational campaign will be required to conclusively test this hypothesis.

This chapter documents the first unambiguous observation of a lee wave in the ACC. A thorough analysis of sparse observations was conducted to produce optimal estimates of wave properties, which are broadly consistent with inferences from previous, spatially incoherent finescale measurements. The extremely energetic nature of the wave is conducive to large vertical fluxes of energy and momentum and to the generation of significant amounts of turbulence, reinforcing current appreciation for the dynamically important role that lee waves likely play in the circulation of the Southern Ocean.

Chapter 4

Eddy - internal wave interaction

4.1 Introduction

Mesoscale eddies with horizontal scales of order 100 km are ubiquitous in the all the worlds oceans as is apparent from satellite altimetry measurements (Chelton et al., 2011). They emerge from barotropic and baroclinic instabilities in the mean flow as small perturbations that grow to a finite size, at which point non-linear dynamics dominate. Baroclinic generation feeds off potential energy in the background state, acting to reduce isopycnal slopes set up by atmospheric forcing at the ocean surface. Their dynamics are strongly influenced by the rotation of the Earth and as such are close to geostrophic. Particular hotspots of eddy activity exist in the Southern Ocean along the ACC path downstream of topographically rough areas and also where western boundary currents separate from the coast. Estimates of the kinetic energy of the ocean can be split into contributions from the mean flow and eddies, separating the two by averaging over an appropriate timescale. It has been found that eddying motions are generally several times more energetic, and in places up to two orders of magnitude more energetic than the mean flow (Ferrari and Wunsch, 2009). However, the dominant processes leading to eddy dissipation remain poorly understood.

The wind energy input into geostrophic flows has been estimated to be 0.85 - 1 TW (Scott and Xu, 2009) and numerous pathways to dissipate this energy have been postulated. These include lee wave generation through interaction with topography, investigated by applying linear wave generation theory to modelled currents and climatological stratification (Nikurashin and Ferrari, 2011), resulting in an estimated global transfer of 0.2 TW. Similar methods have been used to generate a higher estimate of 0.34 to 0.49 TW (Scott et al., 2011). High resolution numerical modelling analysis set up to approximate the Southern Ocean (Nikurashin et al., 2012) concluded that 80% of wind energy input to the model was dissipated by near bottom viscous processes, resulting from the interaction of geostrophic flows with bottom topography. Lateral boundary scattering of eddies to higher modes, investigated using a reduced gravity model and observations, leads to a global dissipation rate of 0.1 - 0.3 TW (Zhai et al., 2010). Surface frontogenesis and

submesoscale dynamics have also been advanced as candidates (Capet et al., 2008), although no global energy estimates have so far been made. Ferrari and Wunsch (2009) estimate that eddy - internal wave interactions may result in a global transfer of energy from eddies to internal waves of 0.35 TW, based on an extrapolation of the results of Polzin (2010). However, this result is based on limited observational evidence and the relative significant of eddy - wave interactions remains poorly constrained.

Internal waves range in spatial scale from metres to tens of kilometres, and in temporal scale from the buoyancy period to the inertial period. Their common appearance in oceanic measurements led to the development of the Garrett - Munk spectrum (e.g. Munk, 1980), which provided a foundation for decades of subsequent investigation. The first extensive theoretical investigation of internal wave - eddy interactions (Muller, 1976) was motivated by the desire to design a parameterisation of the process suitable for inclusion in numerical models. Muller (1976) argues that the interaction can be treated as a viscous diffusion of eddy momentum, proportional to a viscosity coefficient multiplied by an eddy velocity gradient. The assumptions underlying this simplification are that the internal wave velocity perturbations, spatial scale and temporal scale are all small and distinct from those of the eddying field such that the Wentzel-Kramer-Brillioun-Jeffreys (WKBJ) approximation can be applied. Furthermore, the mean flow is required to be quasigeostrophic so that wave action, equal to wave energy divided by the intrinsic frequency, E/ω_0, is conserved. Non-linear interactions between waves are assumed to relax the internal wave field to a background spectrum that is independent of the eddy flow, and the characteristic timescale of this process should be short enough that the wave-eddy interaction is localised. Assuming a Garrett-Munk energy spectrum, Muller (1976) produces order of magnitude analytical estimates of the resulting horizontal and vertical viscosity parameters, which are $\nu_h = 7$ m^2 s^{-1} and $\nu_v = 0.4$ m^2 s^{-1} respectively. The vertical viscosity in particular, was significantly larger than those typically used in numerical models at the time (Smagorinsky, 1963), and is certainly larger than measurements of turbulent diffusivity for most of the water column $< 10^{-4}$ m^2 s^{-1} (e.g. Polzin et al., 1997).

Experimental investigation of the interaction began with an analysis of moored current meter observations from the Mid Ocean Dynamics Experiment (MODE) (Frankignoul, 1976), located in the Sargasso sea (28°N, 69°40'W), at depths of 400 and 700 m. The study could not produce a confident estimate of the horizontal viscosity, but did conclude that the vertical viscosity was less than or equal to 0.1 m^2 s^{-1}. The analysis suffered from a relatively short time series of less than 100 days at both depths. Further investigation (Frankignoul and Joyce, 1979) using another short, 42 day, dataset from the Internal Wave Experiment (IWEX), concluded that the vertical viscosity was less than the noise threshold of the measurements and could not be more than 0.01 m^2 s^{-1}. Ruddick and Joyce (1979) arrived at a similar conclusion using data from POLYMODE, a joint U.S. - U.S.S.R. program, concluding that the vertical viscosity could not be more than 0.02 m^2 s^{-1}. Brown and Owens (1981) analysed a 180 day record from POLYMODE Local Dynamics

Experiment (LDE) and deduced a horizontal viscosity of 200 - 400 $m^2\ s^{-1}$. A reanalysis of LDE data (Polzin, 2010) produced a smaller horizontal viscosity, $\sim 50\ m^2\ s^{-1}$, and a vertical viscosity of $(2.5 \pm 0.3\times)10^{-3}\ m^2\ s^{-1}$, citing a possible error in the work of Brown and Owens (1981) for the large discrepancy between these results. In summary, previous observational estimates, all of which were confined to the Northwest Atlantic ocean, have concluded that the vertical viscosity of wave - eddy interactions is likely to be several orders of magnitude smaller than the theoretical estimate of Muller (1976), whereas the horizontal viscosity could be an order of magnitude larger.

Polzin (2010) went further and estimated the dissipation of eddy energy attributable to internal wave stresses, producing a value of 3×10^{-10} W kg^{-1} due to horizontal stresses and 1×10^{-10} W kg^{-1} to vertical stresses. This is an order of magnitude smaller than the estimated transfers of energy between eddies and the mean flow (Bryden, 1982), but similar in magnitude to simple estimates of dissipation in the bottom boundary layer. Difficulty in estimating an energy budget arises from the fact that net transfer from the mean to eddies is the residual of three large and uncertain quantities. Moreover, other mechanisms of eddy energy dissipation are poorly constrained. As a result, the significance of internal wave - eddy interactions in the eddy energy budget remains difficult to quantify.

This chapter attempts to construct a picture of the energy balance of eddies using observations from an array of moorings in the Southern Ocean, with a focus on the role of eddy - internal wave interactions. It presents the first analysis of the topic outside of the Northwest Atlantic in one of the world's major eddy kinetic energy hotspots. We begin with a brief outline of the theory necessary for interpreting the observations, followed by a description of the methods. While the method is largely the same as presented in previous works, more effort is made to gain insight into the internal wave field and the nature of the correlation between eddy strain and wave stress. The final section discusses the findings in the context of the energetics of the Southern Ocean.

4.1.1 Energy equations

The interaction of fluid processes which differ significantly in temporal and/or spatial scale can be treated mathematically by decomposing the equations of motion into a fluctuating component, usually denoted by a prime, ψ', and a mean component usually denoted by an overbar, $\overline{\psi}$. Here, ψ, represents any variable such as velocity or buoyancy and the total field is the sum of the two, $\psi = \overline{\psi} + \psi'$. The overbar denotes a temporal or spatial average such as, $\overline{\psi} = \frac{1}{T}\int_0^T \psi dt$, and by definition the average over the fluctuating component is equal to zero, $\int_0^T \psi' dt = 0$.

This chapter is concerned with the transfer of energy between the fluctuating field and the large scale flow. Such exchanges can be diagnosed from the energy equations for the fluctuating and large scale components. The energy equations are derived from the Buossinesq equations of motion on an f plane by multiplying the mean momentum equation by the mean velocity

and summing it with the mean buoyancy equation multiplied by the mean buoyancy. Following (Muller, 1976), the equation for the sum of mean kinetic and mean potential energy, denoted E, is found to be

$$\begin{aligned}&\left(\frac{\partial}{\partial t}+\overline{u}_j\frac{\partial}{\partial x_j}\right)E+\frac{\partial}{\partial x_i}\left(\overline{pu_i}+N^{-2}\overline{b}M_j\right)\\&=-\overline{u_i}\frac{\partial\overline{u_i'u_j'}}{\partial x_j}+N^{-2}\overline{b'u_j'}\frac{\partial\overline{b}}{\partial x_j}+\overline{bb'u_3'}\frac{\partial N^{-2}}{\partial x_3}+\frac{1}{2}\overline{b}^2\overline{u}_3\frac{\partial N^{-2}}{\partial x_3}\end{aligned}\tag{4.1}$$

where tensor notation has been used and summation over repeated indices is assumed. The indices i and j represent spatial components and can take integer values from 1 to 3. The total energy is defined as

$$E=\frac{1}{2}\overline{u_iu_i}+\frac{1}{2}N^{-2}\overline{b^2}.\tag{4.2}$$

Molecular diffusion has been neglected in the above decomposition, pressure has been divided by density and the background stratification N is assumed to be a function of height only. Equation (4.1) is relatively general and the definition of the fluctuating field as an internal wave field or the mean flow as a QG eddy field leads to further simplification. The equation has been split such that advective and transport processes are on the left and energy exchanges are on the right hand side. The energy equation for the fluctuating field is given by

$$\begin{aligned}&\left(\frac{\partial}{\partial t}+\overline{u}_j\frac{\partial}{\partial x_j}\right)E'+\frac{\partial}{\partial x_i}\overline{p'u_i'}\\&=-\overline{u_i'u_j'}\frac{\partial\overline{u}_i}{\partial x_j}-N^{-2}\overline{b'u_j'}\frac{\partial\overline{b}}{\partial x_j}+\frac{1}{2}\overline{b'b'}\overline{u}_3\frac{\partial N^{-2}}{\partial x_3}\end{aligned}\tag{4.3}$$

where terms involving triple products of the fluctuating field have been omitted and the fluctuating energy is given by

$$E'=\frac{1}{2}\overline{u_i'u_i'}+\frac{1}{2}N^{-2}\overline{b'b'}.\tag{4.4}$$

4.1.2 Internal wave - eddy interactions

If Equation (4.3) represents the internal wave energy and fluxes due to interactions with a QG mean flow, the properties of these types of motion can be used to simplify the equation. Firstly, in the QG limit, the vertical velocity is smaller than the horizontal by a factor $\beta H/f$, and it is assumed that $\overline{u_3}=\overline{w}\sim 0$. Secondly, the vertical flux of buoyancy by linear internal wave motions is zero, $\overline{b'u_3'}=0$. The equation then reads,

$$\begin{aligned}&\left(\frac{\partial}{\partial t}+\overline{u}_\beta\frac{\partial}{\partial x_\beta}\right)E'+\frac{\partial}{\partial x_i}\overline{p'u_i'}\\&=-\overline{u_\alpha'u_\beta'}\frac{\partial\overline{u}_\alpha}{\partial x_\beta}-\overline{u_\alpha'w'}\frac{\partial\overline{u}_\alpha}{\partial z}-N^{-2}\overline{b'u_\beta'}\frac{\partial\overline{b}}{\partial x_\beta}\end{aligned}\tag{4.5}$$

where the indices α and β can be either 1 or 2, denoting the horizontal components. In the absence of any interaction, the terms on the left hand side of the equation would sum to zero and represent a balance between advection of waves by the mean flow and divergence in the wave energy flux. The terms on the right hand side describe the various components of the internal wave stress acting on gradients in the eddy flow field. Terms containing buoyancy represent the wave induced buoyancy flux acting on horizontal gradients in buoyancy; internal wave fluxes of buoyancy influence the eddy flow via thermal wind.

Equation (4.5) can be rearranged in a way that makes explicit the fact that only normal and shear strain rates are involved in the energy exchange. To perform this rearrangement the stress tensor, $\overline{u_\alpha'u_\beta'}$, is decomposed into a kinetic energy component and a deviatoric component

$$\overline{u_\alpha'u_\beta'}=\frac{1}{2}\overline{u_k'u_k'}\delta_{\alpha\beta}+\left(\overline{u_\alpha'u_\beta'}-\frac{1}{2}\overline{u_k'u_k'}\delta_{\alpha\beta}\right)\tag{4.6}$$

where $\delta_{\alpha\beta}$ is the equal to 1 if $\alpha=\beta$ otherwise it is equal to 0. Similarly the deviation tensor, $\frac{\partial\overline{u}_\alpha}{\partial x_\beta}$, is split into three different components. A volumetric (divergence) component that contains compressive strain rates, a symmetric distortion component that contains the normal and shear strain rates, and an antisymmetric rotational component.

$$\frac{\partial\overline{u}_\alpha}{\partial x_\beta}=\frac{1}{2}\frac{\partial\overline{u}_k}{\partial x_k}\delta_{\alpha\beta}+\left(\frac{1}{2}\left(\frac{\partial\overline{u}_\alpha}{\partial x_\beta}+\frac{\partial\overline{u}_\beta}{\partial x_\alpha}\right)-\frac{1}{2}\frac{\partial\overline{u}_k}{\partial x_k}\delta_{\alpha\beta}\right)+\frac{1}{2}\left(\frac{\partial\overline{u}_\alpha}{\partial x_\beta}-\frac{\partial\overline{u}_\beta}{\partial x_\alpha}\right)\tag{4.7}$$

For a QG mean flow, the horizontal divergence is zero to a good approximation, $\frac{\partial\overline{u}_k}{\partial x_k}=0$, and the equation simplifies to

$$\frac{\partial\overline{u}_\alpha}{\partial x_\beta}=\left(\frac{1}{2}\left(\frac{\partial\overline{u}_\alpha}{\partial x_\beta}+\frac{\partial\overline{u}_\beta}{\partial x_\alpha}\right)-\frac{1}{2}\frac{\partial\overline{u}_k}{\partial x_k}\delta_{\alpha\beta}\right)+\frac{1}{2}\left(\frac{\partial\overline{u}_\alpha}{\partial x_\beta}-\frac{\partial\overline{u}_\beta}{\partial x_\alpha}\right)\tag{4.8}$$

Substituting Equations (4.6) and (4.8) back into the Equation (4.5) and summing over tensor components leads to the final result

$$\begin{aligned}&\left(\frac{\partial}{\partial t}+\overline{\boldsymbol{u}_h}\cdot\boldsymbol{\nabla}_h\right)E'+\boldsymbol{\nabla}\cdot\overline{p'\boldsymbol{u}'}\\&=-\frac{1}{2}\left(\overline{u'u'}-\overline{v'v'}\right)\left(\frac{\partial\overline{u}}{\partial x}-\frac{\partial\overline{v}}{\partial y}\right)-\overline{u'v'}\left(\frac{\partial\overline{v}}{\partial x}+\frac{\partial\overline{u}}{\partial y}\right)\\&\quad-\left(\overline{u'w'}-fN^{-2}\overline{b'v'}\right)\frac{\partial\overline{u}}{\partial z}-\left(\overline{v'w'}+fN^{-2}\overline{b'u'}\right)\frac{\partial\overline{v}}{\partial z},\end{aligned}\tag{4.9}$$

where thermal wind balance has been used to substitute horizontal buoyancy gradients for vertical shears, $\left(\frac{\partial b'}{\partial x}, \frac{\partial b'}{\partial y}\right) = f\left(\frac{\partial \overline{v}}{\partial z}, -\frac{\partial \overline{u}}{\partial z}\right)$. Traditional vector calculus notation is now used and the subscript h denotes horizontal components only. It can be seen that purely rotational eddy motions are not involved in energy exchanges between the two fields.

Following Polzin (2010), we assume a flux - gradient closure, whereby the fluctuating stresses are related to the large scale velocity gradients multiplied by a coefficient of viscosity.

$$-2\overline{u'v'} = \nu_h S_s \tag{4.10}$$

$$\overline{u'u'} - \overline{v'v'} = \nu_h S_n \tag{4.11}$$

$$\overline{u'w'} - \frac{f}{N^2}\overline{b'v'} = -(\nu_v + \frac{f^2}{N^2}K_h)\frac{\partial \overline{u}}{\partial z} \tag{4.12}$$

$$\overline{v'w'} + \frac{f}{N^2}\overline{b'u'} = -(\nu_v + \frac{f^2}{N^2}K_h)\frac{\partial \overline{v}}{\partial z} \tag{4.13}$$

where $S_s = \frac{\partial \overline{v}}{\partial x} + \frac{\partial \overline{u}}{\partial y}$ is the shear strain rate, $S_n = \frac{\partial \overline{u}}{\partial x} - \frac{\partial \overline{v}}{\partial y}$ is the normal strain rate and $(\nu_v + f^2/N^2 K_h)$ is the effective vertical viscosity from the combined effect of vertical stresses and buoyancy fluxes. The coefficients ν_h and ν_v represent horizontal and vertical viscosity respectively, and K_h is a diffusivity associated with buoyancy fluxes. Analytical expressions for these viscosities are derived by Muller (1976), however, assuming the validity of the approximation, they can be deduced from observations by fits to stress and strain data. Theoretical arguments for the flux - gradient relationship rely on the assumption that non-linear processes in the internal wave field relax the wave action spectrum to a background state in a time short enough that that the interaction is localised.

The total energy flux from eddies to waves is estimated as the viscosity multiplied by the variance of the eddy velocity gradient. It can be derived from Equation (4.9) by substituting in the flux - gradient equations to arrive at

$$\begin{aligned}&\left(\frac{\partial}{\partial t} + \overline{\boldsymbol{u}_h} \cdot \boldsymbol{\nabla}_h\right)E' + \boldsymbol{\nabla} \cdot \overline{p'\boldsymbol{u}'} \\ =&\frac{1}{2}\nu_h\left(S_n^2 + S_s^2\right) + \left(\nu_v + \frac{f^2}{N^2}K_h\right)\left(\left(\frac{\partial \overline{u}}{\partial z}\right)^2 + \left(\frac{\partial \overline{v}}{\partial z}\right)^2\right).\end{aligned} \tag{4.14}$$

4.1.3 Eddy - mean flow interaction and dissipation

Following Bryden (1982) we estimate the magnitude and direction of energy fluxes due to various possible interactions of eddies with the mean flow. This is done by using observations to estimate the value of interaction terms in the energy equation (Equations (4.1) and (4.3)). Eddy motions are now denoted with a superscript * to distinguish them from internal wave motions. The second

term on the right hand side of Equation (4.3) concerns the conversion of mean available potential energy into eddy kinetic energy via baroclinic instability is denoted F_{PK} as follows,

$$F_{PK} = \frac{\rho_0 f}{\frac{\partial \overline{\rho}}{\partial z}} \left(\overline{v^* \rho^*} \frac{\partial \overline{u}}{\partial z} - \overline{u^* \rho^*} \frac{\partial \overline{v}}{\partial z} \right), \tag{4.15}$$

where ρ_0 is the mean density. The conversion of mean kinetic energy into eddy kinetic energy via barotropic instability is the first term on the right hand side of Equation (4.3),

$$F_{ME} = -\left(\overline{u^{*2}} \frac{\partial \overline{u}}{\partial x} + \overline{u^* v^*} \left(\frac{\partial \overline{u}}{\partial y} + \frac{\partial \overline{v}}{\partial x} \right) + \overline{v^{*2}} \frac{\partial \overline{v}}{\partial y} \right). \tag{4.16}$$

The production of mean kinetic energy by eddies is given by the first term on the right hand side of Equation (4.1),

$$F_{EM} = -\overline{u} \left(\frac{\partial \overline{u^* u^*}}{\partial x} + \frac{\partial \overline{u^* v^*}}{\partial y} \right) - \overline{v} \left(\frac{\partial \overline{u^* v^*}}{\partial x} + \frac{\partial \overline{v^* v^*}}{\partial y} \right). \tag{4.17}$$

Finally, bottom boundary layer dissipation of eddy kinetic energy is assumed to be a cubic function of near bottom eddy speed, u_b^* with a drag coefficient of 2×10^{-3}.

$$F_{bbl} = \rho C_d u_b^{*3} \tag{4.18}$$

The cubic form of the equation follows from a quadratic form of the bottom boundary stress (Gill, 1982).

4.2 Method

4.2.1 Data acquisition

The majority of the analysis in this chapter uses data from an array of 5 moorings located just south of Burwood Bank in the Scotia sea, as indicated by the cross in Figure 4.1. Their position puts them close to the climatological position of the SAF (Orsi et al., 1995). They were originally deployed over the 9th - 11th of December 2009, subsequently recovered over the 6th - 7th of December 2010 and redeployed on the 18th - 20th December 2010 and finally recovered on the 5th and 6th of March 2012. The analysis in this chapter considers only the latter half of this dataset and is 438 days long. Utilising the full dataset is a work in progress that is complicated by several instrument losses during the first year. The moorings were positioned in a cross pattern, as shown in Figure 4.2, the diagonal distance between corners being approximately 15.5 km. Individual moorings are denoted by their cardinal position in the array such that the north east

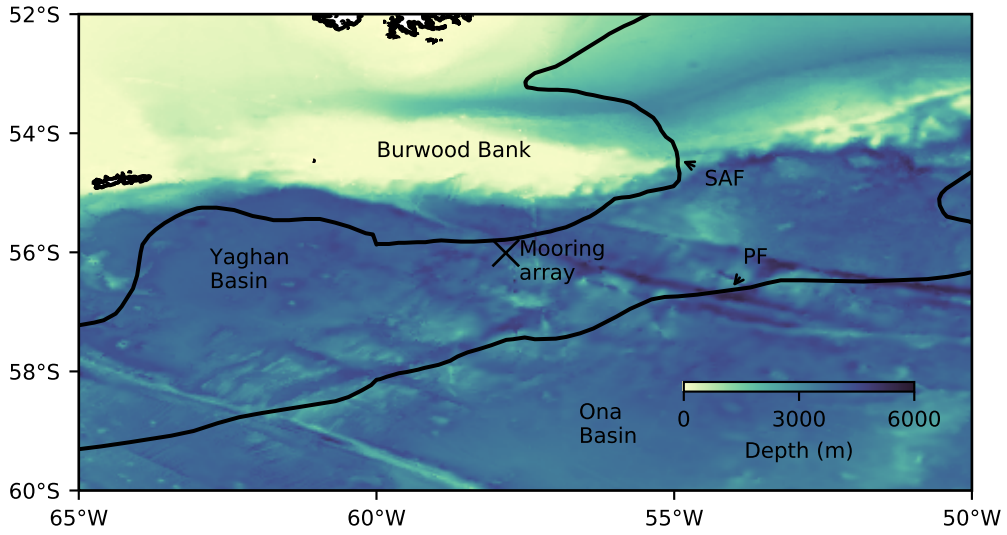

Figure 4.1: The position of the mooring array is denoted by a cross. Topography (Smith and Sandwell, 1997) is coloured. The climatological position of the SAF and PF are displayed with dark lines.

mooring is denoted NE for example. The central mooring, denoted C, was positioned near the top of a small sea mount which rose to ~ 3650 m depth.

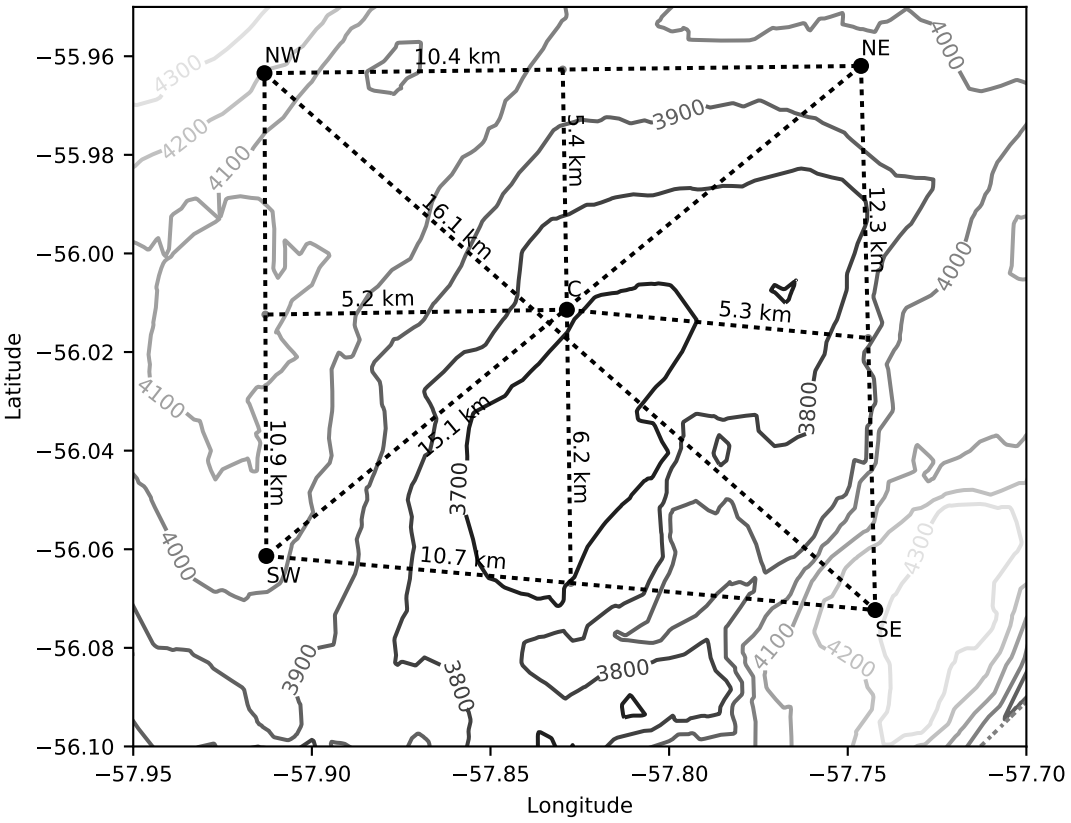

Figure 4.2: Mooring locations are denoted by filled circles and distances by dashed lines. Topography observed by multibeam swath sounding is contoured in 100 m increments.

The instrumentation on the moorings consisted of pairs of current meters and CTD probes

providing colocated observations of temperature, salinity, pressure and horizontal current speed at 15 minute intervals. NORTEK acoustic current meters were used on the central mooring while all other moorings used Seaguard meters. All moorings used Seabird Electronics SBE 37-SMP pumped MicroCAT for CTD measurements. Figure 4.3 displays the histogram of depths for each instrument pair as well as their most frequent position. The distributions have a large peak and a long tail, produced by occasional knockdown events associated with strong currents, which can be seen in Figure 4.4. The central mooring used 12 instrument pairs whereas the other moorings used 5.

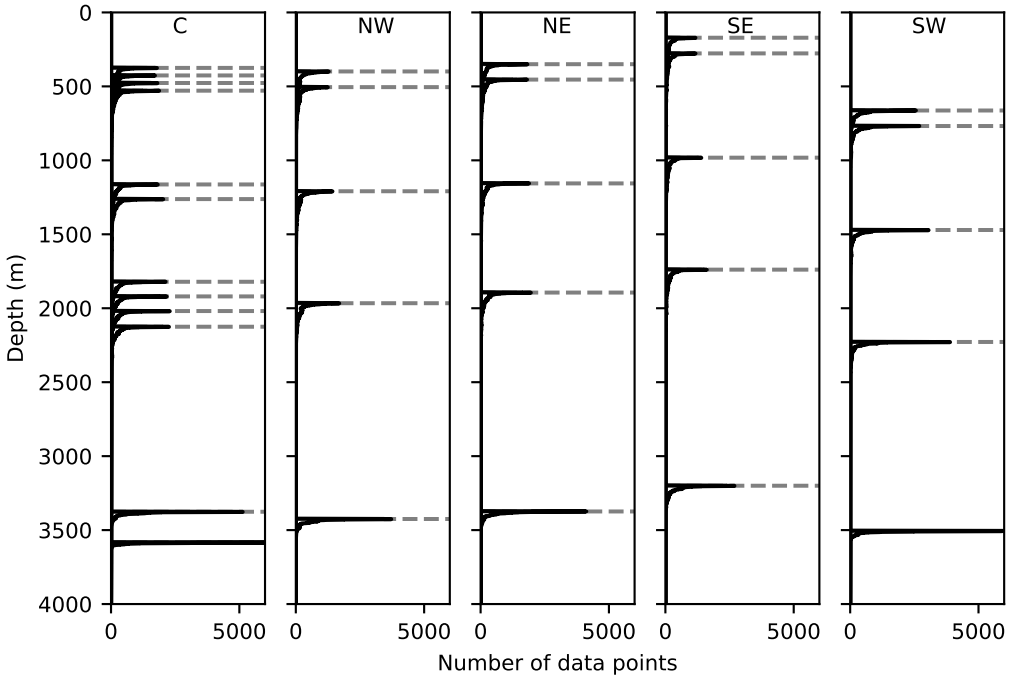

Figure 4.3: All recorded instrument depths have been binned into 1 m intervals and displayed as histograms. The horizontal dashed lines indicate the most frequent depth of the instrument.

When chopped to the longest common length of time, the data consists of 42048 records from each instrument, corresponding to 438 days of data with a 15 minute sampling period (96 samples per day). Early instrument failure for current meters at approximate pressures 2200 dbar and 1500 dbar on the SW mooring resulted in a reduced record length of 28117 samples (292 days) for those instruments.

Prior to analysis, mooring data is adjusted to a common level so as to make horizontal derivatives calculable, which is especially important during knockdown events. This is done using the method described in Brearley et al. (2013) which is similar to that described by Phillips and Rintoul (2000). The essence of the adjustment is the definition of reference profiles of temperature and salinity, calculated by fitting cubic polynomials to low pass filtered data. The adjusted temperature or salinity is then found by interpolation using a distance weighted average of the canonical profile and measured data from instruments. Velocity data is interpolated using specific volume anomaly as the interpolant, assuming geostrophy. The fixed levels are 450, 550, 1200, 2000 and 3500 dbar.

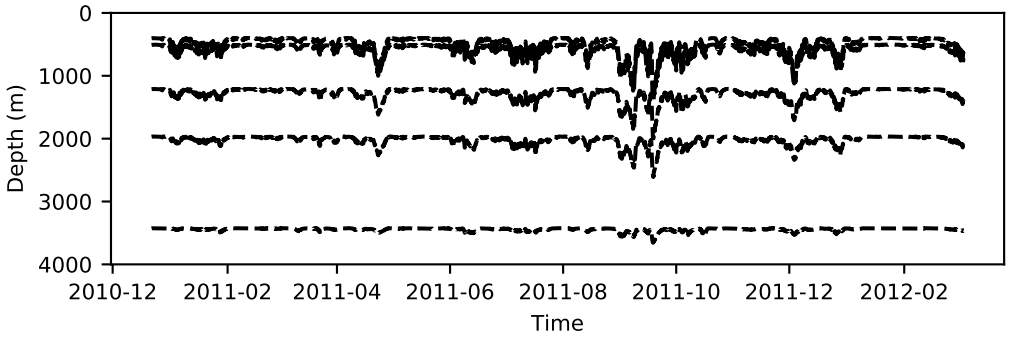

Figure 4.4: Time series of instrument depths for the NW mooring.

Vertical microstructure data

Measurements of the turbulent dissipation rate, ϵ, were taken during the second U.K. DIMES cruise aboard *RRS James Cook* using two Rockland Scientific VMP 5500 vertical microstructure profilers, one from Woods Hole Oceanographic Institute (U.S.A) and the other from the National Oceanography Centre (U.K.). This was the same cruise that recovered and redeployed the moorings. Detailed description of the processing and initial data analysis in available in the cruise report (Meredith, 2011). It suffices to say that 15 VMP stations were conducted between the 8th and 23rd of December 2010 in the vicinity of the mooring array, and their location relative to the moorings is displayed in Figure 4.5.

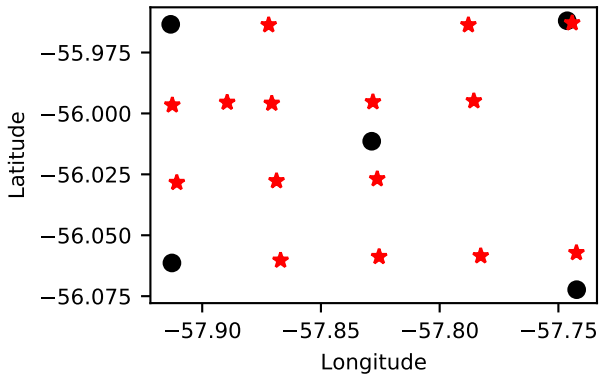

Figure 4.5: VMP stations, denoted by stars and mooring locations by circles.

4.2.2 Definition of mean, eddy and internal wave fluctuations

A measured variable, q, such as temperature, salinity or velocity is decomposed in the following way

$$q(\boldsymbol{x}, t) = \overline{q}(\boldsymbol{x}) + q^*(\boldsymbol{x}, t) + q'(\boldsymbol{x}, t) \tag{4.19}$$

where q, denotes the unfiltered quantity, $\overline{q}$, the mean, q^*, the eddy fluctuation and q' the internal wave fluctuations. The mean is defined as the time average over the whole record period

of 438 days. The internal wave fluctuations are isolated by high pass filtering using a 4th order Butterworth filter with a 40 hour cut off period. Eddy fluctuations are defined by the residual of the other quantites according to Equation (4.19). Defining the internal wave fluctuations using a cut off period greater than $2\pi/f$ will lead to the inclusion of sub-inertial processes. To avoid this, internal wave stresses are estimated in frequency space by performing an integral over the internal wave band, which is explained in more detail in the following sections.

4.2.3 Vertical velocity and buoyancy

Vertical velocity is estimated by assuming a vertical balance in the density equation, whereby changes in density at a given instrument are caused by vertical advection of the eddy density gradient by internal waves. Uncertainty in this value comes from two sources, the estimation of the internal wave induced density perturbation itself, which is sensitive to the mooring motion adjustment, especially for large knockdowns. The second source of uncertainty is the estimation of the eddy density gradient, which is estimated using instruments spaced far apart in the vertical. The following equation describes the balance,

$$w' \frac{\partial}{\partial z}(\overline{\rho} + \rho^*) = \frac{\partial \rho'}{\partial t} \tag{4.20}$$

Internal wave buoyancy perturbation, b', is estimated from neutral density (Jackett and McDougall, 1997) perturbations at the adjusted levels using the following equation,

$b' = -\frac{g}{\rho_0}\rho'$

where $\rho_0 = 1000$ kg m^{-3}.

4.2.4 Horizontal gradients of eddy quantities

The finite difference approximation

To estimate quantities such as the eddy shear strain $S_s = \frac{\partial v^*}{\partial x} + \frac{\partial u^*}{\partial y}$ using in-situ data it is necessary to deploy the finite difference approximation of the derivative, $S_s \approx \frac{\Delta v^*}{\Delta x} + \frac{\Delta u^*}{\Delta y}$, where a Δ denotes the difference between two discrete values. To compute this, we construct triangles or crosses using groups of three or four moorings as illustrated in Figure 4.6. Quantities at specific moorings are denoted with the mooring subscript, e.g. u^*_{C}, u^*_{NE} or u^*_{SE}. In the example in Figure 4.6a the meridional gradient of zonal velocity is simply estimated as $\frac{u^*_{\mathrm{NE}} - u^*_{\mathrm{SE}}}{y_{\mathrm{NE}} - y_{\mathrm{SE}}}$, a second order accuracy central difference. The zonal gradient of meridional velocity is complicated by the lack of a fourth mooring east of, and at the same latitude as the central mooring, so it is necessary to construct a 'virtual' mooring, by averaging quantities from the NE and SE moorings. The location of this virtual mooring, which will be denoted with a subscript E, is at the midpoint of the NE

and SE moorings with position given by $(x_E, y_E) = \frac{1}{2}(x_{NE} + x_{SE}, y_{NE} + y_{SE})$. Finally, the zonal gradient of meridional velocity is calculated as $\frac{v^*_E - v^*_C}{x_E - x_C}$, a first order forward difference. Similar triangles can be constructed for each face and vertex of the mooring array, however, triangles at the vertices rely only on forward/backward differences and are therefore less accurate. We estimate strain at four virtual moorings at each face centre, W, N, E and S and then compute the strain at the central mooring by averaging these four. The reason for doing this is that loss of data from any one mooring does not compromise the time series at the centre. Computing derivatives at the central mooring using the four outer moorings, as in Figure 4.6c is found to give an indistinguishable result. Deviations of the mooring positions from a rectilinear grid will result in a bias in the estimated derivatives that we assume is negligible.

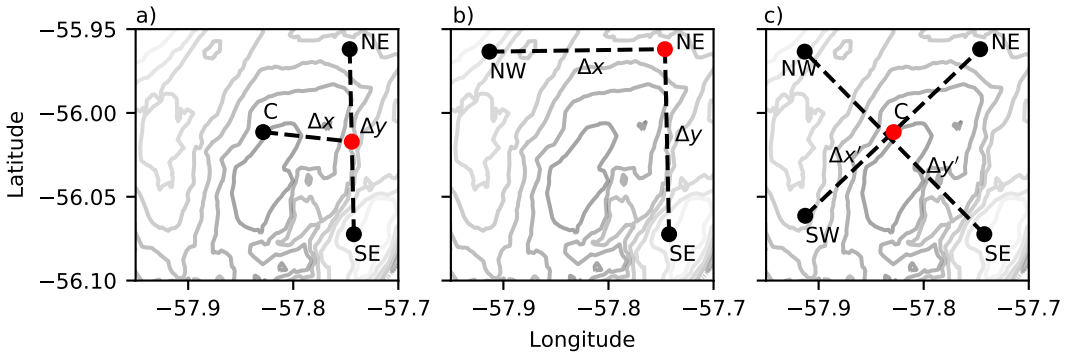

Figure 4.6: The possible finite difference configurations are a) accurate to first order at array edge centres, b) accurate to first order at array corners c) accurate to second order at the array centre. The red circle denotes the location at which the difference estimate is valid.

The derivatives are calculated at every time step and a comparison between moorings is displayed in Figure 4.7. The very good agreement between mooring estimates of strain is consistent at different depth levels (not shown). Before using the data in regressions a moving window average is computed, with the window size equal to 512 records, equivalent to just over 5 days, moving in increments of 96 samples, the same window size used to calculated internal wave stress.

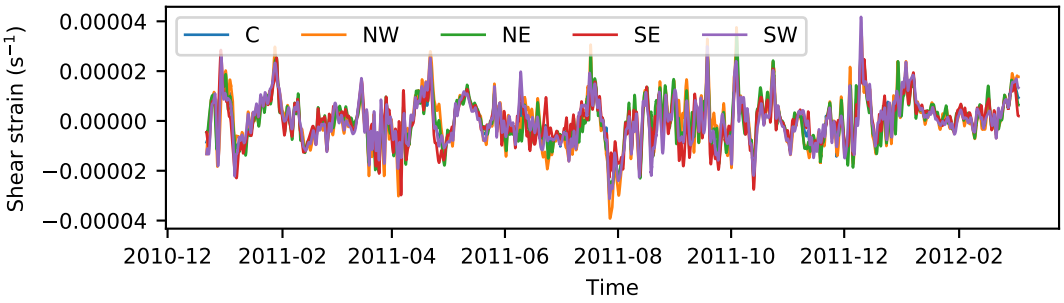

Figure 4.7: Eddy shear strain at 550 dbar estimated at the five mooring locations.

Stoke's theorem and the divergence theorem

Stoke's theorem applied to a two dimensional plane, also known as Green's theorem, provides an alternative framework for estimating horizontal gradients at the mooring array (Bryden and Fofonoff, 1977). Mathematically, the theorem is written as follows,

$$\iint \left(\frac{\partial v}{\partial x} - \frac{\partial u}{\partial y} \right) \mathrm{d}A = \oint \mathbf{u} \cdot \mathrm{d}\mathbf{s}, \tag{4.21}$$

which states that the integral of the vorticity over an area, A, is equal to the integral of the velocity tangent to the line enclosing that area. A similar relation can be derived for the area integral of the divergence,

$$\iint \left(\frac{\partial u}{\partial x} + \frac{\partial v}{\partial y} \right) \mathrm{d}A = \oint \mathbf{u} \cdot \mathrm{d}\mathbf{n}, \tag{4.22}$$

which is equal to the integral of the velocity normal to the line enclosing that area. Derivatives are assumed constant throughout the area, so that the equations are simplified.

$$\frac{\partial u}{\partial x} + \frac{\partial v}{\partial y} = \frac{1}{A} \oint \mathbf{u} \cdot \mathrm{d}\mathbf{n} \tag{4.23}$$

The individual components of the gradient can be calculated from the line integrals of the individual components of velocity, for example,

$$\frac{\partial u}{\partial x} = \frac{1}{A} \oint u n_x \, \mathrm{d}x, \tag{4.24}$$

where n_x is the component of the normal vector pointed in the x direction.

Vorticity, divergence and the individual velocity gradients were computed at the central mooring using line integrals around the four outer moorings and compared to the finite difference estimates. The array area was calculated using the shoelace formula. A comparison of vorticity and divergence calculated using finite differences and Stoke's method is displayed in Figures 4.8 and 4.9 respectively. The divergence and vorticity match so closely that they are not distinguishable from one another. Data loss at the SW mooring meant that line integrals were not calculable for most of the time series at depths of 1200 dbar and 2000 dbar. The mean absolute difference between the two methods is of order 2×10^{-7} s^{-1}, about two orders of magnitude smaller than the typical magnitude of the vorticity. Results presented in this chapter are based on derivatives calculated using the finite difference approximation only.

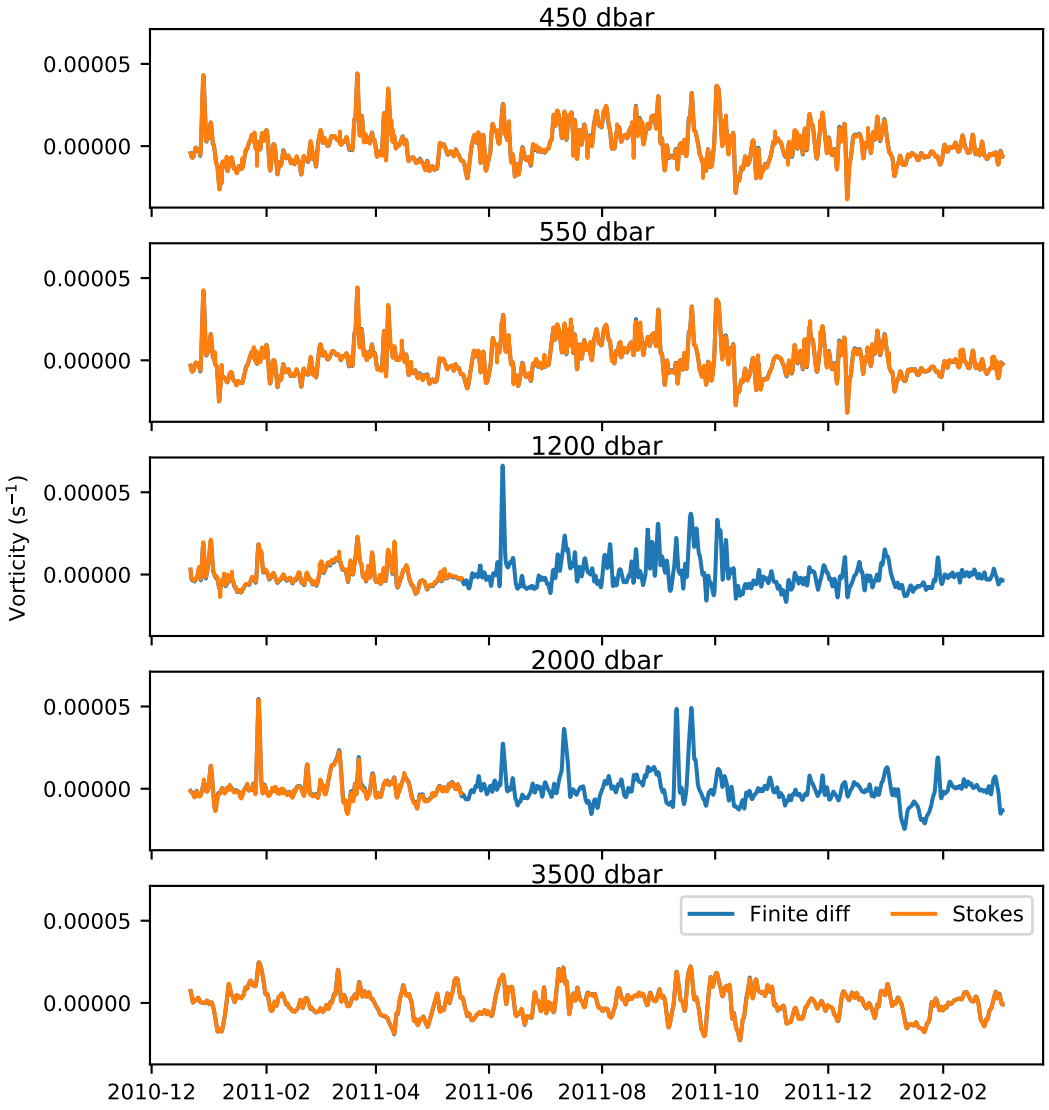

Figure 4.8: Vorticity time series at the central mooring computed using the finite difference method and Stoke's method. The results match so closely so as to be nearly indistinguishable.

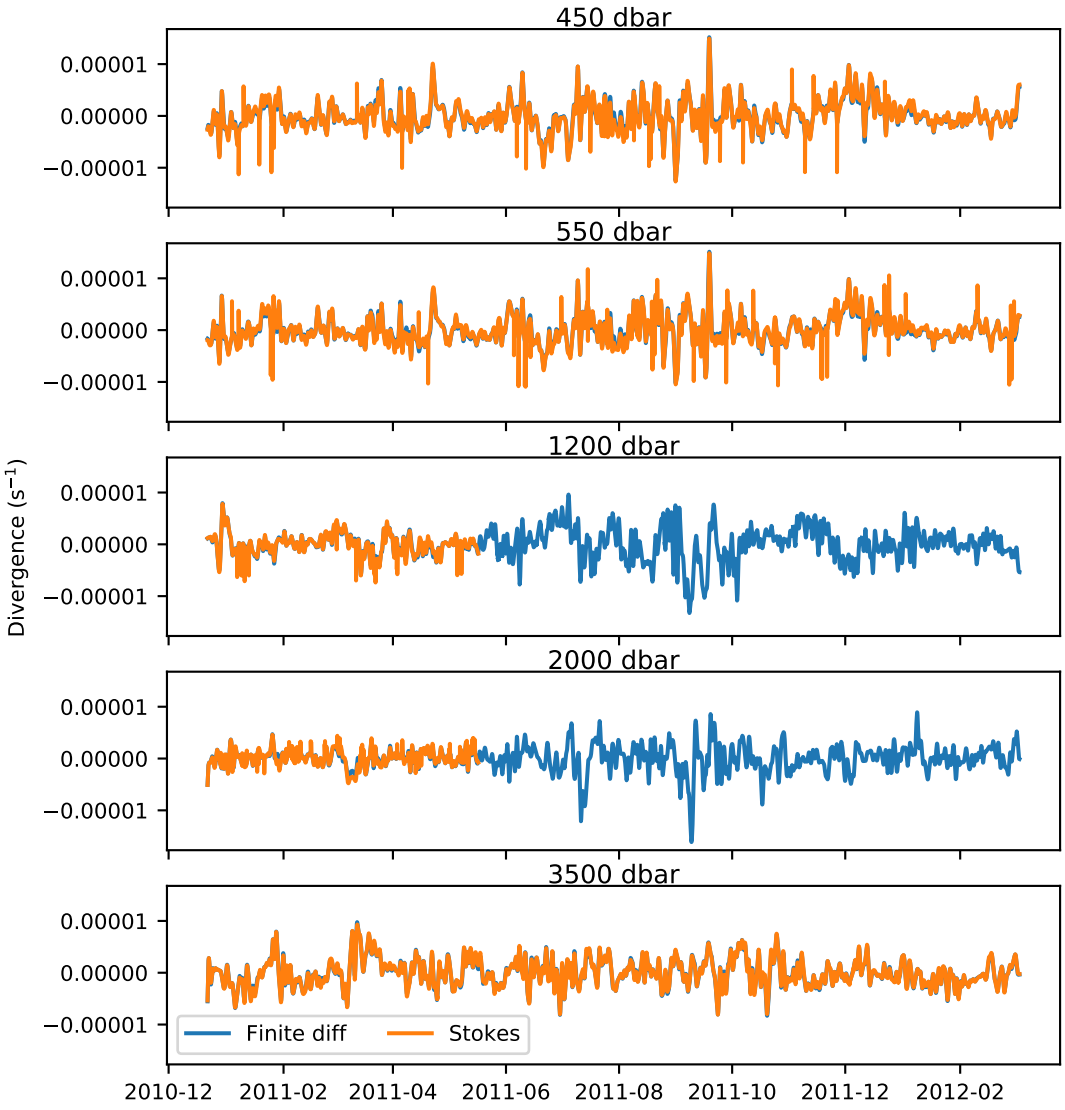

Figure 4.9: Divergence time series at the central mooring computed using the finite difference method and Stoke's method.

Error estimates

Frankignoul (1976) quantify the quality of the horizontal derivatives using the following ratio

$$R_D = \frac{\overline{\left|\frac{\partial u}{\partial x} + \frac{\partial v}{\partial y}\right|}}{\overline{\left|\frac{\partial u}{\partial x}\right|} + \overline{\left|\frac{\partial v}{\partial y}\right|}} \tag{4.25}$$

which should be of order Rossby number (Bryden and Fofonoff, 1977), $Ro = U/fL \sim 0.1$ for a QG flow. We find that R_D is in the range 0.33 to 0.45 at the central mooring and in the range 0.4 to 0.65 at the corner moorings. Bryden and Fofonoff (1977) also estimate the error due to finite difference approximation assuming the large scale flow can be represented locally by a plane wave, $u = u_0 e^{\mathbf{k}\cdot\mathbf{x}}$, with a dominant wave vector, $\mathbf{k}$. The ratio of the finite difference gradient to the true gradient in this case is given by,

$$\frac{\sin\left(\frac{1}{2}\mathbf{k}\cdot\Delta\mathbf{x}\right)}{\frac{1}{2}\mathbf{k}\cdot\Delta\mathbf{x}}, \tag{4.26}$$

where $\Delta\mathbf{x}$ is the spacing between the moorings. Thus the maximum error in the estimate, for an eddy with a wavelength of 50 km, aligned with moorings spaced 10 km apart is expected to be about 6%.

4.2.5 Horizontal internal wave stress

The internal wave shear stress, $-2\overline{v'u'}$ and normal stress $\overline{u'u'} - \overline{v'v'}$ are calculated in frequency space, by integrating the covariance and variance spectra, denoted C_{uv}, P_{uu} and P_{vv} (Frankignoul, 1976; Brown and Owens, 1981; Polzin, 2010), over the internal wave band. The velocity time series is first separated into segments containing 512 measurements (128 hours) that are centered at mid-day. The segmants are then multiplied by a hanning window prior to computing the spectra. The covariance spectra consist of a real part, called the cospectra, and an imaginary part called the quadrature spectrum. Only the cospectra is integrated because it contains the in-phase signal. The coherence is given by,

$$c^2 = \frac{|C_{uv}|^2}{P_{uu}P_{vv}} \tag{4.27}$$

and the significance level of the coherence when overlapping windows are used is given by Gallet and Julien (2011).

An example spectrum for a single segment is shown in Figure 4.10 with the integration limits. The variance rapidly declines in magnitude at higher frequencies.

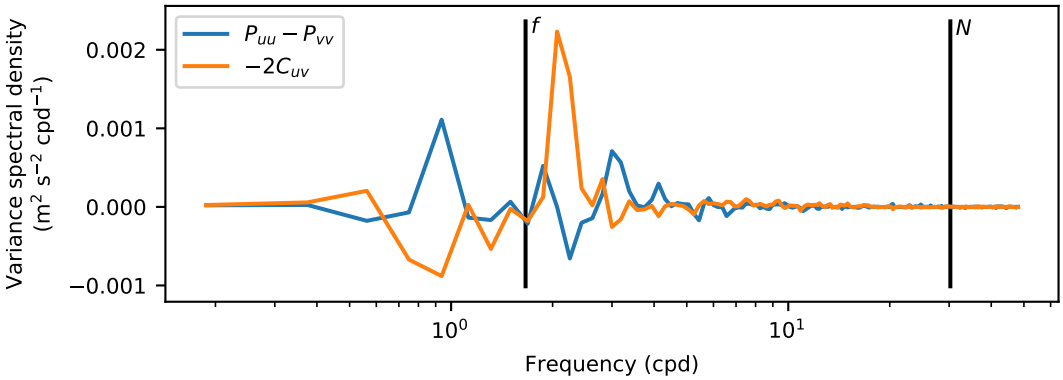

Figure 4.10: Example spectrum of internal wave normal and shear stress. The variance is zero at frequencies less than 0.5 cpd due to high pass filtering. The vertical lines indicate the inertial and buoyancy frequencies, which are also the limits of integration.

4.2.6 Wavelet analysis

The continuous wavelet transform has some analogies with a sliding Fourier transform in that it provides an estimate of the frequency content of a signal with time. We defer to Torrence and Compo (1998); Grinsted et al. (2004) for a discussion of the method and its application to geophysical time series. In this chapter, it is used to estimate the frequency content of the internal wave band as a function of time. Wavelet coherence is also computed to assess the coherence of two signals as a function of frequency and time. If the two signals are denoted X and Y, then the wavelet phase angle means the following: for negative (positive) angle, X leads (lags) Y. A phase angle of zero (180 degrees) means X and Y are in phase (anti phase). In the results below strain is equivalent to X and stress is equivalent to Y.

4.2.7 Tidal harmonic analysis

The barotropic tidal contribution to the velocity signal was investigated in two ways. The first was to extract the estimated tidal amplitude from the tidal inversion software OTIS (Egbert and Erofeeva, 2002) for a point near the mooring array. The data in this software ultimately comes from an inversion of the tidal equations to altimetry measurements from TOPEX/Poseidon altimetry. The second used the harmonic analysis package `utide` (Codiga, 2011) which is fitted to data from each instrument pair on the central mooring and then averaged over depth to isolate the barotropic component.

4.3 Results

To aid the flow of the chapter and reduce clutter we usually show figures from one mooring only. In general, conclusions drawn from the results could be drawn from any of the moorings. Where this is not the case, it is noted in the text.

4.3.1 Internal wave properties

Before calculating stress - strain regressions, we consider the properties of internal waves at the mooring array, focusing on the near inertial (NI) portion of the spectrum, roughly defined as $f/2$ to $2f$, which contains the majority of the energy. The record average NI variance spectrum of horizontal velocity computed using Welch's method with half overlapping windows of 16384 points, is displayed in Figure 4.11 for the NE mooring. Prominent peaks in variance at diurnal and semidiurnal frequencies are apparent at all depths, with a relative minima at mid-depth of 1200 dbar, away from boundary sources of wave energy. There is no clear peak at the inertial frequency at any depth, although the background spectrum does increase in variance going from high frequencies towards the inertial and then falls off rapidly at frequencies lower than the inertial. It is likely that Doppler shifting of NI frequencies is important at the shallower instrument levels and may explain the lack of a distinct NI peak. In general, variance at non-tidal frequencies diminishes with depth.

A more detailed picture of NI energy is given by the wavelet spectra in Figure 4.12. The quantity plotted is the squared magnitude of the wavelet velocity spectrum, proportional to the horizontal kinetic energy. It can be seen that, at all depths, near inertial energy appears in discrete events. At the deepest current meter, the M2 frequency band is highly energetic and very little energy exists at frequencies lower than the inertial. This is suggestive of internal tides and a lack of Doppler shifting, although the source of tidal energy may not be local. Towards the surface, energetic events are more spread out in frequency, which is indicative of stronger Doppler shifting.

It is not clear from Figure 4.12 whether near inertial energy is generally propagating upwards or downwards. Apart from the upper two levels, which are 100 m apart and nearly coherent, there is little correlation between levels. To address this question we assess the direction of wave phase propagation visually, and using the polarisation ratio metric. Internal wave vertical phase propagation is opposite to the direction of energy propagation, such that upward (downward) phase propagation implies downward (upward) energy propagation. The polarisation ratio contains information about the vertical rotation of the vertical shear vector and is composed of the counter clockwise rotating component of the internal wave vertical shear integrated over the internal wave band, divided by the integral of the clockwise rotating vertical shear component (Gonella, 1972). In the Southern Hemisphere $R_{\mathrm{pol}} > 1$ indicates an excess of downward propagating wave energy.

To analyse propagation direction, we use velocity data from the central mooring prior to interpolation, which was more heavily instrumented than the others (Figure 4.3), with one group of 4 current meters spaced 50 m apart centred at about 500 m depth and another group of 4 spaced 100 m apart centred at 2000 m. The data is band pass filtered between periods of 1 to 16 hours to select the internal wave band. Figures 4.13a and 4.13b display the zonal component

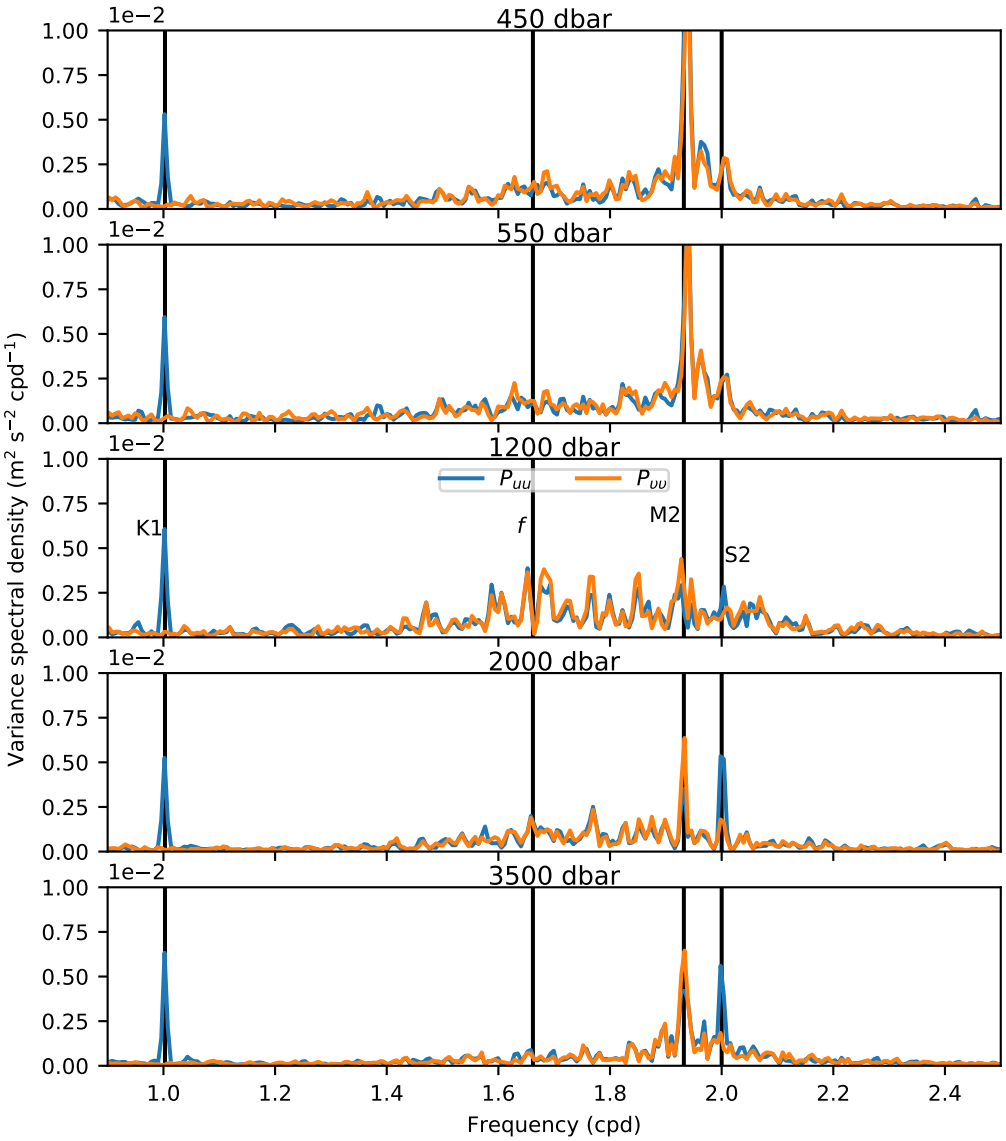

Figure 4.11: Near inertial spectrum of velocity variance at the NE mooring for five depth levels. Vertical lines denote tidal and inertial frequencies.

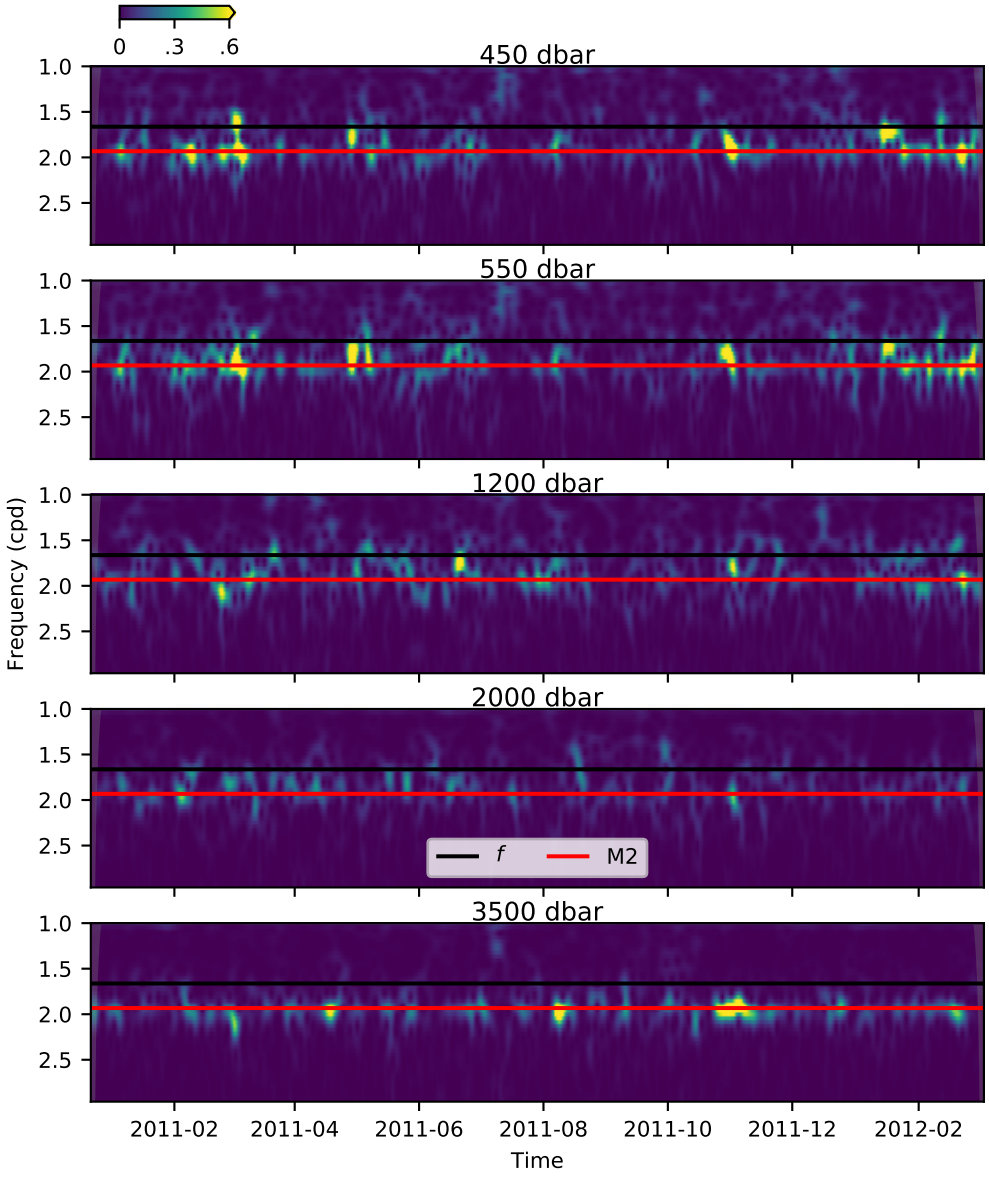

Figure 4.12: Wavelet spectra of horizontal velocity at C mooring. The colour represents the horizontal kinetic energy. Horizontal lines mark the inertial and M2 frequencies. A Morlet wavelet with scale 20 was used, as a compromise between temporal and frequency resolution.

of velocity for a short, but energetic, segment of the time series for which phase lines are clearly visible. It is difficult to deduce by eye whether the phase lines are propagating upwards, as is the case in general. Figure 4.13d plots the polarisation ratio, which is generally positive in the upper 500 m and close to 1 at 2000 m. The mean polarisation for the full time series is 1.7 ± 0.4 at 500 m and 1.6 ± 0.5 at 2000 m, indicating, that in general there is a net downward propagation of internal wave energy. The confidence in this result is low, however, because vertical shear was only measured at 4 points at both levels, meaning that the internal wave band is poorly resolved.

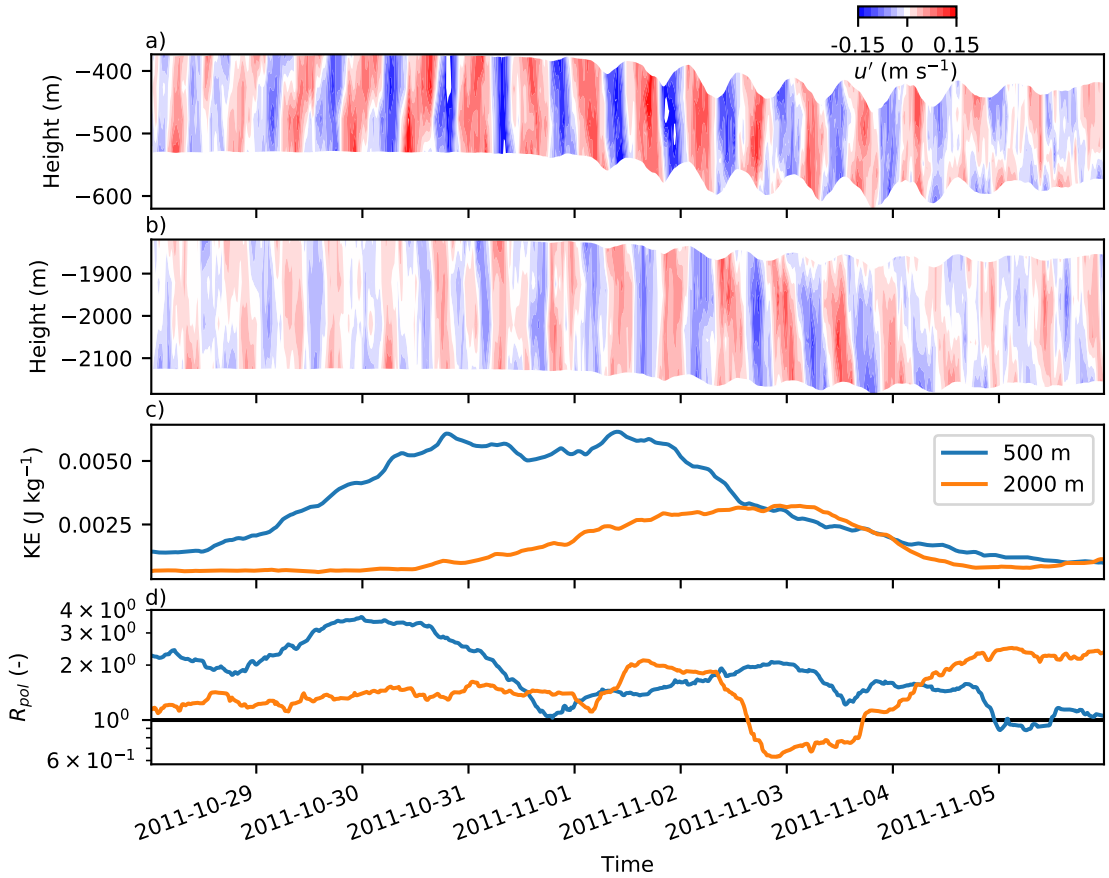

Figure 4.13: Uncorrected, band pass filtered data from a small portion of central mooring time series shows a) zonal velocity at 500 m depth and b) zonal velocity at 2000 m depth. The kinetic energy at the two levels is plotted in c) and the polarisation ratio in d).

Barotropic tides

The main barotropic constituents estimated using the tidal inversion software OTIS for a position close to the mooring site are listed in Table 4.1. The constituents with the largest magnitude are S2 and M2, both equal to roughly 1 cm s^{-1}. Fits of tidal constituents to high pass filtered data using `utide` indicate that the barotropic tidal speed is less than 2 cm s^{-1} at all moorings. These estimates are an order of magnitude less than typical near inertial and internal tide speeds and are therefore unlikely to significantly contaminate velocity data.

Table 4.1: Output from the tidal inversion software OTIS for a point close to the mooring array (-55.8196 N, -58.8444 E).

Constituent	u (cm s^{-1})	v (cm s^{-1})
M2	0.1624	0.7832
S2	0.8633	0.2876
N2	0.1961	0.3489
K2	0.2191	0.0621
K1	0.9857	0.0966

Horizontal wave stress

A small portion of the velocity and stress time series from C mooring are plotted in Figure 4.14. It can be seen that large stresses, in both normal and shear components, are the result of strong near inertial events. Similar examples can be found throughout the time series at each mooring. The full stress time series also exhibits changes at lower frequency, and it is this long period stress variations that appear to give rise to the anticipated linear relationship between strain and stress. This point is expanded on in the next section.

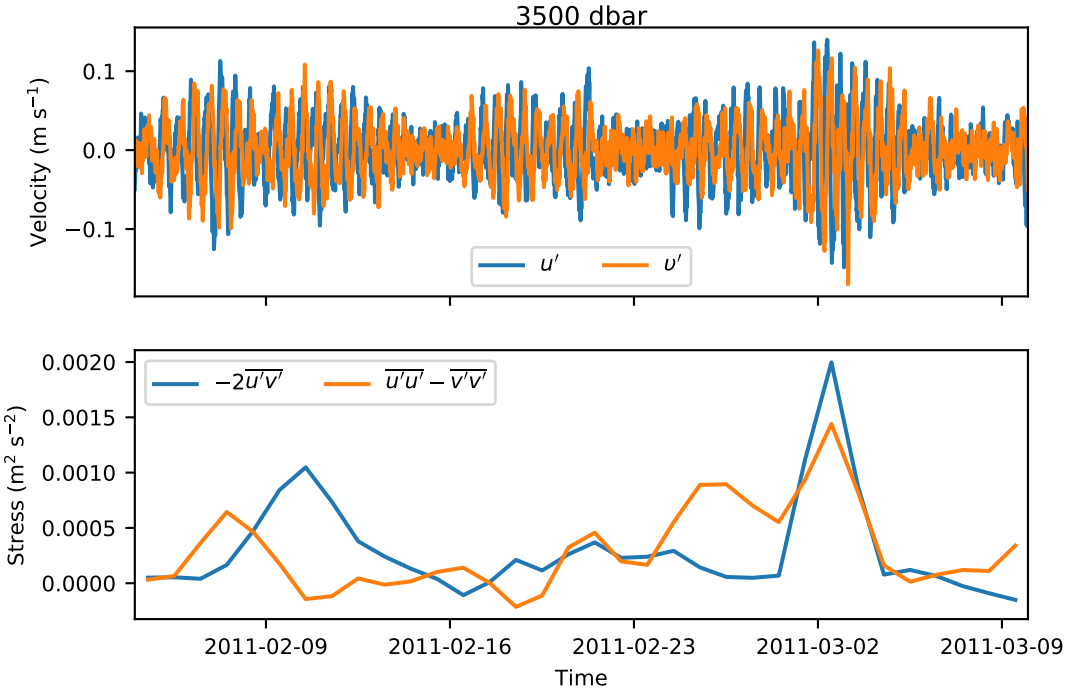

Figure 4.14: A segment of the time series of high pass filtered velocity (upper) and stress (lower) from 3500 dbar at the central mooring.

4.3.2 Horizontal coupling

Prior to estimating horizontal viscosity, we consider the relationship between stress and strain at the mooring array. Time series of the shear component are compared directly, from 550 m depth at C mooring, in Figure 4.15c. Figure 4.15b displays the wavelet coherence, from which it can be seen, that the two series are coherent at 95% significance over time periods of about 20 to 50

days over much of the record. Two measures of the record average coherence, plotted in Figure 4.15d, also show a significant peak over the same periods. The phase difference between the two series, for regions of significant coherence, is shown in Figure 4.15a and is generally close to zero or slightly negative, indicating that strain tends to lag stress. This coherence at periods of 20 to 50 days, with close to zero phase difference, is repeated at all the moorings in the shallowest 2 to 3 corrected levels. The deepest two levels do not display any significant coherence. Contrast the shear components results to that of the normal components, shown in Figure 4.16. The two series appear to be uncorrelated, and correspondingly, there is no evidence of significant coherence. This result is repeated for all moorings at all depths.

Figure 4.17 displays both the data and result of fitting a straight line to shear stress and eddy strain at C mooring. Straight line fits reveal significant correlation at the shallowest two levels, with very weak to no correlation in the lower two levels. It should be noted, that results from some moorings, such as the NW plotted in Figure 4.18 display much stronger correlation at the central 1200 dbar level, while all show weak correlation at the deepest levels. Horizontal viscosity coefficients derived from these fits are in the range 10 to 20 $\mathrm{m}^2\ \mathrm{s}^{-1}$. The viscosity value exhibits a dependency on the choice of the length of Fourier transform used to estimate the internal wave stress, with longer windows resulting in higher viscosities. However, the effect is less than a factor of two for doubling the window length, and smaller in magnitude than the error bars associated with the straight line fit. Results from fits to normal stress and eddy strain are plotted in Figure 4.19 for C mooring. In general, the fits are not significantly different from zero, and when they are, results from other moorings do not corroborate the values. It suffices to say that efforts to estimate a horizontal viscosity from the normal components of stress and strain were unsuccessful.

4.3.3 Vertical coupling

Following Polzin (2010) we attempt to estimate the order of magnitude of the vertical viscosity coefficient by integration of the effective vertical stress, defined as,

$$-\operatorname{sgn}\left(\frac{\partial\overline{u}}{\partial z}\right)\left(\overline{u'w'}-\frac{f}{N^2}\overline{b'v'}\right)\mathrm{RMS}\left(\frac{\partial\overline{u}}{\partial z}\right)-\operatorname{sgn}\left(\frac{\partial\overline{v}}{\partial z}\right)\left(\overline{v'w'}+\frac{f}{N^2}\overline{b'u'}\right)\mathrm{RMS}\left(\frac{\partial\overline{v}}{\partial z}\right) \tag{4.28}$$

over the internal wave frequency band, where RMS denotes the root mean square of a quantity. Stresses were computed via Fourier transform over the whole record using Welch's method with a window of 8192 data points. The results do not converge to a similar value at any depth across the moorings, as can be seen from Figure 4.20. We should note that multiple moorings suffered from large errors in the vertical velocity estimate. Fits of vertical stress to vertical shear did not provide a significant correlation.

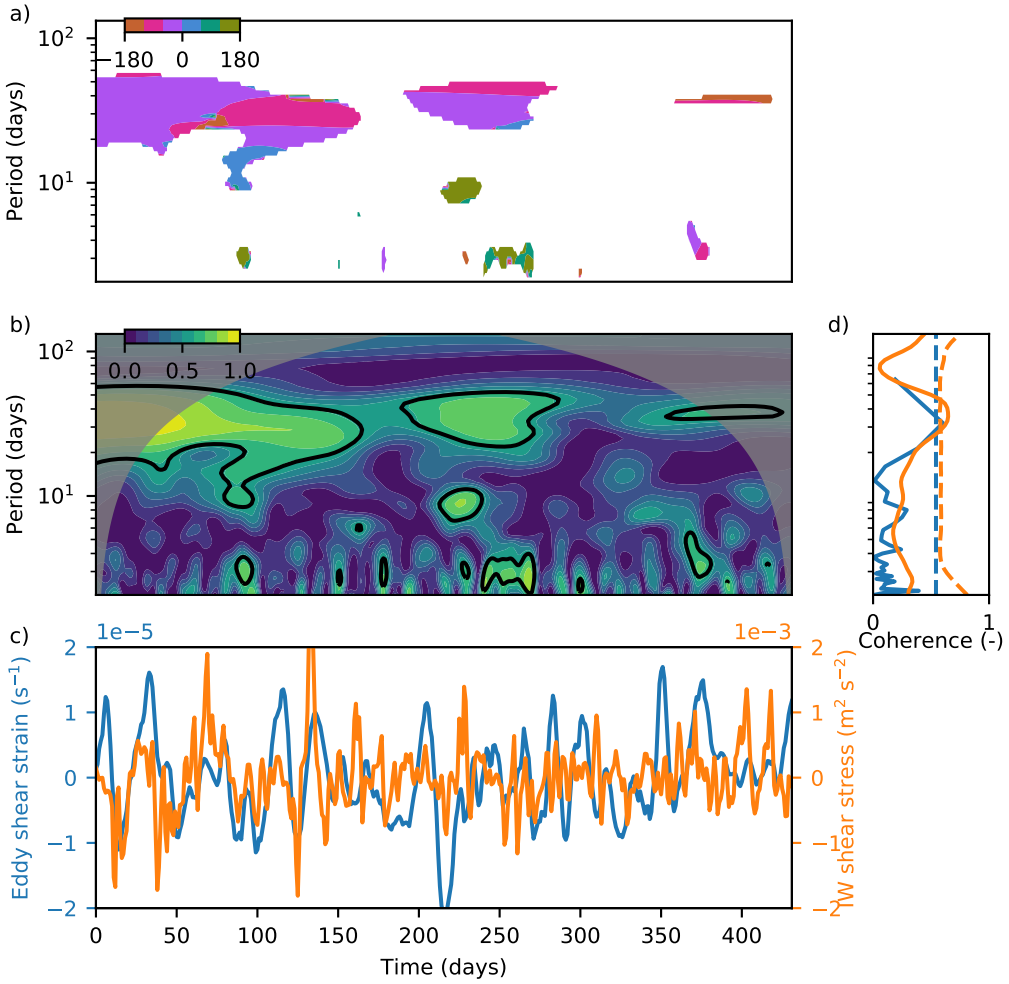

Figure 4.15: Data from the central mooring at 550 dbar display: a) Phase difference in degrees between shear strain and stress computed using the wavelet transform. Negative values indicate that strain lags stress. b) Wavelet magnitude squared coherence between strain and stress as function of time since start of record and period. The thick black contour denotes values above the 95% significance threshold. In the shaded regions, edge effects reduce confidence in the result. c) Strain and stress time series. d) Global wavelet spectrum of coherence, equal to the average over time of values plotted in 'b)' (orange line), and Fourier transform coherence (blue line). Dashed lines denote the 95% confidence threshold.

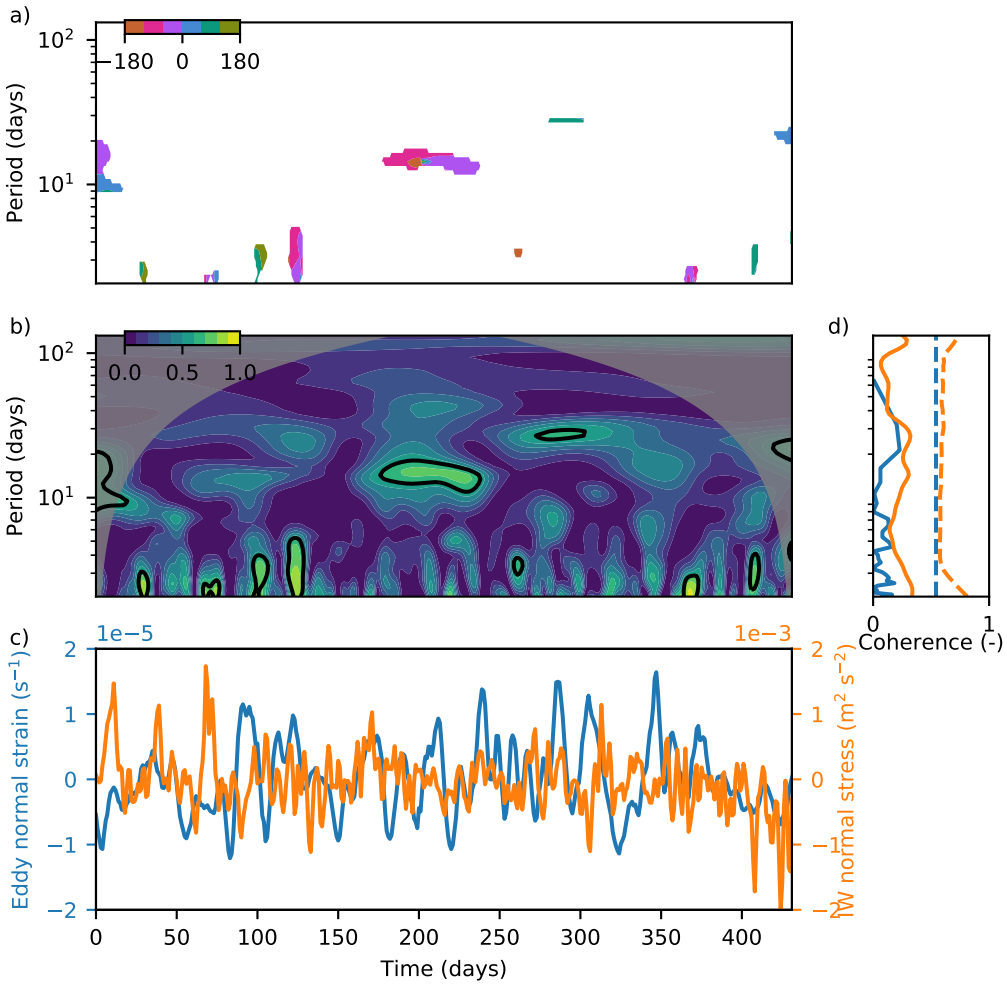

Figure 4.16: Normal strain and stress analysis from 550 dbar and C mooring. See Figure 4.15 caption for plot details. There is no evidence of correlation between the two quantities.

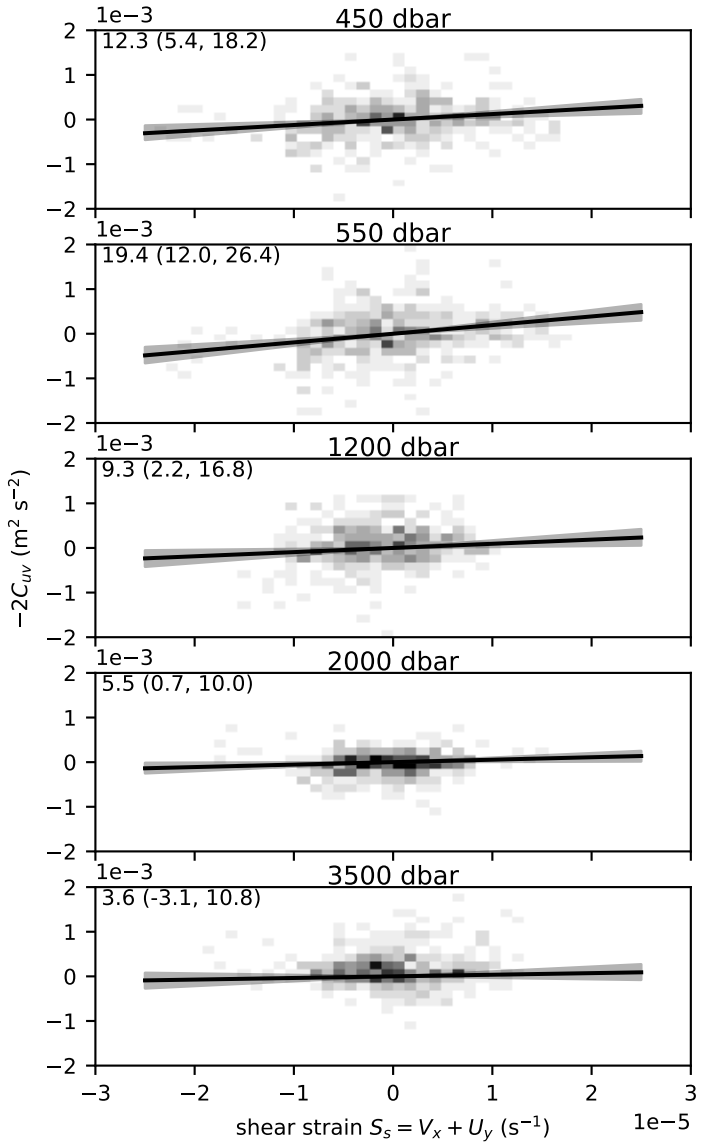

Figure 4.17: Internal wave shear stress is plotted against shear strain for 5 depth levels of the central mooring as a two dimensional histogram, the shading being proportional to the number of data points that fall within that area of the plot. The straight lines are best fit estimates to the data including a 95% confidence outer shading. The number in the upper left corner indicates the best fit horizontal viscosity in units of m^2 s^{-1} with the 95% confidence interval in brackets.

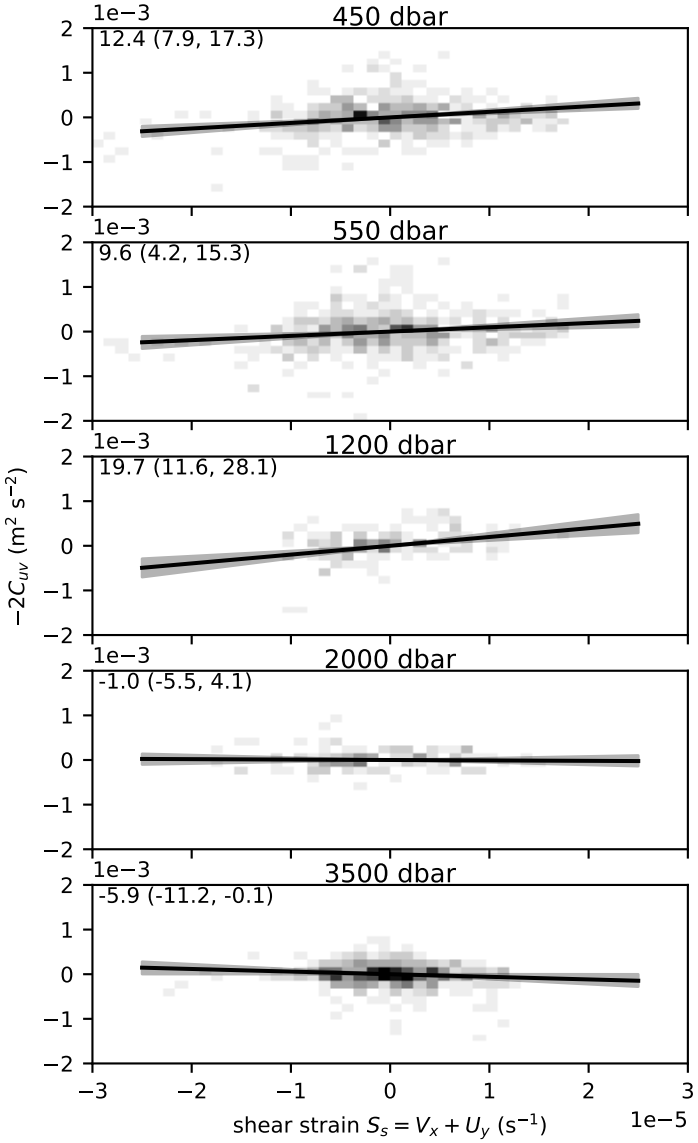

Figure 4.18: Internal wave shear stress is plotted against shear strain for 5 depth levels of the north west mooring. See Figure 4.17 for details.

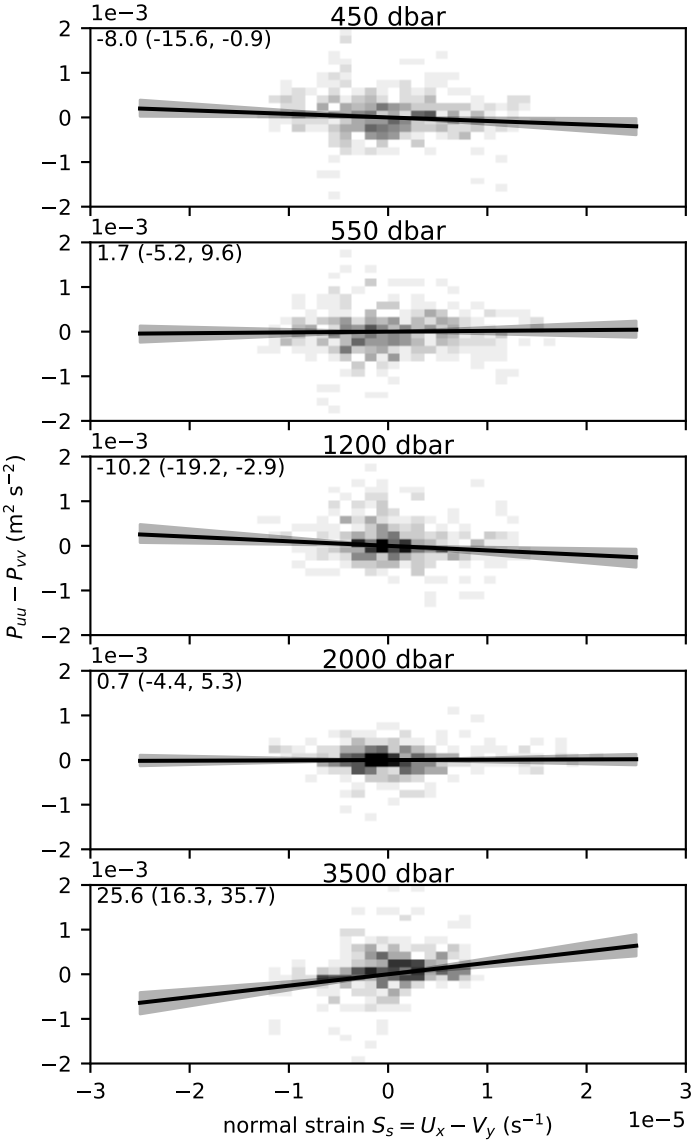

Figure 4.19: Fits to normal stress and strain data at the central mooring, see Figure 4.17 for details. Results at 550 dbar and 2000 dbar are not statistically different from zero. Results at other depths are not corroborated by analysis of other moorings.

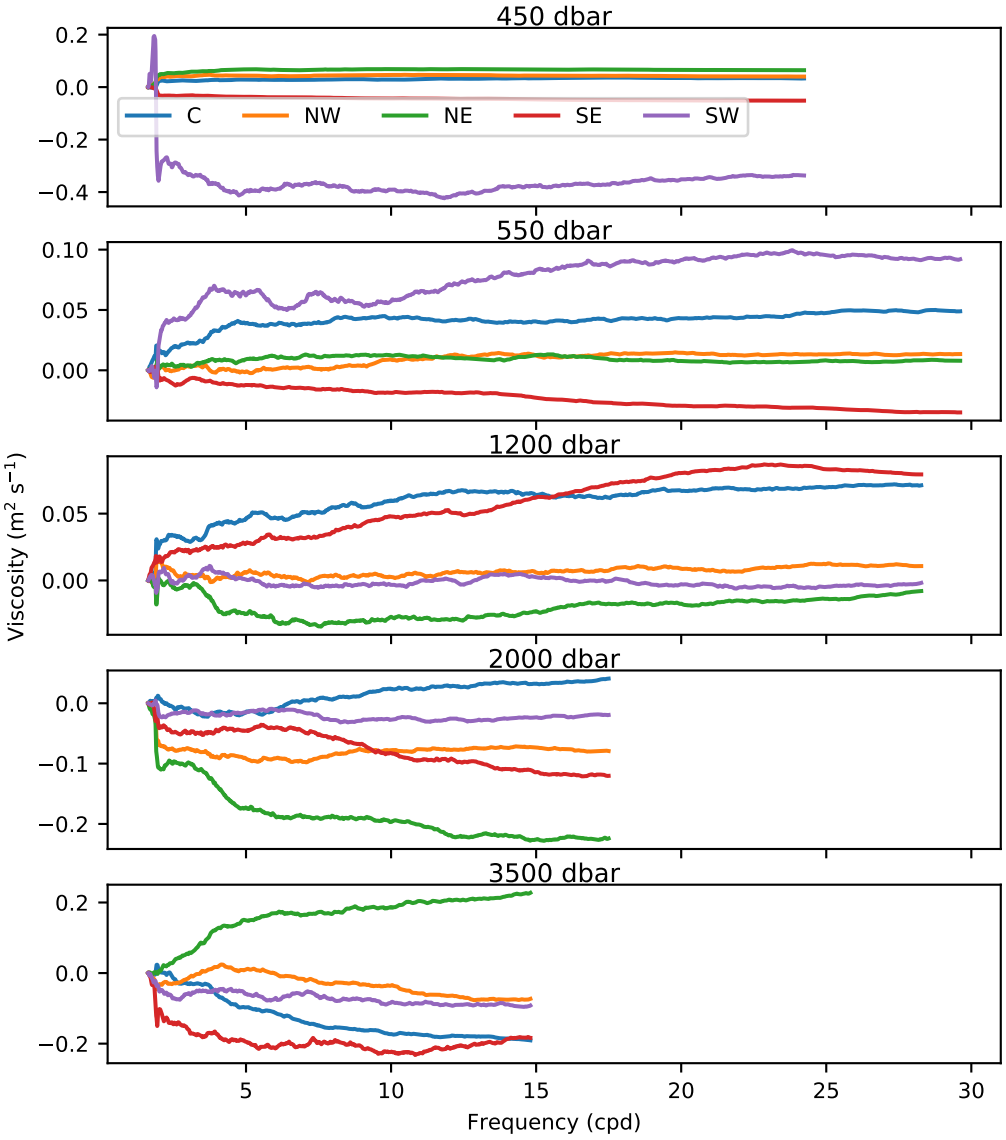

Figure 4.20: Cumulative integrals of the effective vertical stress, normalised by the root mean square vertical shear. The lines end at different frequency values, corresponding to the estimate of N at that level.

4.3.4 Energetics

In order to place the results in a wider oceanographic context, we estimate the energy transfer from eddies to internal waves using Equation 4.14. Taking the distribution of horizontal viscosities provided by the fits allows the estimation of a probability density function of this transfer which is plotted in Figure 4.21. At the shallower levels, its order magnitude is 1×10^{-9} W kg^{-1}, decreasing towards the bottom. This result is reproduced at all the other moorings (not shown). The spread of the results is large enough that at the deepest level, the transfer rate is not significantly different from zero.

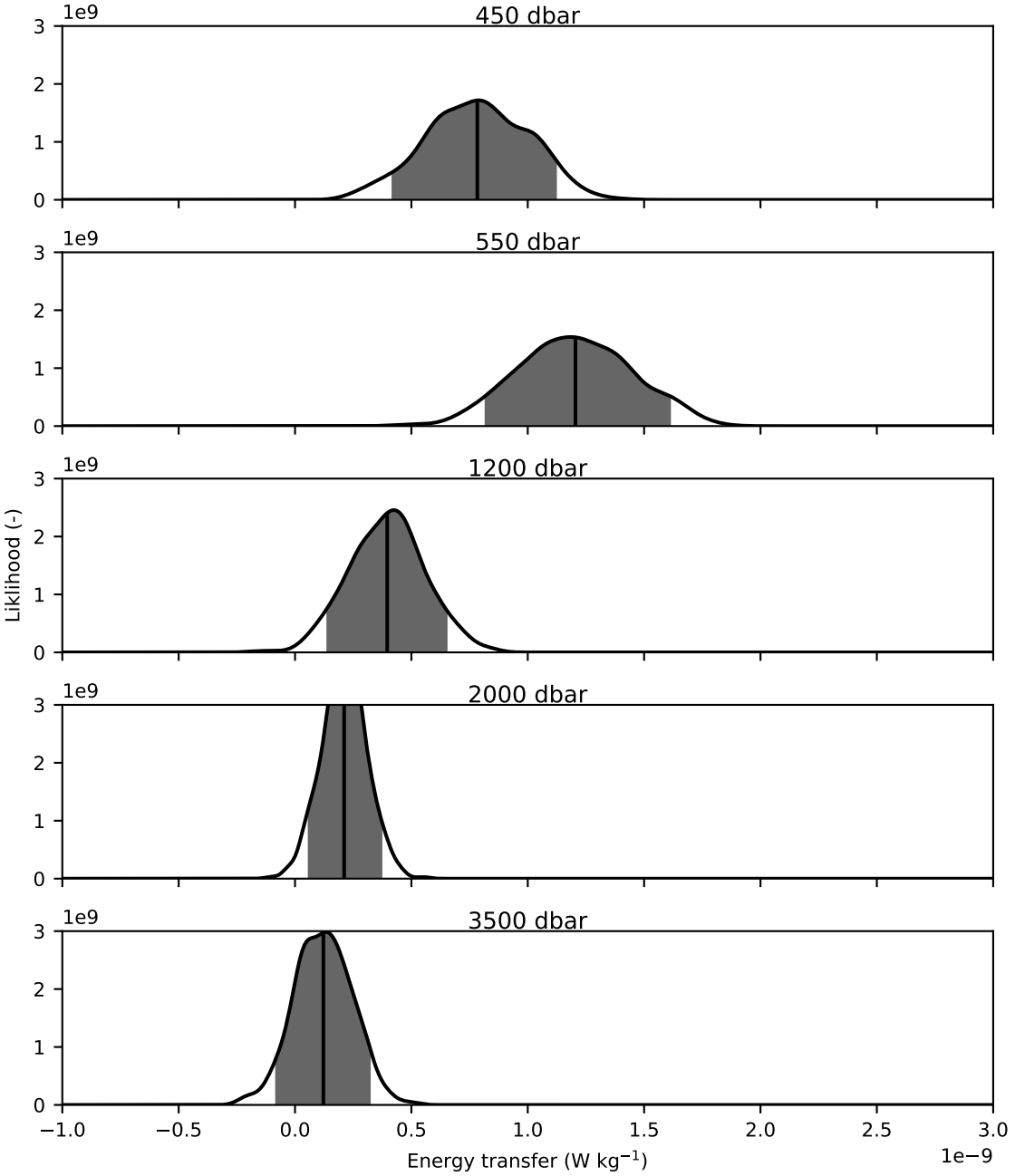

Figure 4.21: Energy transfer from eddies to internal waves estimated at C mooring. The probability density is plotted, and the 95% confidence shaded. The central vertical line denotes the mean.

The energy transfers between the mean flow and eddies, calculated using Equations (4.15) to (4.17), are depicted in Figure 4.22. In the shallower levels, eddies gain much of their energy from the available potential energy in the mean flow, where the conversion rate approaches 4×10^{-8} W kg^{-1}. This is largely balanced by a transfer of energy from eddies to the mean, which is of a similar order of magnitude but opposite in sign. Transfer from the kinetic energy of the mean flow to that of eddies is about a factor of 4 smaller than the other two terms. These transfers describe a recycling of energy between the mean flow and eddies, the net magnitude of which is smaller than the uncertainties on the individual terms, but should be equal to the sum of dissipation, advection and propagation.

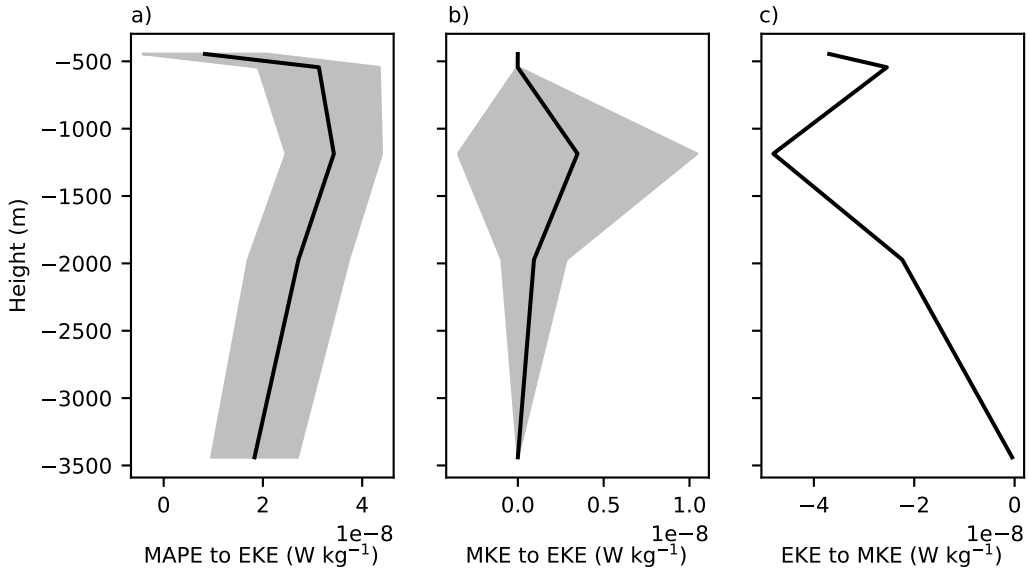

Figure 4.22: Estimates of eddy conversions from the mean flow to eddies, estimated using Equations (4.15) to (4.17). a) Mean available potential energy to eddy kinetic energy, b) mean kinetic energy to eddy kinetic energy and c) eddy kinetic energy to mean kinetic energy. The shading denotes plus and minus one standard deviation from the mooring mean. Note that the x-axis limits are not equal.

The final process analysed in this chapter is bottom boundary layer dissipation, quantified using the cubic formula in Equation 4.18. Using a drag coefficient of 2×10^{-3}, taking the eddy velocity from the lowest corrected level, and averaging over the 5 moorings, we estimate its magnitude to be 14 ± 5 mW m^{-2}. This is equivalent to a dissipation rate of about 3×10^{-9} W kg^{-1} averaged over 4 km deep water, comparable in order of magnitude to the horizontal viscous dissipation due to internal wave stress. Brearley et al. (2013) estimates the loss of eddy energy to lee waves at the same mooring site by applying linear lee wave theory to observed stratification, bottom topography and near bottom flow speed. They find an annual mean lee wave radiation rate of 5.3 mW m^{-2}, roughly equivalent to a dissipation rate of 1×10^{-9} W kg^{-1} over the water column.

Internal wave dissipation

The mean profile of the turbulent dissipation rate measured using a Vertical Microstructure Profiler (VMP) is superposed on top of the histogram of all measurements in Figure 4.23. It can be seen that over the full water column, values typically fall in the range 5×10^{-11} to 1×10^{-9} W kg^{-1}. The mean profile exists at the higher end of this range, as a result of the long tail in the typical distribution of turbulent dissipation. The depth average dissipation rate for depths greater than 100 m was 4.6×10^{-10} W kg^{-1}. Dissipation of internal wave energy due to bottom boundary layer interaction is quantified using (4.18) multiplied by a factor of 2 (Polzin, 2010). It is found to be 0.6 ± 0.4 mW m^{-2}, very roughly equivalent to a depth average of 1.5×10^{-10} W kg^{-1}.

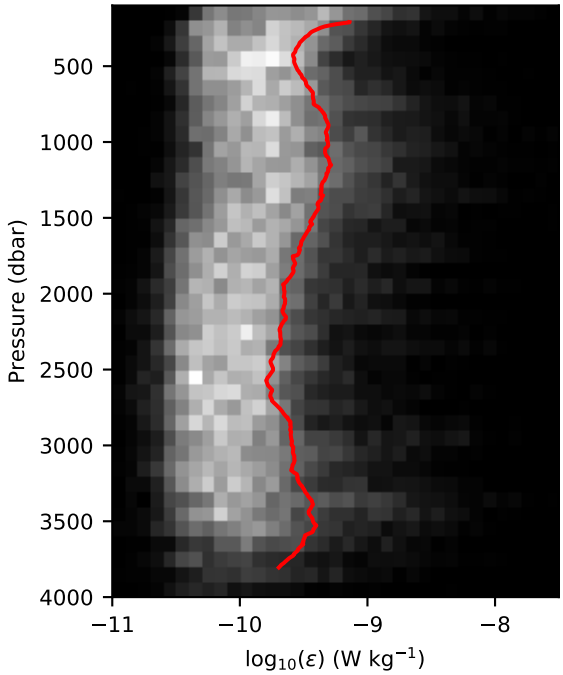

Figure 4.23: A two dimensional histogram of turbulent dissipation measurements as a function of pressure. The shading is proportional to the number of measurements within the bin. The red curve is the average dissipation profile (not the average after taking the logarithm).

4.4 Discussion and conclusion

Current meter and CTD data from a mooring array in the north Scotia Sea were used to assess the energy budget of the mesoscale eddy field, focusing in particular on the exchange of energy between eddies and the internal wave field. The array consisted of 5 moorings arranged in a 10 km wide cross. Following the theoretical work of Muller (1976), the internal wave stress was parametrised as a viscosity multiplied by spatial gradients of the eddy velocity field, which were further separated into horizontal and vertical components. The horizontal coefficient of viscosity was calculated to be in the range 10 to 20 m^2 s^{-1} between depths of 450 and 1200 m,

diminishing with depth. Viscosity estimates deeper than 2000 m were not statistically different from zero. This result is a factor of 3 smaller than that found from the LDE moorings (Polzin, 2010), despite typical stress and strain values being larger in the Scotia Sea. Theoretically, the distortion and filamentation of internal wave packets propagating through a mesoscale strain field should generate stresses that extract energy from the mesoscale field. Plots of stress and strain data exhibit a high degree of scatter, especially on short time scales of hours to days, although appear coherent on longer times scales.

A particularly striking result from this work is the coherence between shear stress and strain that exists on timescales of 20 to 50 days. Tests of the sensitivity of the horizontal viscosity estimate to the time scales of variability in the data indicate that it is only significant over these multi-week time scales. The high degree of scatter exhibited in the data can be explained as the result of high frequency changes in stress caused by internal waves propagating through the mooring array. On longer timescales, similar to that of eddy propagation times, there is coherent variation in shear stress and strain. This highlights the need for sufficiently long datasets to produce a statistically significant correlation. Analysis of the stress spectra indicate that near inertial waves, including the internal tidal band, are responsible for the vast majority of the horizontal stress. Assessment of the polarisation ratio implies net downward propagation of near inertial energy through 500 m depth and 2000 m depth. While suggestive of surface generation, we hesitate to speculate on the origin of this energy since confidence in the result is low due to the small number of vertical data points in the analysis. Moreover, the Scotia Sea internal wave field is complicated in nature, having strong surface wind forcing conducive to near inertial wave generation and rough topography conducive to internal tides both of which can propagate long distances undergoing multiple boundary reflections.

Attempts to corroborate the value of the horizontal viscosity with normal stress - strain fits and to calculate the vertical viscosity coefficient were both unsuccessful. Normal stress and strain data were noisy and a confident slope could not be estimated. We note that (Polzin, 2010) found that viscosity estimated from normal stresses was about a factor of 2 lower than that from shear stresses. If this is also true at our mooring array, the value may simply be too small to be detected with confidence. The vertical viscosity estimate is sensitive to the estimate of internal wave vertical velocity, which itself is sensitive to parameters in the mooring motion adjustment scheme. Further work is required to improve the estimated vertical velocity estimates.

A general result of this work is that energy transfers between the mean flow, eddies and internal waves peaks between 450 and 1200 dbar. The eddy energy budget at the DIMES mooring array can be summarised as follows; energy transfer between the mean flow and eddies is the residual of 3 uncertain terms, 1) transfer of mean available potential energy to eddy kinetic energy via baroclinic instability $\sim 4 \times 10^{-8}$ W kg−1, 2) transfer from eddy kinetic energy into mean kinetic energy by eddy stresses $\sim -4 \times 10^{-8}$ W kg−1 and, 3) transfer of mean kinetic energy to eddy

kinetic energy $\sim 5 \times 10^{-9}$ W kg−1. The residual of these quantities is smaller than the typical error on the terms ($\sim 1 \times 10^{-8}$ W kg−1) and is equal to the sum of dissipation, propagation and advection of eddy energy. The dissipation term has been the focus of this work and is assumed to comprise of losses to the internal wave field due to horizontal stresses, $\sim -1 \times 10^{-9}$ W kg−1, and to viscous processes in the bottom boundary layer $\sim -3 \times 10^{-9}$ W kg−1. While estimates of the loss to viscous stresses remain a work in progress, assuming the same factor of 3 difference found by (Polzin, 2010), we would expect its order of magnitude to be $\sim -3 \times 10^{-10}$ W kg−1. Finally, work by Brearley et al. (2013) finds that the annual mean flux of energy from eddies to lee waves is $\sim 1 \times 10^{-9}$ W kg^{-1} at the mooring site. We conclude, based on the magnitude of these quantities, that dissipation of eddy energy via interaction with internal waves is significant at the DIMES mooring array. All transfers in the energy budget are about an order of magnitude larger than those at the LDE array (Bryden, 1982; Polzin, 2010), reflecting the more energetic nature of the mesoscale eddy field in the north Scotia Sea.

The physical interaction between eddies and waves considered in this work is not a source of internal waves, but rather an enhancement of a pre-existing wave field. Recent numerical modelling work into the radiation of internal waves by submesoscale frontal structures (Shakespeare and Hogg, 2017), using an idealised channel model, provides further evidence of this process. Time mean estimates of energy fluxes into lee waves in the Drake Passage (Nikurashin et al., 2014) are of order 10 mW m^{-2}, which is very roughly equivalent to depth mean input of 2×10^{-9} W kg^{-1} and estimates of energy input into internal tides are similar in magnitude (Nycander, 2005). Input into near inertial waves via wind forcing are uncertain (Alford et al., 2016) but may be slightly smaller than those of lee waves and internal tides in Drake Passage (e.g Jiang et al., 2005). Our results suggest that eddy - wave interactions constitute a significant flux of energy into the internal wave field, comparable in magnitude to sources of internal wave energy.

This chapter has examined the interaction of internal waves and eddies at a mooring array in the north Scotia Sea, the first such analysis outside of the northwest Atlantic. It indicates that energy transfers from eddies to waves are important in comparison to other mechanisms of eddy energy dissipation. Moreover, the transfer is also a significant source of internal wave energy.

Chapter 5

Conclusion

5.1 Introduction

All the results presented in this thesis come from the Drake Passage and Scotia Sea, located in the Southern Ocean. The first chapter provided an overview of how the ocean dynamics occurring there are of great significance within the climate system. Understanding the region is especially important given current concern with climate change. Furthermore, it was emphasised that the connection between processes with very different temporal and spacial scales was a key part of the story. This thesis has covered two scientific topics broadly concerned with the physical mechanisms transferring energy from the large scale flow into smaller scale motions and ultimately turbulence. This chapter summarises the findings from the previous three chapters and highlights their significance for our understanding of Southern Ocean dynamics. Potential avenues of future work are presented at the end.

5.2 Summary of results

Chapter 2 covered the derivation and analysis of a model for profiling float vertical motion. By subtracting the modelled float motion from the measured motion, an estimate of the absolute vertical water velocity was obtained. The equations of motion for an object moving in a fluid are complex and so both the acceleration of the float and the water were assumed to be negligible. The simplified equations contained several uncertain parameters, and these were optimised for each float individually, using constraints on the bulk statistics of the derived vertical velocity.

The model was only successfully applied to a minority of the floats deployed during DIMES, however, those to which the model was applied successfully provided accurate and useful vertical velocity measurements. The accuracy, determined from two floats singled out for detailed study, was estimated to be about 1 to 2 mm s^{-1}, similar to that estimated from gliders (Merckelbach et al., 2010; Frajka-Williams et al., 2011; Beaird et al., 2012). Four floats detected large vertical

velocity perturbations, suggestive of large amplitude internal waves. Generally, vertical velocity measurements are rare, but this is especially true in the Southern Ocean, where all measurements relatively scarce. We believe that simple models applied to vertically profiling instruments have great potential, as demonstrated by the work in this chapter, to fill gaps in our understanding of vertical flows. The model set out here, can in principle, be applied to the many hundreds of profiling floats that are in operation in the ocean at the present day.

Chapter 3 presents an analysis of data from two profiling floats that transited the Shackleton Fracture Zone (SFZ). They observed a lee wave with an amplitude of $\sim$ 120 m and vertical velocities large enough to reverse the direction of float motion. It was determined to have a wavelength of $\sim$ 1000 m, a vertical energy flux of $\sim$ 1 W m^{-2} directed upwards and corresponding downward flux of horizontal momentum $\sim$ 8 N m^{-2}. Additionally, the depth average rate of turbulent dissipation was $\sim$ 10 mW m^{-2}. The scarcity of lee wave observations provides little by way of comparison, however, estimates of lee wave energy fluxes from the same region based on observations (Sheen et al., 2013) found fluxes of order 10 mW m^{-2}, which is similar to that from idealised models (Nikurashin et al., 2014), which suggest that the energy flux saturates at 100 mW m^{-2}. Our result is considerably larger than these two estimates and also two orders of magnitude larger than the integrated dissipation rate, implying that the wave is not actively breaking. Recent observations from the Luzon Strait (Pinkel et al., 2012) show that very energetic lee waves are not unprecedented, although the barotropic tidal forcing is different from that studied here.

The lee wave observation is the first of its kind in the Southern Ocean. Its appearance is not surprising since the Drake Passage has been noted as a potential hot spot for wave generation, although, the magnitude of the fluxes observed are large compared to previous estimates and time - mean inputs into the energy and momentum budgets of the region. They are, however, broadly consistent with crude application of linear theory above a topographic blocking level. It is difficult to extrapolate from one event to the regional scale and more observations and modelling work will be required to provide context. However, many regions of rough bathymetry exist along the pathway of the ACC, such as the Kerguelen Plateau and the Macquarie Ridge, and it seems reasonable to suspect that similar waves could be generated there. The result adds to the growing body of evidence suggesting that lee waves play an important role in the dynamics of the Southern Ocean.

Chapter 4 used data from a mooring array in the Scotia Sea to assess the strength of eddy - internal wave interactions. The interaction was parametrised as a viscosity multiplied by gradients in the eddy velocity field. The horizontal viscosity coefficient was estimated to be in the range 10 to 20 m^2 s^{-1} in the upper water column, about a factor of 3 smaller than previous estimates from the Northwest Atlantic. The correlation between eddy strain and internal wave stresses that lead to this result was found to have a characteristic time period of 20 to 50 days. The rate of energy transfer from eddies to waves was found to be $\sim 2\times10^{-9}$ W kg^{-1}, significantly larger than

previous estimates, due to the energetic nature of the Scotia Sea eddy field. More work is required to assess the vertical coupling of waves and eddies, the strength of which was not successfully determined.

The work presented in this thesis is consistent with the small number of previous studies that show eddy - wave interaction is an important sink of eddy energy. It is comparable in magnitude to crude estimates of dissipation via bottom boundary layer dissipation and by generation of lee waves, making it a first order term in the energy balance. The difference between our estimate of the horizontal viscosity and previous estimates implies that globally, this effect is spatially inhomogeneous. However, many regions of the Southern Ocean exhibit similar levels of eddy kinetic energy to the Scotia Sea as well as an energetic internal wave field. It is expected that the results presented here would hold there too. More observations are required in different dynamical regimes before a global assessment can be made.

5.3 Recommendations for future work

An obvious extension of the work presented in Chapter 2 would be to apply the vertical velocity model to more profiling floats. There are currently over 3000 such floats already in operation, under the auspices of the ARGO program. Application of the model requires that the floats provide high resolution profiles and some internal engineering variables that may not normally be provided. However, these technical difficulties are likely to be easy to overcome, since many recent floats are equipped with Iridium 2-way communications, which allow for changes in mission parameters and provide more bandwidth for data transfers. Estimates of turbulence do not even require a model since it is sufficient to high pass filter pressure data. A global picture of turbulent dissipation could be gained using the large eddy method applied to high resolution pressure profiles from profiling floats.

The lee wave energy flux result presented in Chapter 3 presents two obvious questions; 1) why is it so much larger than previous estimates? and 2), what is the ultimate fate of this energy? Initial progress towards answering these questions could be made by analysing high resolution, realistic numerical models of the Drake Passage. The resolution would need to be less than 200 m in the horizontal to resolve the length scales of such waves. Although, even this may not be sufficient if one wants a realistic representation of wave breaking and dissipative processes. Ultimately, a targeted observational campaign is required to understand where lee wave energy goes, although this is a daunting task, because of their relatively small spatial scale and intermittency.

The work presented in Chapter 4 could be expanded with a more thorough analysis of vertical stresses and their relationship with eddy velocity shear. Recent work in idealised high resolution numerical modelling of wave - mean interactions have already shown promising results (Shakespeare and Hogg, 2017), and could provide insight into a subject that suffers particularly

badly from under-sampling. Investigation into the spatial and temporal variability of the viscous coefficients is required before a parametrisation suitable for inclusion in numerical models can be developed. The Surface Water Ocean Topography (SWOT) satellite, due to be launched in 2021 will provide new ways of assessing eddy dissipation using high resolution sea surface topography data. However, in-situ observations such as those presented in this thesis will still be required to provide a 'ground truth' comparison.

Glossary

AABW

Antarctic Bottom Water

AAIW

Antarctic Intermediate Water

ACC

Antarctic Circumpolar Current

CDW

Circumpolar Deep Water

DIMES

Diapycnal and Isopycnal Mixing Experiment in the Southern Ocean

EM-APEX

Electromagnetic Autonomous Profiling Explorer

IWKE

internal wave kinetic energy

IWPE

internal wave potential energy

LADCP

Lowered Acoustic Doppler Current Profiler

LCDW

Lower Circumpolar Deep Water

NADW

North Atlantic Deep Water

NI

near inertial

PF

Polar Front

QG

quasi-geostrophic

SACCF

Southern Antarctic Circumpolar Front

SAF

Subantarctic Front

SAMW

Subantarctic Mode Water

TKED

turbulent kinetic energy dissipation

UCDW

Upper Circumpolar Deep Water

VMP

Vertical Microstructure Profiler

WKBJ

Wentzel-Kramer-Brillioun-Jeffreys

Bibliography

Abernathey, R., J. Marshall, and D. Ferreira, 2011: The Dependence of Southern Ocean Meridional Overturning on Wind Stress. *Journal of Physical Oceanography*, **41 (12)**, 2261–2278.

Aguilar, D. a., and B. R. Sutherland, 2006: Internal wave generation from rough topography. *Physics of Fluids*, **18 (6)**, 066 603.

Alford, M. H., J. M. Klymak, and G. S. Carter, 2014: Breaking internal lee waves at Kaena Ridge, Hawaii. *Geophysical Research Letters*, **41 (3)**, 906–912.

Alford, M. H., J. A. MacKinnon, H. L. Simmons, and J. D. Nash, 2016: Near-Inertial Internal Gravity Waves in the Ocean. *Annual Review of Marine Science*, **8 (1)**, 95–123.

Batchelor, G. K., 2000: Flow at large reynolds number: Effects of viscosity. *An Introduction to Fluid Dynamics:*, Cambridge University Press, Cambridge, 264–377.

Beaird, N., I. Fer, P. Rhines, and C. Eriksen, 2012: Dissipation of Turbulent Kinetic Energy Inferred from Seagliders: An Application to the Eastern Nordic Seas Overflows. *Journal of Physical Oceanography*, **42 (12)**, 2268–2282.

Bell, T. H., 1975: Lee waves in stratified flows with simple harmonic time dependence. *Journal of Fluid Mechanics*, **67 (04)**, 705.

Boé, J., A. Hall, and X. Qu, 2009: Deep ocean heat uptake as a major source of spread in transient climate change simulations. *Geophysical Research Letters*, **36 (22)**, 1–5.

Bray, N. A., and N. P. Fofonoff, 1981: Available Potential Energy for MODE Eddies. *Journal of Physical Oceanography*, **11 (1)**, 30–47.

Brearley, J. A., K. L. Sheen, A. C. Naveira Garabato, D. a. Smeed, and S. Waterman, 2013: Eddy-Induced Modulation of Turbulent Dissipation over Rough Topography in the Southern Ocean. *Journal of Physical Oceanography*, **43 (11)**, 2288–2308.

Brown, E. D., and W. B. Owens, 1981: Observations of the Horizontal Interactions between the Internal Wave Field and the Mesoscale Flow. *Journal of Physical Oceanography*, **11 (11)**, 1474–1480.

Bryden, H. L., 1980: Geostrophic vorticity balance in midocean. *Journal of Geophysical Research*, **85 (C5)**, 2825.

Bryden, H. L., 1982: Sources of eddy energy in the Gulf Stream recirculation region. *Journal of Marine Research*, **40 (4)**, 1047 – 1068.

Bryden, H. L., and N. P. Fofonoff, 1977: Horizontal Divergence and Vorticity Estimates from Velocity and Temperature Measurements in the MODE Region. *Journal of Physical Oceanography*, **7 (3)**, 329–337.

Bühler, O., and M. E. McIntyre, 2005: Wave capture and waveâĂŞvortex duality. *Journal of Fluid Mechanics*, **534**, 67–95.

Capet, X., J. C. McWilliams, M. J. Molemaker, and a. F. Shchepetkin, 2008: Mesoscale to Submesoscale Transition in the California Current System. Part III: Energy Balance and Flux. *Journal of Physical Oceanography*, **38 (10)**, 2256–2269.

Chelton, D. B., M. G. Schlax, and R. M. Samelson, 2011: Global observations of nonlinear mesoscale eddies. *Progress in Oceanography*, **91 (2)**, 167–216.

Chidichimo, M. P., K. A. Donohue, D. R. Watts, and K. L. Tracey, 2014: Baroclinic Transport Time Series of the Antarctic Circumpolar Current Measured in Drake Passage. *Journal of Physical Oceanography*, **44 (7)**, 1829–1853.

Codiga, D. L., 2011: Unified Tidal Analysis and Prediction Using the UTide Matlab Functions. Tech. rep., Graduate School of Oceanography, University of Rhode Island, 59 pp.

Cunningham, S. a., 2003: Transport and variability of the Antarctic Circumpolar Current in Drake Passage. *Journal of Geophysical Research*, **108 (C5)**, 8084.

Cusack, J. M., A. C. Naveira Garabato, D. A. Smeed, and J. B. Girton, 2017: Observation of a Large Lee Wave in the Drake Passage. *Journal of Physical Oceanography*, **47 (4)**, 793–810.

D'Asaro, E. A., D. M. Farmer, J. T. Osse, and G. T. Dairiki, 1996: A Lagrangian Float. *Journal of Atmospheric and Oceanic Technology*, **13 (6)**, 1230–1246.

D'Asaro, E. a., and R.-C. Lien, 2000a: Lagrangian Measurements of Waves and Turbulence in Stratified Flows. *Journal of Physical Oceanography*, **30 (3)**, 641–655.

D'Asaro, E. a., and R.-C. Lien, 2000b: The Wave-Turbulence Transition for Stratified Flows. *Journal of Physical Oceanography*, **30 (7)**, 1669–1678.

Dillon, T. M., 1982: Vertical overturns: A comparison of Thorpe and Ozmidov length scales. *Journal of Geophysical Research*, **87 (C12)**, 9601.

Donohue, K. A., K. L. Tracey, D. R. Watts, M. P. Chidichimo, and T. K. Chereskin, 2016: Mean Antarctic Circumpolar Current transport measured in Drake Passage. *Geophysical Research Letters*, **43 (22)**, 11,760–11,767.

Egbert, G. D., and S. Y. Erofeeva, 2002: Efficient inverse modeling of barotropic ocean tides. *Journal of Atmospheric and Oceanic Technology*, **19 (2)**, 183–204.

Ferrari, R., and C. Wunsch, 2009: Ocean circulation kinetic energy-reservoirs, sources and sinks: Supplementary material. *Annual Review of Fluid Mechanics*, **41 (1)**, 253–282.

Ferron, B., H. Mercier, K. Speer, A. Gargett, and K. Polzin, 1998: Mixing in the Romanche Fracture Zone. *Journal of Physical Oceanography*, **28 (10)**, 1929–1945.

Frajka-Williams, E., C. C. Eriksen, P. B. Rhines, and R. R. Harcourt, 2011: Determining Vertical Water Velocities from Seaglider. *Journal of Atmospheric and Oceanic Technology*, **28 (12)**, 1641–1656.

Frankignoul, C., 1976: Observed interaction between oceanic internal waves and mesoscale eddies. *Deep-Sea Research and Oceanographic Abstracts*, **23 (9)**, 805–820.

Frankignoul, C., and T. M. Joyce, 1979: On the internal wave variability during the internal wave experiment (IWEX). *Journal of Geophysical Research*, **84 (C2)**, 769.

Fritts, D. C., 2003: Gravity wave dynamics and effects in the middle atmosphere. *Reviews of Geophysics*, **41 (1)**, 1003.

Frölicher, T. L., J. L. Sarmiento, D. J. Paynter, J. P. Dunne, J. P. Krasting, and M. Winton, 2015: Dominance of the Southern Ocean in anthropogenic carbon and heat uptake in CMIP5 models. *Journal of Climate*, **28 (2)**, 862–886.

Gallet, C., and C. Julien, 2011: The significance threshold for coherence when using the Welch's periodogram method: Effect of overlapping segments. *Biomedical Signal Processing and Control*, **6 (4)**, 405–409.

Gargett, A., and T. Garner, 2008: Determining Thorpe Scales from Ship-Lowered CTD Density Profiles. *Journal of Atmospheric and Oceanic Technology*, **25 (9)**, 1657–1670.

Garrett, C., and E. Kunze, 2007: Internal Tide Generation in the Deep Ocean. *Annual Review of Fluid Mechanics*, **39 (1)**, 57–87.

Gill, A. E., 1982: *Atmosphere-Ocean Dynamics*. Academic Press, San Diego, 662 pp.

Gille, S. T., K. Speer, J. R. Ledwell, and A. C. Naveira Garabato, 2007: Mixing and stirring in the Southern Ocean. *Eos, Transactions American Geophysical Union*, **88 (39)**, 382–383.

Gonella, J., 1972: A rotary-component method for analysing meteorological and oceanographic vector time series. *Deep Sea Research and Oceanographic Abstracts*, **19 (12)**, 833–846.

Gregg, M. C., and E. Kunze, 1991: Shear and strain in Santa Monica Basin. *Journal of Geophysical Research*, **96 (C9)**, 16 709.

Grinsted, A., J. C. Moore, and S. Jevrejeva, 2004: Application of the cross wavelet transform and wavelet coherence to geophysical time series. *Nonlinear Processes in Geophysics*, **11 (5/6)**, 561–566.

Hellerman, S., and M. Rosenstein, 1983: Normal Monthly Wind Stress Over the World Ocean with Error Estimates. *Journal of Physical Oceanography*, **13 (7)**, 1093–1104.

Hennon, T. D., S. C. Riser, and M. H. Alford, 2014: Observations of Internal Gravity Waves by Argo Floats. *Journal of Physical Oceanography*, **44 (9)**, 2370–2386.

Hibiya, T., N. Furuichi, and R. Robertson, 2012: Assessment of fine-scale parameterizations of turbulent dissipation rates near mixing hotspots in the deep ocean. *Geophysical Research Letters*, **39 (24)**, n/a–n/a.

Hogg, A. M., 2010: An Antarctic Circumpolar Current driven by surface buoyancy forcing. *Geophysical Research Letters*, **37 (23)**, 1–5.

Hogg, A. M., M. P. Meredith, D. P. Chambers, E. P. Abrahamsen, C. W. Hughes, and A. K. Morrison, 2015: Recent trends in the Southern Ocean eddy field. *Journal of Geophysical Research: Oceans*, n/a–n/a.

Howard, L. N., 1961: Note on a paper of John W. Miles. *Journal of Fluid Mechanics*, **10 (04)**, 509.

IOC, SCOR, and IAPSO, 2010: *The international thermodynamic equation of seawater - 2010: Calculation and use of thermodynamic properties*. Intergovernmental Oceanographic Commission, Manuals and Guides No. 56 UNESCO (English), 196 pp.

Jackett, D. R., and T. J. McDougall, 1997: A Neutral Density Variable for the World's Oceans. *Journal of Physical Oceanography*, **27 (2)**, 237–263.

Jiang, J., Y. Lu, and W. Perrie, 2005: Estimating the energy flux from the wind to ocean inertial motions: The sensitivity to surface wind fields. *Geophysical Research Letters*, **32 (15)**, 1–5.

Kantha, L. H., and C. A. Clayson, 2000: *Small Scale Processes in Geophysical Fluid Flows*, Vol. 67. Academic press, San Diego, California, 888 pp.

Kilbourne, B. F., and J. B. Girton, 2015: Quantifying High-Frequency Wind Energy Flux into Near-Inertial Motions in the Southeast Pacific. *Journal of Physical Oceanography*, **45**, 369–386.

Klein, P., and G. Lapeyre, 2009: The Oceanic Vertical Pump Induced by Mesoscale and Submesoscale Turbulence. *Annual Review of Marine Science*, **1 (1)**, 351–375.

Kunze, E., E. Firing, J. M. Hummon, T. K. Chereskin, and A. M. Thurnherr, 2006: Global Abyssal Mixing Inferred from Lowered ADCP Shear and CTD Strain Profiles. *Journal of Physical Oceanography*, **36 (8)**, 1553–1576.

Kunze, E., L. K. Rosenfeld, G. S. Carter, and M. C. Gregg, 2002: Internal Waves in Monterey Submarine Canyon. *Journal of Physical Oceanography*, **32**, 1890–1913.

Kunze, E., and T. B. Sanford, 1984: Observations of Near-Inertial Waves in a Front. *Journal of Physical Oceanography*, **14 (3)**, 566–581.

Lamb, K. G., 2014: Internal Wave Breaking and Dissipation Mechanisms on the Continental Slope/Shelf. *Annual Review of Fluid Mechanics*, **46 (1)**, 231–254.

Le Quéré, C., and Coauthors, 2012: The global carbon budget 1959-2011. *Earth System Science Data*, **5**, 1107–1157.

Ledwell, J. R., E. Montgomery, K. L. Polzin, L. St. Laurent, R. W. Schmitt, and J. M. Toole, 2000: Evidence for enhanced mixing over rough topography in the abyssal ocean. *Nature*, **403 (6766)**, 179–82.

Liu, W., F. P. Bretherton, Z. Liu, L. Smith, H. Lu, and C. J. Rutland, 2010: Breaking of Progressive Internal Gravity Waves: Convective Instability and Shear Instability*. *Journal of Physical Oceanography*, **40**, 2243–2263.

Livermore, R., C. D. Hillenbrand, M. Meredith, and G. Eagles, 2007: Drake Passage and Cenozoic climate: An open and shut case? *Geochemistry, Geophysics, Geosystems*, **8 (1)**.

MacKinnon, J., 2013: Oceanography: Mountain waves in the deep ocean. *Nature*, **501 (7467)**, 321–322.

MacKinnon, J., L. St Laurent, and A. C. Naveira Garabato, 2013: Diapycnal Mixing Processes in the Ocean Interior. *Ocean Circulation and Cliamte: A 21st Century Perspective*, Academic Press, 159–183.

Mann, K. H., and J. R. N. Lazier, 2006: *Dynamics of marine ecosystems: biological-physical interactions in the oceans*. Blackwell Publishing, 496 pp.

Marshall, J., and T. Radko, 2003: Residual-Mean Solutions for the Antarctic Circumpolar Current and Its Associated Overturning Circulation. *Journal of Physical Oceanography*, **33 (11)**, 2341–2354.

Marshall, J., and K. Speer, 2012: Closure of the meridional overturning circulation through Southern Ocean upwelling. *Nature Geoscience*, **5 (3)**, 171–180.

Mazloff, M. R., P. Heimbach, and C. Wunsch, 2010: An Eddy-Permitting Southern Ocean State Estimate. *Journal of Physical Oceanography*, **40 (5)**, 880–899.

McFarlane, N. a., 1987: The Effect of Orographically Excited Gravity Wave Drag on the General Circulation of the Lower Stratosphere and Troposphere. *Journal of the Atmospheric Sciences*, **44 (14)**, 1775–1800.

McGillicuddy, D. J., 2016: Mechanisms of Physical-Biological-Biogeochemical Interaction at the Oceanic Mesoscale. *Annual Review of Marine Science*, **8 (1)**, 125–159.

Merckelbach, L., D. Smeed, and G. Griffiths, 2010: Vertical Water Velocities from Underwater Gliders. *Journal of Atmospheric and Oceanic Technology*, **27 (3)**, 547–563.

Meredith, M. P., 2011: Cruise Report, RRS James Cook JC054 (DIMES UK2). Tech. rep., British Antarctic Survey, 206 pp.

Meyer, A., K. L. Polzin, B. M. Sloyan, and H. E. Phillips, 2016: Internal Waves and Mixing near the Kerguelen Plateau. *Journal of Physical Oceanography*, **46 (2)**, 417–437.

Miles, J. W., 1961: On the stability of heterogeneous shear flows. *Journal of Fluid Mechanics*, **10 (04)**, 496.

Millard, R. C., W. B. Owens, and N. P. Fofonoff, 1990: On the calculation of the Brunt-Väisälä frequency. *Deep-Sea Research*, **37 (1)**, 167–181.

Muller, P., 1976: On the diffusion of momentum and mass by internal gravity waves. *Journal of Fluid Mechanics*, **77 (04)**, 789–823.

Müller, P., G. Holloway, F. Henyey, and N. Pomphrey, 1986: Nonlinear interactions among internal gravity waves. *Reviews of Geophysics*, **24 (3)**, 493.

Munday, D. R., H. L. Johnson, and D. P. Marshall, 2013: Eddy Saturation of Equilibrated Circumpolar Currents. *Journal of Physical Oceanography*, **43 (3)**, 507–532.

Munk, W., 1980: Internal waves and small-scale processes. *Evolution of Physical Oceanography: Scientific Surveys in Honor of Henry Stommel*, B. A. Warren, and C. Wunsch, Eds., MIT Press, 264–290.

Munk, W. H., 1966: Abyssal recipes. *Deep Sea Research and Oceanographic Abstracts*, **13 (January)**, 707 – 730.

Nash, J. D., M. H. Alford, and E. Kunze, 2005: Estimating Internal Wave Energy Fluxes in the Ocean. *Journal of Atmospheric and Oceanic Technology*, **22 (10)**, 1551–1570.

Naveira Garabato, A. C., R. Ferrari, and K. L. Polzin, 2011: Eddy stirring in the Southern Ocean. *Journal of Geophysical Research*, **116 (C9)**, C09 019.

Naveira Garabato, A. C., a. J. G. Nurser, R. B. Scott, and J. a. Goff, 2013: The Impact of Small-Scale Topography on the Dynamical Balance of the Ocean. *Journal of Physical Oceanography*, **43 (3)**, 647–668.

Naveira Garabato, A. C., K. L. Polzin, B. A. King, K. J. Heywood, and M. Visbeck, 2004: Widespread intense turbulent mixing in the Southern Ocean. *Science*, **303 (5655)**, 210–3.

Nikurashin, M., and R. Ferrari, 2010a: Radiation and Dissipation of Internal Waves Generated by Geostrophic Motions Impinging on Small-Scale Topography: Application to the Southern Ocean. *Journal of Physical Oceanography*, **40 (9)**, 2025–2042.

Nikurashin, M., and R. Ferrari, 2010b: Radiation and Dissipation of Internal Waves Generated by Geostrophic Motions Impinging on Small-Scale Topography: Theory. *Journal of Physical Oceanography*, **40 (5)**, 1055–1074.

Nikurashin, M., and R. Ferrari, 2011: Global energy conversion rate from geostrophic flows into internal lee waves in the deep ocean. *Geophysical Research Letters*, **38 (8)**, 1–6.

Nikurashin, M., and R. Ferrari, 2013: Overturning circulation driven by breaking internal waves in the deep ocean. *Geophysical Research Letters*, **40 (12)**, 3133–3137.

Nikurashin, M., R. Ferrari, N. Grisouard, and K. Polzin, 2014: The Impact of Finite-Amplitude Bottom Topography on Internal Wave Generation in the Southern Ocean. *Journal of Physical Oceanography*, **44 (11)**, 2938–2950.

Nikurashin, M., G. K. Vallis, and A. Adcroft, 2012: Routes to energy dissipation for geostrophic flows in the Southern Ocean. *Nature Geoscience*, **6 (1)**, 48–51.

Nycander, J., 2005: Generation of internal waves in the deep ocean by tides. *Journal of Geophysical Research*, **110 (C10)**, C10 028.

Olbers, D., J. Willebrand, and C. Eden, 2012: Geostrophic and Quasi-Geostrophic Motions. *Ocean Dynamics*, Springer Berlin Heidelberg, Berlin, Heidelberg, 137–157.

Orlanski, I., and K. Bryan, 1969: Formation of the thermocline step structure by large-amplitude internal gravity waves. *Journal of Geophysical Research*, **74 (28)**, 6975.

Orsi, A. H., T. Whitworth, and W. D. Nowlin, 1995: On the meridional extent and fronts of the Antarctic Circumpolar Current. *Deep Sea Research Part I: Oceanographic Research Papers*, **42 (5)**, 641–673.

Peters, H., M. C. Gregg, and T. B. Sanford, 1995: Detail and scaling of turbulent overturns in the Pacific Equatorial Undercurrent. *J. Geophys. Res.*, **100 (C9)**, 18 349–18 368.

Phillips, H. E., and N. L. Bindoff, 2014: On the nonequivalent barotropic structure of the Antarctic Circumpolar Current: An observational perspective. *Journal of Geophysical Research: Oceans*, n/a–n/a.

Phillips, H. E., and S. R. Rintoul, 2000: Eddy Variability and Energetics from Direct Current Measurements in the Antarctic Circumpolar Current South of Australia. *Journal of Physical Oceanography*, **30 (12)**, 3050–3076.

Pinkel, R., M. Buijsman, and J. Klymak, 2012: Breaking Topographic Lee Waves in a Tidal Channel in Luzon Strait. *Oceanography*, **25 (2)**, 160–165.

Polzin, K. L., 2010: Mesoscale EddyâĂŞInternal Wave Coupling. Part II: Energetics and Results from PolyMode. *Journal of Physical Oceanography*, **40 (4)**, 789–801.

Polzin, K. L., A. C. Naveira Garabato, T. N. Huussen, B. M. Sloyan, and S. Waterman, 2014: Finescale parameterizations of turbulent dissipation. *Journal of Geophysical Research: Oceans*, **119 (2)**, 1383–1419.

Polzin, K. L., J. M. Toole, J. R. Ledwell, and R. W. Schmitt, 1997: Spatial Variability of Turbulent Mixing in the Abyssal Ocean. *Science*, **276 (5309)**, 93–96.

Rhein, M., and Coauthors, 2013: Observations: ocean. *Climate Change 2013: The Physical Science Basis. Contribution of Working Group I to the Fifth Assessment Report of the Intergovernmental Panel on Climate Change*, Cambridge University Press, 255–315.

Rintoul, S. R., and A. C. Naveira Garabato, 2013: Dynamics of the Southern Ocean Circulation. *Ocean Circulation and Cliamte: A 21st Century Perspective*, Academic Press, 471–492.

Ruddick, B. R., and T. M. Joyce, 1979: Observations of Interaction between the Internal Wavefield and Low-Frequency Flows in the North Atlantic. *Journal of Physical Oceanography*, **9 (3)**, 498–517.

Sabine, C. L., 2004: The Oceanic Sink for Anthropogenic CO$_2$. *Science*, **305 (5682)**, 367–371.

Sanford, T. B., 1971: Motionally induced electric and magnetic fields in the sea. *Journal of Geophysical Research*, **76 (15)**, 3476–3492.

Sanford, T. B., J. Dunlap, J. Carlson, D. Webb, and J. B. Girton, 2005: Autonomous velocity and density profiler: EM-APEX. *Proceedings of the IEEE/OES Eighth Working Conference on Current Measurement Technology, 2005.*, Ieee, 152–156.

Scott, R. B., J. a. Goff, a. C. Naveira Garabato, and a. J. G. Nurser, 2011: Global rate and spectral characteristics of internal gravity wave generation by geostrophic flow over topography. *Journal of Geophysical Research*, **116 (C9)**, C09 029.

Scott, R. B., and Y. Xu, 2009: An update on the wind power input to the surface geostrophic flow of the World Ocean. *Deep Sea Research Part I: Oceanographic Research Papers*, **56 (3)**, 295–304.

Sévellec, F., A. C. Naveira Garabato, J. A. Brearley, and K. L. Sheen, 2015: Vertical Flow in the Southern Ocean Estimated from Individual Moorings. *Journal of Physical Oceanography*, **45 (9)**, 2209–2220.

Shakespeare, C. J., and A. M. Hogg, 2017: Spontaneous Surface Generation and Interior Amplification of Internal Waves in a Regional-Scale Ocean Model. *Journal of Physical Oceanography*, **47 (4)**, 811–826.

Sheen, K., and Coauthors, 2013: Rates and mechanisms of turbulent dissipation and mixing in the Southern Ocean: Results from the Diapycnal and Isopycnal Mixing Experiment in the Southern Ocean (DIMES). *Journal of Geophysical Research: Oceans*, **118 (6)**, 2774–2792.

Sheen, K. L., and Coauthors, 2014: Eddy-induced variability in Southern Ocean abyssal mixing on climatic timescales. *Nature Geoscience*, **7 (July)**, 6–11.

Smagorinsky, J., 1963: General Circulation Experiments With the Primitive Equations. *Monthly Weather Review*, **91 (3)**, 99–164.

Smith, W. H., and D. T. Sandwell, 1997: Global Sea Floor Topography from Satellite Altimetry and Ship Depth Soundings. *Science*, **277 (5334)**, 1956–1962.

Sokolov, S., and S. R. Rintoul, 2007: Multiple Jets of the Antarctic Circumpolar Current South of Australia*. *Journal of Physical Oceanography*, **37 (5)**, 1394–1412.

Speer, K., S. R. Rintoul, and B. Sloyan, 2000: The Diabatic Deacon Cell*. *Journal of Physical Oceanography*, **30 (12)**, 3212–3222.

St. Laurent, L., a. C. Naveira Garabato, J. R. Ledwell, a. M. Thurnherr, J. M. Toole, and a. J. Watson, 2012: Turbulence and Diapycnal Mixing in Drake Passage. *Journal of Physical Oceanography*, **42 (12)**, 2143–2152.

Staquet, C., and J. Sommeria, 2002: INTERNAL GRAVITY WAVES : From Instabilities to Turbulence. *Annual Review of Fluid Mechanics*, **34 (1)**, 559–593.

Swart, N. C., and J. C. Fyfe, 2012: Observed and simulated changes in the Southern Hemisphere surface westerly wind-stress. *Geophysical Research Letters*, **39 (16)**, n/a–n/a.

Talley, L., 2013: Closure of the Global Overturning Circulation Through the Indian, Pacific, and Southern Oceans: Schematics and Transports. *Oceanography*, **26 (1)**, 80–97.

Taylor, G. I., 1935: Statistical Theory of Turbulence. *Proceedings of the Royal Society A: Mathematical, Physical and Engineering Sciences*, **151 (873)**, 421–444.

Thorpe, S. A., 1977: Turbulence and Mixing in a Scottish Loch. *Philosophical Transactions of the Royal Society of London. Series A, Mathematical and Physical Sciences*, **286 (1334)**, 125–181.

Thurnherr, A. M., 2011: Vertical velocity from LADCP data. *2011 IEEE/OES 10th Current, Waves and Turbulence Measurements (CWTM)*, IEEE, 198–204.

Thurnherr, A. M., E. Kunze, J. M. Toole, L. St. Laurent, K. J. Richards, and A. Ruiz-Angulo, 2015: Vertical kinetic energy and turbulent dissipation in the ocean. *Geophysical Research Letters*, **42 (18)**, 7639–7647.

Torrence, C., and G. P. Compo, 1998: A Practical Guide to Wavelet Analysis. *Bulletin of the American Meteorological Society*, **79 (1)**, 61–78.

Vallis, G. K., 2006: *Atmospheric and Oceanic Fluid Dynamics*. Cambridge University Press, 745 pp.

Waterhouse, A. F., and Coauthors, 2014: Global Patterns of Diapycnal Mixing from Measurements of the Turbulent Dissipation Rate. *Journal of Physical Oceanography*, **44 (7)**, 1854–1872.

Waterman, S., A. C. Naveira Garabato, and K. L. Polzin, 2013: Internal Waves and Turbulence in the Antarctic Circumpolar Current. *Journal of Physical Oceanography*, **43 (2)**, 259–282.

Waterman, S., K. L. Polzin, A. C. Naveira Garabato, K. L. Sheen, and A. Forryan, 2014: Suppression of Internal Wave Breaking in the Antarctic Circumpolar Current near Topography. *Journal of Physical Oceanography*, **44 (5)**, 1466–1492.

Watson, A. J., J. R. Ledwell, M.-J. Messias, B. a. King, N. Mackay, M. P. Meredith, B. Mills, and A. C. Naveira Garabato, 2013: Rapid cross-density ocean mixing at mid-depths in the Drake Passage measured by tracer release. *Nature*, **501 (7467)**, 408–11.

Welch, W. T., P. Smolarkiewicz, R. Rotunno, and B. a. Boville, 2001: The Large-Scale Effects of Flow over Periodic Mesoscale Topography. *Journal of the Atmospheric Sciences*, **58 (12)**, 1477–1492.

Wright, C. J., R. B. Scott, P. Ailliot, and D. Furnival, 2014: Lee wave generation rates in the deep ocean. *Geophysical Research Letters*, **41 (7)**, 2434–2440.

Wunsch, C., 1998: The Work Done by the Wind on the Oceanic General Circulation. *Journal of Physical Oceanography*, **28 (11)**, 2332–2340.

Zhai, X., H. L. Johnson, and D. P. Marshall, 2010: Significant sink of ocean-eddy energy near western boundaries. *Nature Geoscience*, **3 (9)**, 608–612.